Droplet size, concentration, and temperature mapping in sprays using SLIPI-based techniques

Mishra, Yogeshwar Nath

2018

Document Version:
Publisher's PDF, also known as Version of record

Droplet size, concentration, and temperature mapping in sprays using SLIPI-based techniques

YOGESHWAR NATH MISHRA
DEPARTMENT OF PHYSICS | FACULTY OF ENGINEERING | LUND UNIVERSITY

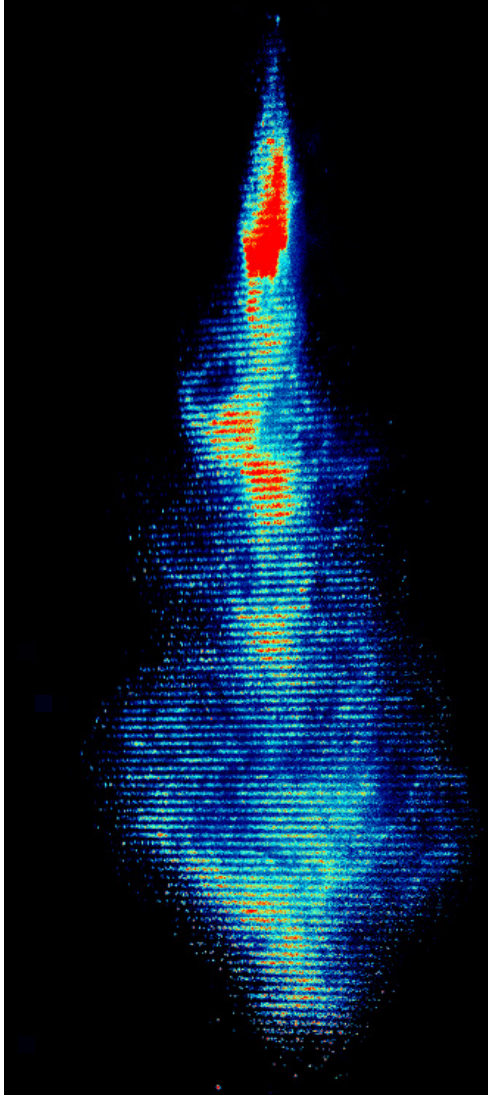

Droplet size, concentration, and temperature mapping in sprays using SLIPI-based techniques

Yogeshwar Nath Mishra

LUND
UNIVERSITY

Academic thesis, which by due permission of the Faculty of Engineering at Lund University, will be publicly defended on Friday, February 16, 2018, at 10:15 am in lecture hall Rydbergsalen, Department of Physics, Professorsgatan1, Lund, for the degree of Doctor of Philosophy in Engineering.

Faculty Opponent:
Professor Yannis Hardalupas,
Mechanical Engineering Department, Imperial College London, UK

Organization
LUND UNIVERSITY
Faculty of Engineering
Department of Physics
Division of Combustion Physics
P.O. Box 118, SE 22100
Lund, Sweden

Document name
DOCTORAL THESIS

Date of issue
January 22, 2018

Author: Yogeshwar Nath Mishra

Sponsoring organization

Title: Droplet size, concentration, and temperature mapping in sprays using SLIPI-based techniques

Abstract

Structured laser illumination planar imaging (SLIPI) is a technique capable of suppressing multiple light scattering effects in optically dense sprays, resulting in spray images without blurs and with enhanced contrast. The novelty of the work presented in this thesis concerns the applications of a variety of SLIPI-based techniques for the measurement of droplet size, droplet concentration, and liquid temperature in atomizing sprays. Two types of spray systems are investigated here: 1) Steady hollow-cone water sprays using temporally averaged imaging.
2) Transient Direct-injection spark ignition (DISI) biofuel sprays using instantaneous imaging.

The temporally averaged measurements are performed using three-phase SLIPI (3p-SLIPI) with liquid injection pressures in the range of 20–50 bar and at ambient conditions. Droplet sizing is obtained by combining SLIPI with the laser-induced fluorescence (LIF)/Mie ratio approach, where the droplet Sauter mean diameter is deduced after calibration with phase Doppler anemometry measurements. The droplet concentration and liquid volume fraction are obtained by combining the SLIPI-LIF/Mie method with light transmission measurements. This is performed using a laser sheet scanning approach, which provides three-dimensional quantitative reconstructions. Finally, the spray temperature is obtained by combining SLIPI with two-color LIF ratio thermometry for a liquid temperature ranging from 25–55°C. It is found that multiple light scattering induces measurement errors even for sprays having singly scattered photons in majority. This finding, therefore, strongly supports the application of SLIPI for quantitative spray measurements, even for optically dilute sprays. The 3p-SLIPI approach is based on recording a minimum of three modulated sub-images successively, each having a different spatial phase; therefore, it has been primarily used for temporally averaged imaging.

To circumvent this limitation, two novel instantaneous imaging approaches, 2p-SLIPI and 1p-SLIPI (corresponding to two-phase and one-phase, respectively), have been developed. In the 2p-SLIPI optical setup, the “lines structure” is optically shifted by exploiting the birefringence property of a calcite crystal. This novel optical approach is used to image spray dynamics in ethanol and butanol DISI sprays at liquid fuel injection pressures of 80 and 160 bar, where the spray chamber is operated at 2-bar air pressure. Finally, the results from instantaneous 2p-SLIPI and 1p-SLIPI imaging have been compared, showing promising applications for the study of spray dynamics.

Key words: SLIPI, Sprays, Multiple light scattering, LIF, Mie, droplet sizing, droplet concentration, thermometry

Classification system and/or index terms (if any)

Supplementary bibliographical information | Language: English

ISSN and key title: ISSN 1102-8718 | ISBN 978-91-7753-468-6

Recipient’s notes | Number of pages 207 | Price

Security classification

Droplet size, concentration, and temperature mapping in sprays using SLIPI-based techniques

DOCTORAL THESIS

Yogeshwar Nath Mishra
(योगेश्वर नाथ मिश्र)

Division of Combustion Physics,
Department of Physics, Faculty of Engineering

LUND
UNIVERSITY

Lund, Sweden
January 2018

Cover page illustration:
Mie sub-image of butanol DISI spray recorded at LTT Erlangen, Germany.

Lund University, Faculty of Engineering, Department of Physics
Lund Reports on Combustion Physics, LRCP-207
ISBN 978-91-7753-467-9 (printed)
ISBN 978-91-7753-468-6 (pdf)
ISSN 1102-8718
ISRN LUTFD2/TFCP-207-SE

Printed in Sweden by Media-Tryck, Lund University
Lund 2018

MADE IN SWEDEN

In memory of my mother, Gyanmati Mishra

उसको नहीं देखा हमने कभी
पर इसकी ज़रुरत क्या होगी
ऐ माँ, ऐ माँ तेरी सूरत से अलग
भगवान की सूरत क्या होगी, क्या होगी
उसको नहीं देखा हमने कभी

इन्सान तो क्या देवता भी
आँचल में पले तेरे
है स्वर्ग इसी दुनिया में
क़दमों के तले तेरे
ममता ही लुटाये जिसके नयन
ऐसी कोई मूरत क्या होगी
ऐ माँ, ऐ माँ तेरी सूरत...

क्यों धूप जलाए दुखों की
क्यों ग़म की घटा बरसे
ये हाथ दुआओं वाले
रहते हैं सदा सर पे
तू है तो अँधेरे पथ में हमें
सूरज की ज़रुरत क्या होगी
ऐ माँ, ऐ माँ तेरी सूरत...

कहते हैं तेरी शान में जो
कोई ऊँचे बोल नहीं
भगवान के पास भी माता
तेरे प्यार का मोल नहीं
हम तो यही जानें तुझसे बड़ी
संसार की दौलत क्या होगी
ऐ माँ, ऐ माँ तेरी सूरत...

--- मजरूह सुल्तानपुरी

Abstract

Structured laser illumination planar imaging (SLIPI) is a technique capable of suppressing multiple light scattering effects in optically dense sprays, resulting in spray images without blurs and with enhanced contrast. The novelty of the work presented in this thesis concerns the applications of a variety of SLIPI-based techniques for the measurement of droplet size, droplet concentration, and liquid temperature in atomizing sprays. Two types of spray systems are investigated here: 1) Steady hollow-cone water sprays using temporally averaged imaging.
2) Transient Direct-Injection spark ignition (DISI) biofuel sprays using instantaneous imaging.

The temporally averaged measurements are performed using three-phase SLIPI (3p-SLIPI) with liquid injection pressures in the range of 20–50 bar and at ambient conditions. Droplet sizing is obtained by combining SLIPI with the laser-induced fluorescence (LIF)/Mie ratio approach, where the droplet Sauter mean diameter is deduced after calibration with phase Doppler anemometry measurements. The droplet concentration and liquid volume fraction are obtained by combining the SLIPI-LIF/Mie method with light transmission measurements. This is performed using a laser sheet scanning approach, which provides three-dimensional quantitative reconstructions. Finally, the spray temperature is obtained by combining SLIPI with two-color LIF ratio thermometry for a liquid temperature ranging from 25–55°C. It is found that multiple light scattering induces measurement errors even for sprays having singly scattered photons in majority. This finding, therefore, strongly supports the application of SLIPI for quantitative spray measurements, even for optically dilute sprays. The 3p-SLIPI approach is based on recording a minimum of three modulated sub-images successively, each having a different spatial phase; therefore, it has been primarily used for temporally averaged imaging.

To circumvent this limitation, two novel instantaneous imaging approaches, 2p-SLIPI and 1p-SLIPI (corresponding to two-phase and one-phase, respectively), have been developed. In the 2p-SLIPI optical setup, the “lines structure” is optically shifted by exploiting the birefringence property of a calcite crystal. This novel optical approach is used to image spray dynamics in ethanol and butanol DISI sprays at liquid fuel injection pressures of 80 and 160 bar, where the spray chamber is operated at 2-bar air pressure. Finally, the results from instantaneous 2p-SLIPI and 1p-SLIPI imaging have been compared, showing promising applications for the study of spray dynamics.

Popular science abstract

When driving or walking on a foggy day, visibility is significantly reduced as light passing through the fog is randomly scattered by water droplets and redirected in all directions. If these droplets are present in great numbers, the light reaching our eyes loses information about what is in or behind, the fog. Similarly, but on a smaller scale, the light crossing a spray system is scattered, by a small cloud of micrometer-sized liquid droplets dispersed into a surrounding gaseous medium. Thus, the visibility in sprays is also significantly reduced, which makes their characterization very challenging.

Due to their virtue of distributing liquids over large surface areas, sprays have a wide range of applications, for example, the injection of liquid fuels in internal combustion engines, spray drying for the powder production of food and pharmaceuticals, spray painting, fire extinguishers, the pesticide treatment of crops in agriculture, and nasal sprays. Depending on their specific application requirements, sprays must be characterized in terms of their structure, droplet size distribution, droplet number density, liquid temperature *etc*.

Laser-sheet imaging techniques have been used to characterize sections of spray systems since the mid-1980s. The idea of the approach is to use a thin two-dimensional (2D) light sheet as a light source, a high-quality lens objective, and a scientific camera system to record spray images that are optically sectioned.

When light passes through a spray, the number of interactions between photons and droplets increase if more droplets are present (higher droplet number density) and/or if the dimensions of the spray are increased (larger spray volume). The singly scattered photons correspond to only one interaction between a photon and a droplet, thus, preserving the information related to the droplet. However, the multiply scattered photons carry information about the last interaction between the light-droplets, which is most frequently out-of-focus. Thus, the detection of multiply scattered photons produces unwanted out-of-focus optical signals due to which the recorded images suffer from reduced image contrast and blurs.

To address this issue, the “conventional” laser sheet, which consists of a homogeneous intensity profile, is modulated in space with a pattern of lines. This approach is known as SLIPI. The pattern of lines works as a “fingerprint” and

helps distinguish between the singly and multiply scattered photons.
During the last decade, SLIPI-based approaches have been used for spray imaging to address unwanted effects from multiple scattering.

In this thesis, a variety of SLIPI-based techniques have been developed for 2D and 3D measurement of spray related quantities such as: droplet size, liquid temperature, droplet concentration, *etc*. All those measured quantities have significant importance for determining the performance of spray systems and estimating their overall surface area.

List of publications

This dissertation is based on the research articles, referred to by their Roman numerals. The copies are appended at the end of the thesis.

I. **Y. N. Mishra**, E. Kristensson, E. Berrocal, *Reliable LIF/Mie droplet sizing in sprays using structured laser illumination planar imaging*, Optics Express 22 (4), 4480-4492 (2014).

II. **Y. N. Mishra**, F. Abou Nada, S. Polster, E. Kristensson, E. Berrocal, *Thermometry in aqueous solutions and sprays using two-color LIF and structured illumination*, Optics Express 24 (5), 4949-4963 (2016).

III. **Y. N. Mishra**, E. Kristensson, E. Berrocal, *3D droplet sizing and 2D optical depth measurements in sprays using SLIPI-based techniques*, Proceedings of the 18th International Symposium on the Application of Laser and Imaging Techniques to Fluids Mechanics, Lisbon (2016).

IV. M. Storch[†], **Y. N. Mishra**[†], M. Koegl[†], E. Kristensson, S. Will, L. Zigan, E. Berrocal, *Two-phase SLIPI for instantaneous LIF and Mie imaging of transient fuel sprays*, Optics Letters 41 (23), 5422-5425 (2016). [†]Equally contributed.

V. **Y. N. Mishra**, E. Kristensson, M. Koegl, J. Jönsson, L. Zigan, E. Berrocal, *Comparison between two-phase and one-phase SLIPI for instantaneous imaging of transient sprays*, Experiments in Fluids, 58,110 (2017).

VI. **Y. N. Mishra**, T. Tscharntke, E. Kristensson, E. Berrocal, *Measurement of droplet size, concentration, and liquid volume fraction in sprays using SLIPI-based techniques*, Manuscript to be submitted in Applied Optics (2018).

VII. M. Koegl, **Y. N. Mishra**, M. Storch, C. Conrad, E. Berrocal, S. Will, L. Zigan, *Analysis of ethanol and butanol DISI sprays using two-phase SLIPI LIF/Mie droplet sizing*, Manuscript submitted to International Journal of Spray and Combustion Dynamics (2017).

Related work

A. **Y. N. Mishra**, E. Kristensson, S.G. Pettersson, E. Berrocal, *Planar droplet sizing of a hollow-cone spray using SLIPI-LIF/Mie*, at the 25th European Conference on Liquid Atomization and Spray Systems, Chania, 2013.

B. **Y. N. Mishra**, E. Kristensson, M. Aldén, E. Berrocal, *Droplet size and concentration mapping in sprays using SLIPI-based techniques*, at the 26th Annual Conference on Liquid Atomization and Spray Systems, Europe, Bremen 2014.

C. **Y. N. Mishra**, S. Polster, F. Abou Nada, E. Kristensson, E. Berrocal, *Sprays thermometry using two color LIF and SLIPI*, at the 13th International Conference on Liquid Atomization and Spray Systems, ICLASS, Taiwan, 2015.

D. M. Koegl, **Y. N. Mishra**, M. Storch, E. Kristensson, S. Will, L. Zigan, E. Berrocal, *SLIPI-LIF/Mie droplet sizing for investigation of DISI sprays*, at the 27th Annual Conference on Liquid Atomization and Spray Systems, Europe, Brighton 2016.

E. M. Koegl, **Y. N. Mishra**, B. Hofbeck, K. Baderschneider, J. Pracht, E. Berrocal, S. Will, L. Zigan, *LIF/Mie planar droplet sizing in IC engine sprays using single-droplet calibration data*, Manuscript in preparation.

Acknowledgements

I express my sincerest thanks to all those who guided, helped, and participated in making my Ph.D. thesis work possible. First and foremost, my gratitude to the head of the division *Professor Marcus Aldén*, and to my supervisor *Dr. Edouard Berrocal,* for giving me an opportunity to work at the division. *Professor Aldén* has been a great source of inspiration for me and words are inadequate in describing him as a scientist and the head of the combustion physics division. He has always ensured competence, an enriching work environment and safety in the laboratories.

To my supervisor *Dr. Edouard Berrocal*, without whose guidance and utmost help this thesis would not have materialized. His deep knowledge of the subject, rigorous scientific reasoning, passion for trying out new ideas, meticulous experimental observations, hard-working nature, persuasiveness to attain perfection and timely advice became the motivators that guided me throughout these years. His constant encouragement and subtle criticism have been the source of strength that helped me cross the barriers at work and in my personal life.
I extend this acknowledgement to my co-supervisor *Dr. Elias Kristensson*, who has taught me several things and helped me improve my learnings. I admire him as researcher; his way of teaching science and bringing out the best in the student through encouragement is unique.

A fair share of my Ph.D. work has been the result of research visits at the Lehrstuhl für Technische Thermodynamik (LTT), Erlangen in Germany. The head of the LTT *Professor Stefan Will* has been very supportive. *Dr. Lars Zigan* has ensured very smooth and pleasant working environment in the laboratory. To *Dr. Michael Storch* for helping me with the instantaneous SLIPI experiments. Finally, yet importantly, I have to thank *Matthias Koegl,* who has worked very hard to make sure things are up and running in the laboratory. He possesses a special talent to produce best engineering solutions with ease. I would also like to thank *Sebastian Bornschlegel* and *Dr. Sebastian Riess*.

My sincere thanks to all the faculty members who gave courses and guest lectures at Lund University; they are *Prof. Per-Erik Bengtsson*, *Prof. Mattias Richter*,

Prof. Joakim Bood, *Prof. Öivind Andersson*, *Prof. Per Tunestål*, *Dr. Zhongshan Li*, *Dr. Sven-Inge Möller* and *Dr. Sven Huldt*. To the senior researchers *Dr. Fredrik Ossler*, *Dr. Robert Collin* and *Dr. Andreas Ehn* with whom I have interacted on several occasions for help and discussions, my sincere thanks. A special mention to *Minna Ramkull* and *Cecilia Bille,* administrative personal at the division, for helping me get through most of the formalities and tedious paperwork whenever needed. To our technician *Igor Buzuk*, who has always been there to sort out any computer-related issues at work.

I was lucky to have shared the office space with *Jinlong Gao*, who has always tried to help me. I will always remember the long talks we had about world politics and personal- and work-related matters. I am sure we are both going to miss our "hellos'' and "very goods''. I would like to thank all my present and previous colleagues at the division; they are *Joakim Jönsson*, *Alexios Matamis*, *Panagiota Stamatoglou*, *Elin Malmquist*, *Kajsa Larsson*, *Dina Hot*, *Ali Hosseinnia, Zhenkan Wang*, *Christoffer Pichler*, *Maria Ruchkina*, *Arman Subash*, *Manu Mannazhi*, *Stephanie Polster*, *Dr. Jiajian Zhu and Dr. Fahed Abou Nada. Fahed* has been very helpful as a senior. I have learnt a lot while working with him on the SLIPI-two color LIF thermometry project. I thank *Dr. Atanu Kundu* for his encouragements and guidance.

I truly appreciate the teaching and supervision that I have received from *Prof. Dag Hanstorp* at Gothenburg University, *Dr. Samarendra Mohanty* at the University of Texas at Arlington, *Prof. V. P. N Nampoori*, *Prof. P. Radhakrishnan*, *Prof. Sheenu Thomas* and the late *Prof. Annie Joseph Vallamattom* at CELOS.

Whatever I have achieved so far is because of the constant support of my parents and my family. I begin with mentioning my grandparents, the late shri *Devidutt Mishra* and the late shrimati *Kaulvashi Mishra*. I would like to make a special mention of my father, *Rajendra Nath Mishra*, my mother the late *Gyanmati Mishra* and all my elders *Anil, Chanda*, *Tara*, *Roopa*, *Deepika* and my younger brother *Kamalendra*.They have always been there for me. I also extend my acknowledgment to families of my sisters and brothers.

To my in-laws, the late *Dr. Narendra Kumar Tiwari* and *Saroj Tiwari,* I express my sincere thanks. Lastly Bhawana, I thank you for your constant support. I consider myself very lucky to have you as my life partner. You soak up all my worries and keep me positive. Thank you for giving me the precious gift of my life, our daughter *Aashvi*!!

List of contents

Acronyms

CW	Continuous Wave
DISI	Direct Injection Spark Ignition
EM-CCD	Electron-Multiplying Charged Coupled Device
FOV	Field-of-view
FWHM	Full Width at Half Maximum
GDI	Gasoline Direct Injection
IC	Internal Combustion
LIEF	Laser-induced Exciplex Fluorescence
LIF	Laser-induced Fluorescence
LIP	Laser-induced Phosphorescence
LSD	Laser Sheet Drop-sizing
PDA	Phase Doppler Anemometry
PDI	Phase Doppler Interferometry
PDS	Planar Droplet Sizing
PIV	Particle Image Velocimetry
sCMOS	Scientific Complementary Metal-Oxide-Semiconductor
SLIPI	Structured Laser Illumination Planar Imaging
SMD	Sauter Mean Diameter
SNR	Signal-to-Noise Ratio
1p-SLIPI	One-phase SLIPI
2p-SLIPI	Two-phase SLIPI
3p-SLIPI	Three-phase SLIPI

1. Introduction

The development and application of laser diagnostic techniques over the past three decades have helped to better understand the basic physics and mechanisms of spray formation and droplet transport. This improved knowledge of spray-related phenomena has, in turn, led to the improvement and further development of spray combustion systems with improved efficiency and reduced emissions [1-3]. Such combustion systems include internal combustion engines, such as diesel and spark ignition, gas turbine combustors, and liquid-fueled rocket engines.

The complete characterization of spray systems is often highly desired in combustion research; however, this is very difficult to achieve, as it requires a combination of a number of different experimental approaches to measure different parameters [4]; each diagnostic has its advantages and limitations [5, 6]. The spray characterization consists of knowing the internal flow within the spray nozzle, the liquid disintegration characteristics, the liquid sheet thickness, the flow velocity, the spray cone angle, the spray evaporation rate, the droplet size distribution, and the droplet concentration [7]. In spray assisted internal combustion engines, the reliable measurement of spray quantities, such as droplet size distribution and spray evaporation, plays a significant role in determining uniform fuel/air mixing and minimal wall-wetting [8].

The fully developed spray is a 3D scattering medium, consisting of a non-homogeneous distribution of droplet [9]. Therefore, optical diagnostics capable of yielding this information at least in 2D are preferable. One of the most common optical methods for the 2D mapping of flows is laser sheet imaging, which is also known as planar laser imaging. The technique optically sections the probed region by means of a sheet of laser light, providing a rapid evaluation of sprays and has been extensively used in the past three decades for spray measurements [4] and combustion diagnostics [10, 11]. Using laser sheet-based techniques, several important quantities, such as flow velocity, droplet SMD, droplet concentration, and spray temperature, can be measured. The spray quantities and their corresponding measurement approaches are listed in Table 1. Note that all those mentioned measurement techniques work on *single scattering approximation*, which refers to the assumption that only singly scattered photons from the probed spray medium are detected by the camera. Most sprays are, however, optically

dense [6, 12], and thus *single scattering approximation* is not respected when imaging such systems. Likewise, other optical diagnostics planar laser imaging also experiences effects such as light extinction [13-15], and multiple scattering [16]. The photons crossing an optically dense sample exit in majority as multiply scattered photons and the singly scattered photons are significantly reduced [17]. Therefore, *single scattering approximation* for quantitative laser sheet imaging is only valid for sprays having a low number density of droplets and samples with a short optical path.

Table 1. Laser sheet-based techniques for quantitative spray imaging

Spray quantities	Laser sheet-based techniques
Flow velocity	Particle Image Velocimetry [18-20]
Droplet SMD	LIF/Mie intensity ratio [21-23], Raman/Mie intensity ratio [24], LIEF/Mie intensity ratio [25]
Spray and droplet temperatures	Two-color LIF intensity ratio [26-28], Two-color LIP intensity ratio [29, 30], Two-color LIEF intensity ratio [31, 32]
Liquid and vapor phase fuel distribution	LIEF intensity [33-35]
Fuel concentration	LIF of fuel [36-38], Signal attenuation [39]
Optical Depth	Light transmission measurements [9], SLITI [40]
Extinction-coefficient	SLIPI-scan [41], Dual-SLIPI [42]
Liquid volume fraction	Dual Infrared Mie extinction [43], fuel LIF [44]

To address multiple light scattering issues in laser sheet imaging, a technique called SLIPI was introduced in 2008 [45, 46]. Thanks to this new imaging approach, the image blur caused by multiple scattering could be addressed, resulting in spray images with improved image contrast. The heart of the SLIPI technique resides in using a laser sheet having a spatially modulated intensity pattern. This structured laser sheet illumination represents a sinusoidal or a square intensity pattern. When crossing the spray, photons interact with the droplets either once or several times depending on the turbidity of the medium [16]. On the detector, both singly and multiply scattered photons are collected; however, the singly scattered photons "remember" the structured information. On the contrary, multiply scattered photons readily lose the given recognizable signature. Therefore, it becomes possible to distinguish between the intensity of singly and multiply scattered photons. Using a mathematical post-processing algorithm [47], the intensity of singly scattered photons is retained as well as demodulation of the structured light pattern. Figure 1 illustrates the detection of Mie scattered light

using this approach, also known as 3p-SLIPI, in which the sinusoidal-modulated laser sheet is traversing the center of a steady-state hollow-cone water spray.

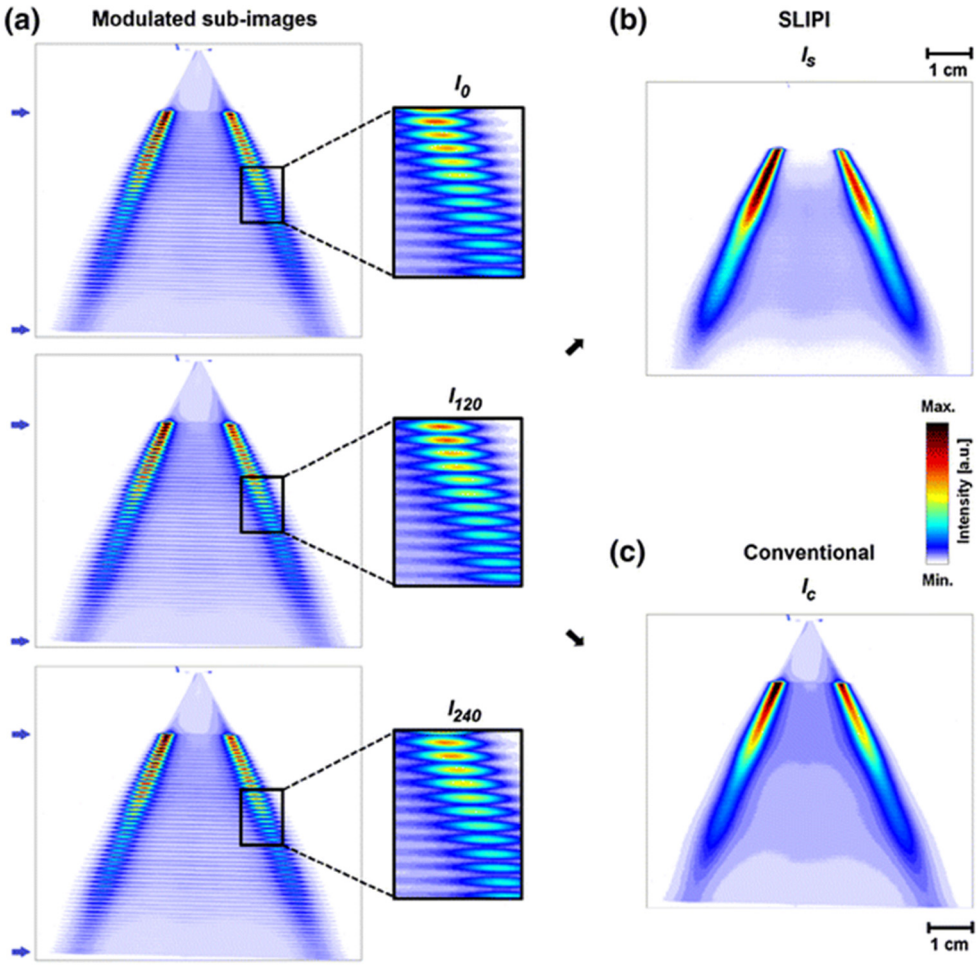

Fig. 1: Illustration of the 3p-SLIPI approach: The laser sheet having a sinusoidally-modulated intensity pattern along the vertical direction is intersecting a hollow-cone water spray. (a): Shows the three sub-images of the Mie scattered signal where the line-pattern is vertically moved one third of the spatial period. (b) and (c): Show the images of the SLIPI and "conventional" laser sheet, respectively, which are deduced using three sub-images in Eq. 2 and Eq. 3, respectively. The "conventional" image suffers from effects of multiple scattering, while in the SLIPI image those effects are reduced. From paper V.

If a sinusoidal pattern is superimposed upon the light sheet, the resulting image intensity $\boldsymbol{I(x,y)}$ is described as:

$$\boldsymbol{I(x,y) = I_c(x,y) + I_s(x,y) \cdot sin(2\pi xv + \phi)} \qquad \textbf{(1)}$$

$\boldsymbol{\nu}$ **:** Spatial frequency of the modulation, $\boldsymbol{\phi}$**:** Spatial phase.
$\boldsymbol{I_c(x,y)}$**:** Intensity corresponding to singly and multiply scattered photons ("conventional").
$\boldsymbol{I_s(x,y)}$**:** Amplitude of the modulation from the singly scattered photons (SLIPI).

To extract the information corresponding to $\boldsymbol{I_s(x,y)}$ in Eq. 1, three intensity "modulated sub-images," $\boldsymbol{I_0}$, $\boldsymbol{I_{120}}$, and $\boldsymbol{I_{240}}$ need to be recorded, having the respective spatial phases of 0°, 120°, and 240°, as shown in Fig. 1(a). Using these sub-images, a SLIPI image shown in Fig. 1(b) can be constructed from the root-mean-square of the differences between sub-image pairs, described mathematically as:

$$\boldsymbol{I_s = \frac{\sqrt{2}}{3} \cdot \left[(I_0 - I_{120})^2 + (I_0 - I_{120})^2 + (I_{120} - I_{240})^2\right]^{\frac{1}{2}}} \qquad (2)$$

A "conventional" laser sheet image, shown in Fig. 1(c), including both the multiply and singly scattered photons can be constructed by extracting the average of the three modulated images as:

$$\boldsymbol{I_c = (I_0 + I_{120} + I_{240})/3} \qquad (3)$$

As shown in Fig. 1(c), due to the effects of multiple scattering, unwanted light intensity contributions are detected in non-illuminated sections. These undesired effects are not present in the corresponding SLIPI image. A detailed comparison between SLIPI and "conventional" laser sheet imaging for both scattering- and fluorescing media with different particle sizes and different optical depths is given in reference [48]. The 3p-SLIPI approach has been employed mainly for temporally averaged imaging due to the requirement of a minimum of three sub-images. An instantaneous imaging 3p-SLIPI setup [49] has been demonstrated, which demands the recombination of three laser pulses, each passing through a separate grating and arriving at the collecting lens within a time difference of a few hundreds of nanoseconds to "temporally freeze" the spray motion. This recombination of three independent optical channels results in large laser power losses. It also requires the use of both three intensified camera detectors and three pulsed laser sources, thus, largely increasing the cost of the system and the complexity of the optical arrangement. To circumvent these challenges, 3p-SLIPI has been extended to two additional SLIPI approaches; 2p-SLIPI requiring two sub-images and 1p-SLIPI requiring a single sub-image [47]. These two additional SLIPI approaches have been employed for instantaneous imaging in sprays in this thesis. The SLIPI-based techniques used for 2D/3D mapping of quantities in sprays and the 2D/3D imaging of species in flames are listed in Table 2.

Table 2. SLIPI-based techniques for quantitative spray/flame imaging

Spray/flame quantities	SLIPI-based techniques
Dropet SMD	SLIPI-LIF/Mie intensity ratio[50-53]
Spray thermometry (Liquid phase and gas phase)	SLIPI-two-color LIF intensity ratio[54] SLIPI-two-color LIP intensity ratio[55]
Spray extinction-coefficient	SLIPI-scan[41, 56], Dual-SLIPI[42]
Spray Optical Depth	SLIPI-scan[9], SLITI[40]
Flame temperatures	SLIPI-Rayleigh thermometry[57, 58]
OH photo fragments in flame	SLIPI-photo fragmentation LIF[59]
Formaldehydes in flame	SLIPI-FRAME with CH_2O-PLIF[60]

The aim of the research work presented in this thesis is the development and application of several SLIPI-based techniques for measuring the droplet size (SMD), spray temperature, droplet number density, and liquid volume fraction in sprays. Table 3 lists the papers related to the quantitative SLIPI imaging in steady hollow-cone (HC) sprays and transient DISI biofuel sprays.

Table 3. SLIPI-based measurements with the publications listed in this thesis

SLIPI-based methods	Droplet size	Droplet concentration	Liquid volume fraction	Droplet temperature	Qualitative imaging
Averaged SLIPI in HC sprays	Paper I, Paper III, Paper VI	Paper VI	Paper VI	Paper II	Paper III
Averaged SLIPI in DISI sprays	Paper VII				
Instantaneous 2p-SLIPI					Paper IV, Paper VII
Instantaneous 1p-SLIPI					Paper V

1.1 Outline of the thesis

The outline of this thesis is as follows:

Chapter 2 provides a short introduction to the basics of atomizing sprays. The influencing parameters governing the atomization process are discussed. Spray drop size distributions and spray drop evaporation are introduced. Finally, steady and transient spray systems are described.

Chapter 3 introduces the light propagation through the spray region and interaction with the surrounding droplets. The extinction of light and multiple light scattering phenomena are discussed.

Chapter 4 describes the laser sheet imaging techniques for spray characterization. Intensity ratio techniques, such as LIF/Mie droplet sizing and two-color LIF thermometry, are reviewed.

Chapter 5 reports the temporally averaged 3p-SLIPI-based approaches requiring a triplet of sub-images for the reconstruction of a SLIPI image. SLIPI is combined with LIF/Mie ratio planar droplet sizing in steady hollow-cone sprays for droplet SMD measurements. The combined SLIPI-LIF/Mie and SLIPI-scan setup is used to simultaneously measure the droplet SMD, droplet concentration, and liquid volume fraction. Finally, SLIPI is combined with the two-color LIF ratio approach for 2D temperature mapping of droplet in aqueous solutions and in steady hollow-cone sprays.

Chapter 6 presents the instantaneous SLIPI approaches; 2p-SLIPI and 1p-SLIPI. In the first sub-section, the 2p-SLIPI is described along with the post-processing algorithm of the sub-images. In the second part, 1p-SLIPI is discussed with the post-processing routine. Finally, 2p-SLIPI in combination with LIF/Mie droplet sizing is reported for the ethanol and butanol DISI sprays.

Chapter 7 concludes and summarizes the presented work together with future considerations.

2. Sprays and their applications

This chapter provides a short introduction to the basics of atomizing sprays. The influencing parameters governing the atomization process are discussed. Spray drop size distributions and droplets evaporation are introduced. Finally, steady and transient spray systems are also described.

2.1 Basics of atomizing sprays

One of the main functions of atomizing sprays is the deposition of liquids over a large surface area [61]. It is usually performed by injecting a liquid flow at a high pressure of injection into a gaseous environment. The interaction between the liquid flow and the surrounding gas leads to a rapid disintegration of the liquid into large liquid bodies and then small droplets, thus enhancing the surface area drastically. Atomizing sprays are used in several applications, ranging from pharmaceuticals to combustion engineering. For example, drug delivery in medical therapy, pesticides treatment in agriculture, surface cleaning, fuel/air mixing in the internal combustion engines, spray coatings at small scale for pills fabrication, spray painting, spray drying for powder fabrication, to mention a few applications [62]. Therefore, the use of spray systems in the modern world has become ubiquitous. The use of sprays depends largely on their suitability, and longevity in correct process repetition. Thus, it is essential to control and optimize the spray formation processes and the characteristics of the formed spray. According to Rayleigh [63], the breakup mechanism of an injected liquid depends on the fluid properties, the jet diameter, and the corresponding outlet velocity [64]. The jet breakup length in the quiescent air as a function of outlet velocity can be categorized into five different regimes as shown in Fig. 2: Dripping (**I**), Rayleigh breakup (**II**), First wind-induced breakup (**III**), Second wind-induced breakup (**IV**), and Atomization (**V**) [65]. The interface between different regimes can be defined by the corresponding Weber numbers. The Weber number $\boldsymbol{We_l}$ is the ratio of the inertia forces to the surface tension forces [66] and can be expressed as:

$$\boldsymbol{We_l = \frac{\rho_l \cdot v_l^2 \cdot d_l}{\sigma}} \qquad (4)$$

$\boldsymbol{\rho_l}$: Density of the liquid jet, $\boldsymbol{v_l}$: Velocity of the liquid jet, $\boldsymbol{\sigma}$: Surface tension coefficient, $\boldsymbol{d_l}$**:** Characteristic length of the liquid flow (here the jet diameter)

Due to the contribution of the density of the surrounding gaseous medium, $\boldsymbol{\rho_g}$ in regimes III-V, the Weber number $\boldsymbol{We_g}$ affected by the surrounding gas is derived as:

$$\boldsymbol{We_g = \frac{\rho_g \cdot v_l^2 \cdot d_l}{\sigma}} \qquad (\mathbf{5})$$

Here, Different regimes in Fig. 2 are described by Bonhoeffer *et al.* [65] as follows:
I: In the dripping regime, the outlet velocity is very low; therefore, the liquid accumulates at the nozzle tip until it drips from it.
II: In the Rayleigh regime, with increasing velocity, an axis-symmetrical jet is generated, which breaks up into single droplets of uniform size.
III: In the first wind-induced breakup, a further increase in outlet velocity leads to a decreasing breakup length, mainly caused by air friction.

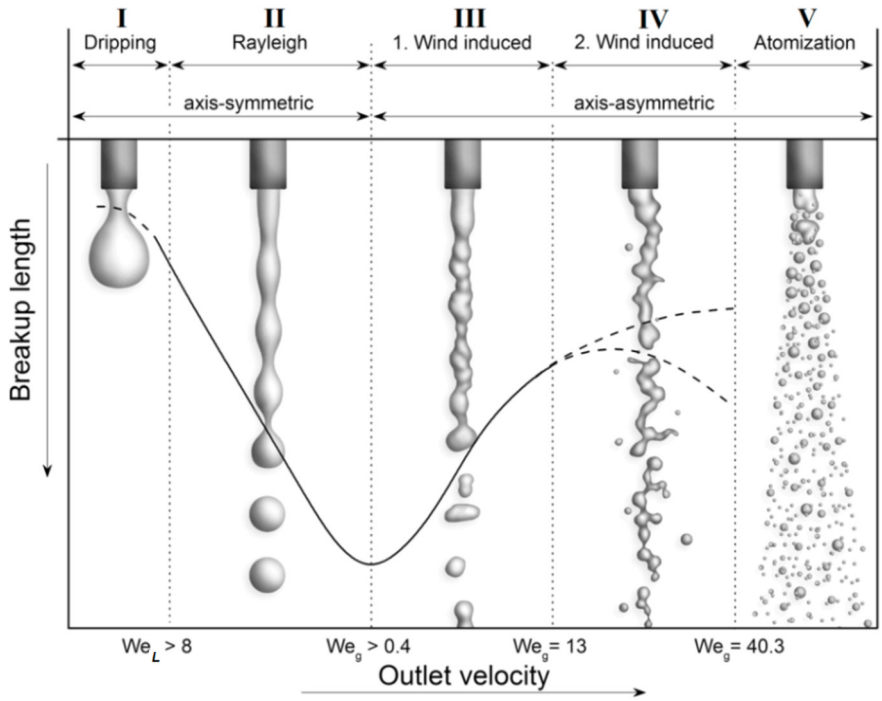

Fig. 2: Illustration of the breakup regimes of round liquid jets in the quiescent air. Impact of outlet velocity on breakup length of injected liquid from a circular nozzle; I: Dripping; II: Rayleigh breakup; III: First wind-induced breakup; IV: Second wind-induced breakup; V: Atomization. From reference [65].

IV: In the second wind-induced breakup, even higher velocities and increased air resistance lead to surface rupture and separation of single droplets from the jet.

V: At very high velocities, atomization occurs, where the separation into small droplets occurs right at the nozzle exit with the breakup length being close to zero.

Two other important non-dimensional numbers associated with spray atomization characteristics are the Reynolds number, $\boldsymbol{Re}$, and the Ohnesorge number, $\boldsymbol{Oh}$, which are defined as:

$$\boldsymbol{Re} = \frac{\boldsymbol{\rho_l \cdot v_l \cdot d_l}}{\boldsymbol{\mu_l}} \tag{6}$$

$\boldsymbol{\mu_l}$: Dynamic viscosity of the liquid.

$$\boldsymbol{Oh} = \frac{\sqrt{\boldsymbol{We}}}{\boldsymbol{Re}} \tag{7}$$

The $\boldsymbol{Re}$ is the ratio of inertial forces to the viscous forces. The $\boldsymbol{Oh}$ is the ratio of viscous forces to the surface tension forces. Figure 3 shows the plot of the $\boldsymbol{Oh}$ against the $\boldsymbol{Re}$ for different break-up regimes. It is used to estimate whether the atomization is poor or strong. For example, the strong atomization of diesel injectors lies in the $\boldsymbol{Oh}$ of range $\boldsymbol{0.01 \geq Oh \geq 0.1}$, and $\boldsymbol{Re \geq 10000}$ **[67].**

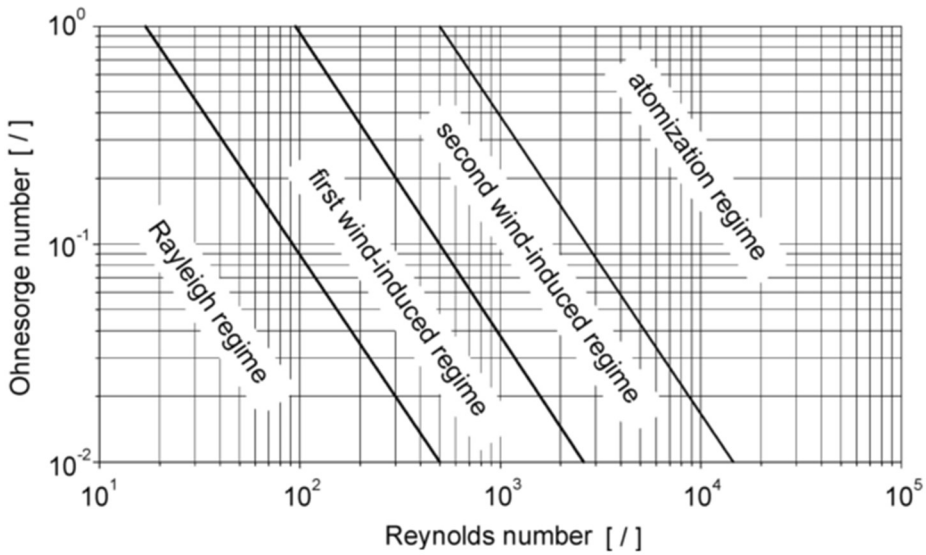

Fig. 3: The Ohnesorge diagram of a jet break-up. From reference [68].

Depending on the properties of the flows and operating conditions, a wide variety of sprays can be produced. As shown in Fig. 4, atomizing sprays can be categorized into two regions: the spray formation region **(1)**, and spray region **(2)**.

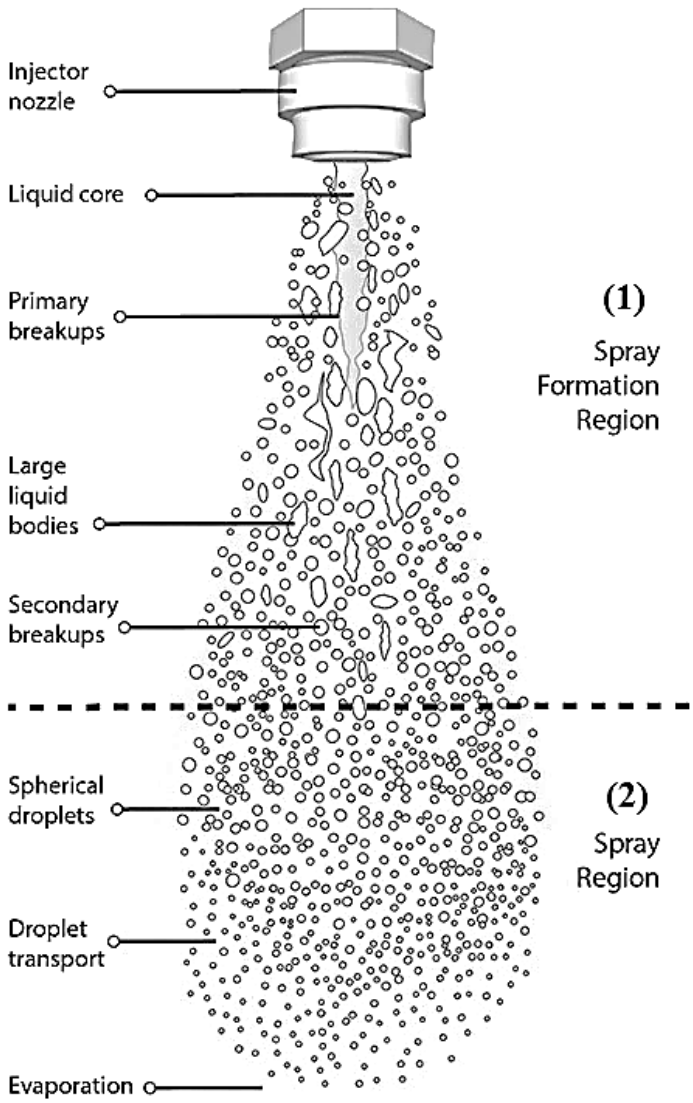

Fig. 4: Atomizing sprays can be categorized into two regions: the spray formation region (1), and the spray region (2). The first region consists of primary and secondary atomization. In the spray region (2), the spray is expected to be fully developed and most of the droplets are assumed to be spherical. Source: www.spray-imaging.com.

The spray formation region **(1)** is located directly downstream from the nozzle exit and is characterized by:

- The extension of the injected liquid body into a liquid core - or a liquid sheet.
- The primary break-up consists of formation of ligaments and large liquid structures.
- The secondary break-up occurs after the primary breakup where the large irregular liquid bodies breakup a second time into both non-spherical and spherical droplets. Note that the large non-spherical drops might break-up into a small droplet.

The spray region **(2)** is located in the far-field region, where the flow is fully dispersed and forms cloud of droplets evolving in a surrounding gaseous medium. Here, each spray droplet has its own characteristics such as diameter and velocity. Droplets may collide and coalesce with each other. The important spray characteristics in this region are:

- The drop-size distribution.
- The drop-velocity distribution.
- The droplet number density (number of droplets per unit volume).
- The local liquid volume fraction.
- The drop temperature.

The focus of the presented thesis work mainly deals with the characterization of the spray region in terms of droplet size, droplet number density, and spray temperature.

2.2 Droplet size distribution and evaporation

The atomization process yields to droplets of different size, usually ranging from a few microns up to several hundred microns. Several droplet size distributions have been reported in the literature [69], and one of the most commonly used expressions is the Rosin-Rammler equations [70]. Spray drops of different sizes can be presented either in terms of number or volume (mass). In many applications, only the mean diameter instead of the complete drop size distribution is used. A list of mean diameters and their related field applications are given in table 4. These mean diameters can be expressed differently based on the droplet diameter exponents $\boldsymbol{p}$ and $\boldsymbol{q}$ in Eq. 8:

$$\boldsymbol{D_{pq}} = \left[\frac{\sum_{i=1}^{\infty} \boldsymbol{n_i} \cdot \boldsymbol{D_i}^{\boldsymbol{p}}}{\sum_{i=1}^{\infty} \boldsymbol{n_i} \cdot \boldsymbol{D_i}^{\boldsymbol{q}}}\right]^{1/(p-q)} \qquad (8)$$

$\boldsymbol{D_i}$ **:** Diameter of the ith droplet
$\boldsymbol{n_i}$ **:** Number of the ith droplet
$\boldsymbol{p}$ and $\boldsymbol{q}$ **:** Values 0, 1, 2, 3, or 4

Table 4. Definition, mean diameter, and their applications

Definition	Mean diameter	Field of application
D_{10}	Arithmetic mean diameter	Evaporation rate
D_{20}	Surface area mean diameter	Monitoring surface applications
D_{21}	Area-length mean diameter	Absorption studies
D_{30}	Volume mean diameter	Hydrology and mass flux applications
D_{31}	Mean evaporative diameter	Evaporation and diffusion applications
D_{32}	Volume/surface mean diameter or Sauter mean diameter	Mass transfer and reaction
D_{43}	Mean diameter over volume or De Broukere diameter	Combustion applications

The mean diameter of a droplet with the same ratio of volume to surface area as the entire ensemble is denoted as the SMD. It corresponds to values of p = 3 and q = 2 in the above equation due to volumetric and surface dependence.

Using the histogram of spherical droplet distribution given in Fig. 5, different mean diameters are deduced using Eq. 8. From the calculations, it is found that these mean diameters are different from each other. Due to volumetric and surface area dependence, D_{32} and D_{43} are strongly representative of the large droplets even if their number density is less in numbers in comparison with the small droplets.

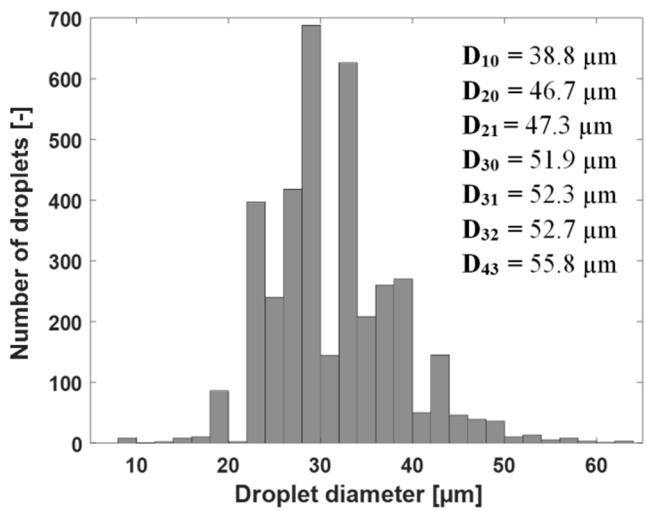

Fig. 5: Example of different mean diameters calculated using Eq. 8. It is deduced from the histogram of droplet size distribution.

The evaporation of spray droplets is a phase transition process by which molecules in a liquid overcome their intermolecular attraction forces and escape into the surrounding gaseous environment [71]. With an increase in liquid temperature, the kinetic energy of the liquid molecules is increased, which results in an increased evaporation activity. Another relevant parameter for enhancing the spray evaporation rate is the reduction of the ambient pressure, which increases the chances of the liquid molecules near the surface to overcome their intermolecular attraction potential. The evaporation of a single droplet is described by the d^2 law model [71]. Using this model, the evaporation of a droplet of diameter $\boldsymbol{d}$ at constant temperature can be described as a function of time $\boldsymbol{t}$:

$$\boldsymbol{d(t)^2 = (d_0 - \beta t)} \qquad (9)$$

$\boldsymbol{d}$: Droplet diameter
$\boldsymbol{d_0}$: Droplet diameter at the beginning of evaporation
$\boldsymbol{\beta}$: Evaporation coefficient

The evaporation coefficient depends on the droplet surface temperature [72] and thus, it is very important to know the actual surface temperature for the prediction of spray evaporation [73]. A detailed description of spray evaporation has been reviewed in reference [71].

2.3 Steady sprays

Sprays can be produced either as steady sprays from continuous injection of the liquid or as transient sprays produced from the pulsed injection of liquid. An example of steady sprays is the pressure-swirl atomizers. The pressure-swirl steady hollow-cone sprays and steady full-cone sprays are used for industrial applications such as spray cooling, spray drying, and dust control. In pressure-swirl atomizers, liquid flow into the swirl chamber via tangential ports. The rotation of the flow in the swirl chamber gains centrifugal forces, which lead to the formation of a liquid sheet. The liquid sheet further disintegrates into ligaments and then into fine drops. The patternation attains the two most common axisymmetric spray shapes of hollow-cone spray and the full-cone spray. The patternation defines both the shape of the spray boundary and the distribution of droplets within the boundary. Here, the mass flux distributions are controlled by the design of the nozzle orifice. The hollow cone design is used more frequently because of its ability to create finer droplets. Figure 6 shows the spray patternations for an axial flow design of a hollow-cone spray, and a full cone spray. It is seen that in a hollow-cone spray, most of the mass of the liquid is deposited on the outer edges, while in a full cone spray the liquid distribution is

even. The nozzle (Order no. 2163243, Lechler UK) producing a hollow-cone spray has been characterized in terms of droplet size, droplet concentration, liquid volume fraction, spray temperature, and optical depth mapping in chapter 5.

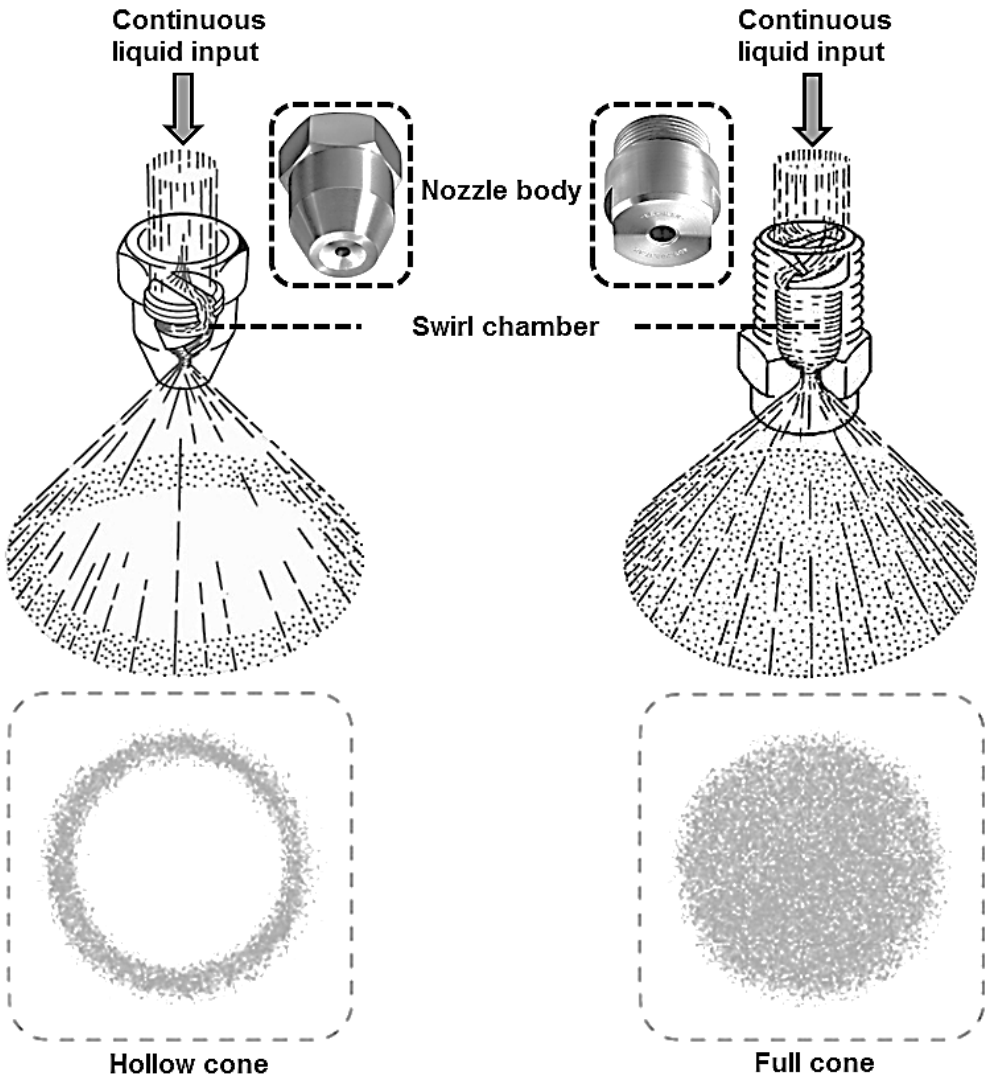

Fig. 6: Flow field schematic of a steady hollow-cone and a full cone spray nozzle (Lechler UK manual). It can be seen that in a hollow-cone spray, the mass of the liquid is deposited on the outer edges, while in full cone spray the liquid distribution is evenly distributed from the center to outer edges (images from Tecpro Australia).

2.4 Transient sprays

The transient injection is used in fuel injection systems in IC engines. The transient injectors provide fuel during short needle openings of varying duration, with a constant rate of flow during each electric pulse. Examples of transient spray systems are GDI sprays and Diesel sprays. The cross-section of a typical fuel injector is shown in Fig. 7, which corresponds to a common rail system. The fuel is guided to the injector at high pressure (from a few hundred up to 2000 bar). The fuel is sprayed from the nozzle orifice that is opened and closed with a needle valve, operated with a solenoid. The solenoid is connected with electrical attachment to receive the electric current. When the solenoid is not activated, the spring forces the needle valve into the nozzle passage and prevents the injection of fuel into the cylinder. The solenoid lifts the needle valve from the valve seat, and fuel under pressure is sent in the engine cylinder.

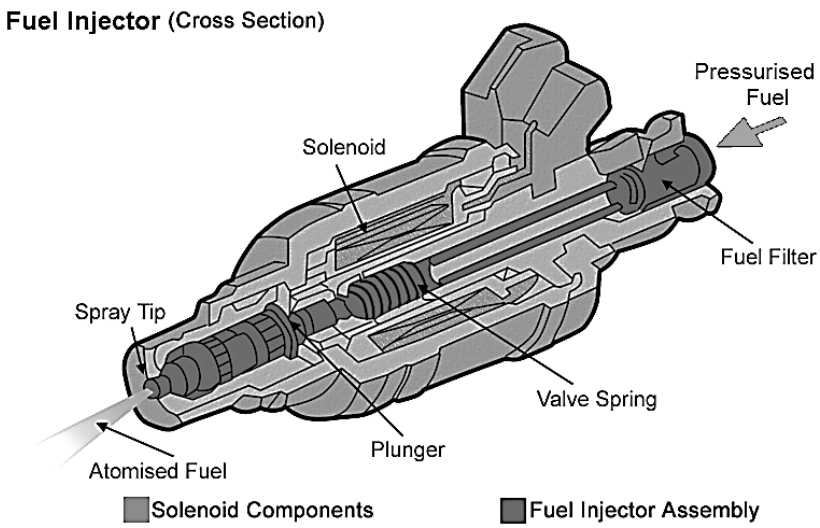

Fig. 7: The cross-section of a common rail fuel injector. From reference [74].

Figure 8 shows an example of a multi-hole GDI injector (Robert-Bosch GmbH Germany), followed with single-shot images of ethanol DISI sprays generated from a single hole. Four single-shot images are recorded with "conventional" laser sheet imaging at times after the visible start of injection, t_1 = 2300 μs, and t_2 = 2550 μs. The injection duration is kept constant to 1800 μs. The spray chamber is operated at 2 bar and 25°C, which represents a high load engine operation. The fuel temperature is fixed at 25°C, and the injection pressure is set to 160 bar. It can be observed from these 2D images that spray shape evolves as a function of time. Also, the spray structures vary from shot-shot injections. Such spray systems are

defined as transient sprays and require optical systems capable of "temporally freezing" the spray in motion.

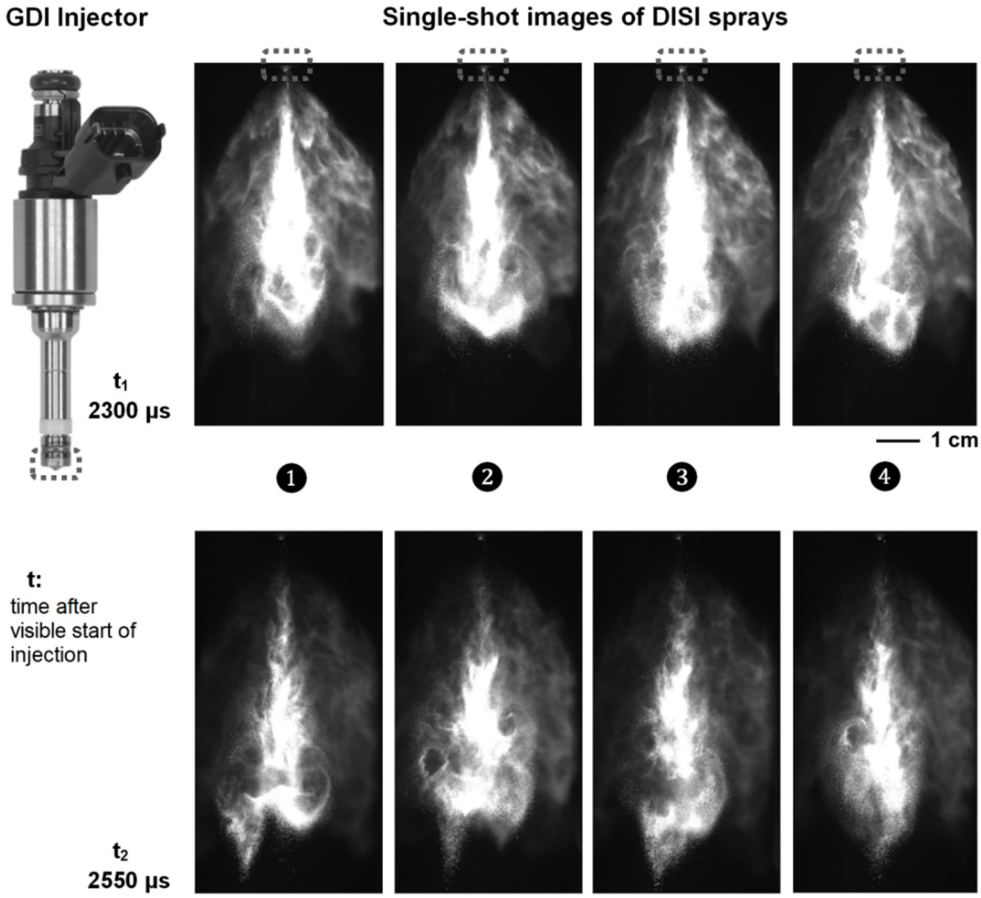

Fig. 8: Image of a GDI injector (from Robert-Bosch GmbH) with four examples of single-shot images for a non-combusting ethanol DISI spray. Two times of visible start of injections, t_1 = 2300 µs, and t_2 = 2550 µs have been considered.

3. Imaging through the spray region

This chapter introduces light propagation through the spray region and its interaction with the surrounding droplets. The extinction of light and multiple light scattering phenomena are described.

3.1 Light scattering by a single droplet

Mie scattering for light/droplet interaction is described by Lorenz-Mie theory [75]. Based on the size parameter $\boldsymbol{x}$, the light/droplet interaction falls within three light scattering regimes:

$\boldsymbol{x \ll 1}$: Rayleigh scattering regime

$\boldsymbol{1 < x < 100}$: Mie scattering regime

$\boldsymbol{x > 100}$: Geometrical optics regime

Here, $\boldsymbol{x}$ is given as:

$$\boldsymbol{x = \frac{\pi d}{\lambda}} \qquad (\mathbf{10})$$

d : Droplet diameter
λ : Wavelength of the incident light

Figure 9 shows plots of scattered light intensity as a function of the size parameter for water droplet of diameter in the range of 0.01-100 μm. The surrounding medium is air in this case. The relationship is investigated at the incident light of the wavelength of 488 nm, and for two scattering angles of 30° and 90° for parallel polarized light. In the Rayleigh scattering regime, the light intensity scattered from each light/droplet interaction is proportional to the sixth power of the diameter. This regime is suitable for particle size smaller than the wavelength of incident light. The Mie scattering regime is a transition between the Rayleigh scattering regime and the geometrical optics regime. In Mie scattering regime, a non-

monotonic and highly fluctuating relation between the scattered light intensity and size parameter can be seen. These fluctuations occur due to the interference of light scattered from the droplet with different scattering orders. This relationship can be made semi-monotonic by using an incoherent white light source [76] or setting the scattering angle to 60° [77].

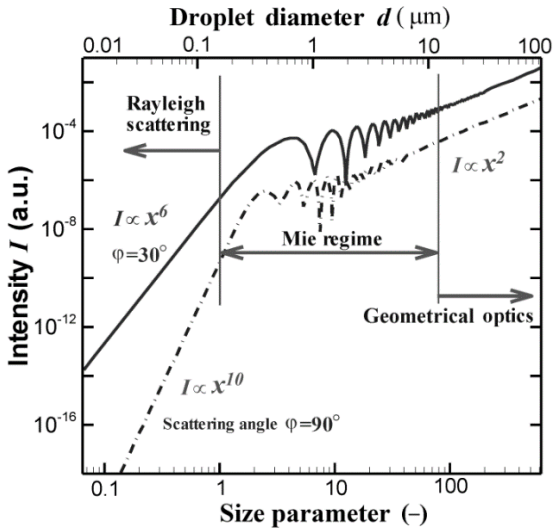

Fig. 9: Scattered intensity as a function of size parameter and droplet diameter. Based on the size parameter, three different regimes of light-droplet interaction can be identified. Adapted from reference [78].

The third regime is governed by geometrical optics. This regime dominates when the droplet diameter is much larger as compared to the wavelength of the incident light. In this regime, the scattered light intensity is proportional to droplet diameter square. Figure 10 shows plots of the scattering phase function for the three scattering regimes indicated in Fig. 9. The scattering phase function gives the angular distribution of light intensity scattered by a droplet at a given wavelength. Using Lorenz-Mie theory, linear and logarithmic plots are calculated for an incident wavelength of 488 nm for water droplet of three sizes; 0.1 μm, 10 μm, and 100 μm. It is seen in Fig. 10(a) that in the Rayleigh scattering regime, light scatters in all directions. However, in Fig 10(b), it is observed that in the Mie regime, most of the light scatter in the forward direction after a scattering event. In the geometrical optics regime, given in Fig. 10(c), light scatter strongly in the forward direction.

Using geometrical optics, several phenomena can be described when light interacts with a droplet, for example, diffraction, and absorption of light as illustrated in Fig. 11 (a). The reflection and refraction of the light beam crossing at the interface

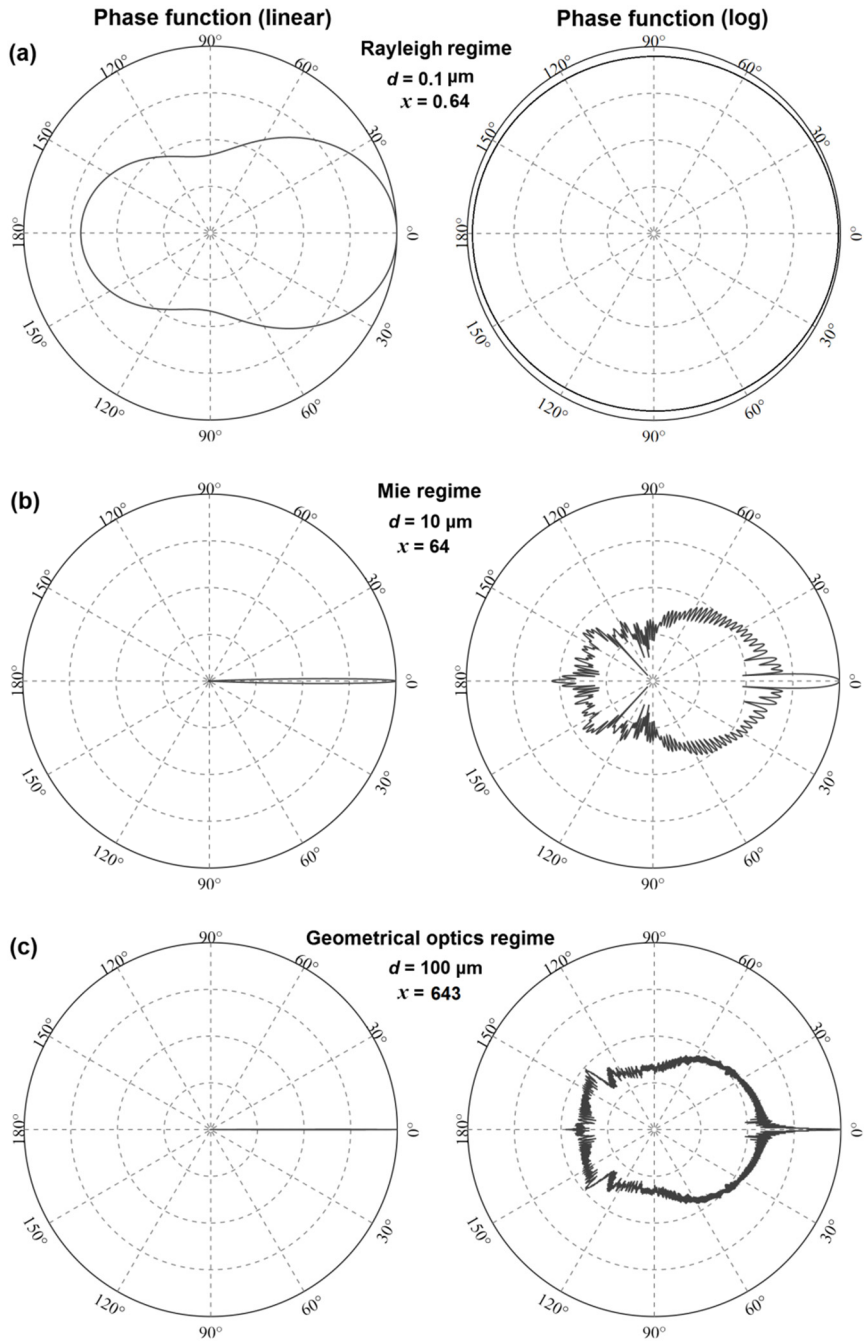

Fig. 10: Linear and log scale plots of scattering phase function calculated from the Lorenz-Mie theory. (a) the Rayleigh regime, (b) the Mie regime, (c) the Geometrical optics regime.

of the droplet and the surrounding medium of different refractive indices according to Snell–Descartes law [75]. A schematic of the different modes of rays resulting from the interaction of light with a spherical particle is given in Fig. 11(b). Every time a ray of light hits a surface of the droplet, one part of it is reflected and another part is refracted. Rays which are reflected directly from the surface are labeled as P = 0, while those refracted directly in the droplet are termed as 1st order refraction (P = 1). The rays of 2nd order refraction (P = 2) emerge after one internal reflection and it is these rays which give rise to the primary rainbow. The 2nd order (P = 2) and 3rd order refraction (P = 3) originate after two and three internal reflections, respectively. Here the refractive index of the droplet medium $\boldsymbol{n_d}$ is greater than to that of the surrounding medium $\boldsymbol{n_m}$.

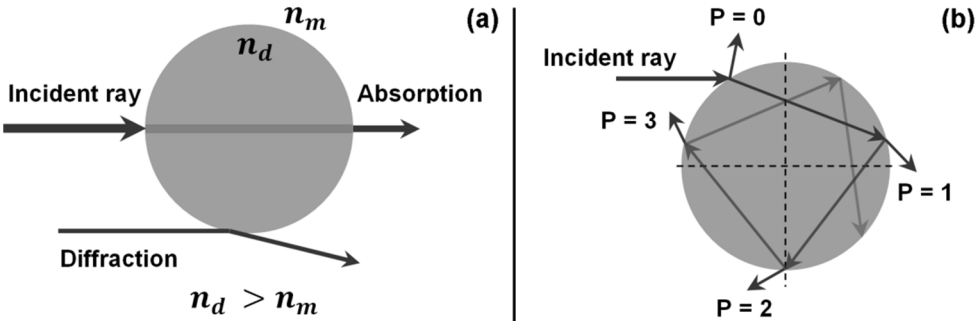

Fig. 11: (a) Geometrical optics sketch of light absorption, and diffraction of light around the curvature of the spherical droplet. (b) Sketch of reflection-refraction light path with the interacting droplet.

3.2 Laser-induced Fluorescence

For the generation of LIF in a droplet, either the droplet is doped with a fluorescence tracer or a self-fluorescent liquid can be used. When a dye-doped droplet is excited with a laser pulse/beam, the incident photons are absorbed by the dye molecule at the ground energy state. Using this energy, the electrons in the dye molecule reaches higher energy state. During the relaxation process from higher to lower energy state through the intermediate energy state, the energy is lost as radiative and non-radiative energy. The radiation part belongs to the spontaneous emission, which is referred as LIF. Because of the loss of the energy during the relaxation process, the LIF emission occurs at a wavelength longer than to that of the excitation wavelength. The non-radiative energy such as pre-dissociation and electronic quenching is collectively referred as quenching in the literature.

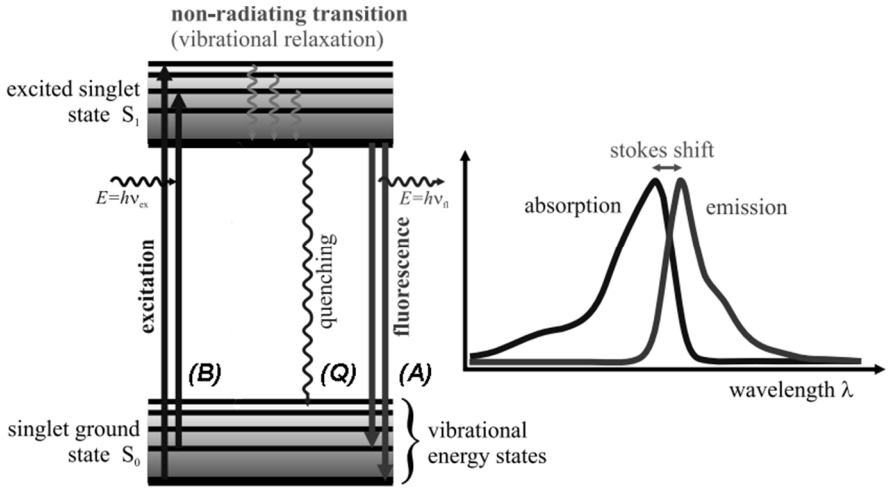

Fig. 12: Jablonski diagram and spectrum illustrating the processes involved in the creation of an excited state by optical absorption and subsequent emission of fluorescence. From reference [79].

Considering a two-level energy transfer processes in LIF according to Jablonski diagram as shown in Fig. 12, the LIF signal intensity can be mathematically described as:

$$\boldsymbol{S_{LIF} = P_{in} \cdot B_{01} \cdot \left(\frac{A_{10}}{A_{10} + Q}\right) \cdot N} \qquad (\mathbf{11})$$

$$\boldsymbol{S_{LIF} = K \cdot N} \qquad (\mathbf{12})$$

$$\boldsymbol{K = P_{in} \cdot B_{01} \cdot \left(\frac{A_{10}}{A_{10} + Q}\right)} \qquad (\mathbf{13})$$

$\boldsymbol{S_{LIF}}$: The emitted LIF optical signal
$\boldsymbol{N}$: The number density of dye molecules per fluid volume
$\boldsymbol{P_{in}}$: The laser power of the incident wavelength
$\boldsymbol{B_{01}}$: Einstein's coefficient of the rate of absorption
$\boldsymbol{A_{10}}$: Einstein's coefficient for spontaneous emission
$\boldsymbol{Q}$: Quenching
$\boldsymbol{K}$: Constant related experimental parameters such as laser power, and dye concentration, *etc.*

In an ideal case, the experimental parameter $\boldsymbol{K}$ remains constant, then, as indicated in Eq. 12, the liquid LIF optical signal is proportional to the number density of dye molecules per unit volume.

Considering a spherical water droplet of diameter $\boldsymbol{d}$ is doped with a fluorescent dye of concentration $\boldsymbol{C}$, covers a volume $\boldsymbol{V}$ with negligible evaporation, the fluorescence signal from Eq. 12 can be derived as:

$$\boldsymbol{S_{LIF} = K \cdot C \cdot V = K \cdot C \cdot \left(\frac{\pi}{6} \cdot d^3\right)} \qquad (14)$$

Thus, from this equation, it is seen that the LIF emission from the droplet is proportional to its volume.

The dependance of liquid fluorescence on droplet volume $\boldsymbol{d^3}$ and Mie scattered light on droplet surface $\boldsymbol{d^2}$ has been exploited for droplet sizing [80]. However, those volumetric and surface relations with the droplet diameter are not strictly respected as discussed in chapeter 4.2.

3.3 Extinction of light

When light passes through a homogeneous scattering medium consisting of an ensemble of droplets, it experiences extinction resulting to an exponential reduction of the light intensity as a function of distance. Figure 13 shows a light beam of incident intensity $\boldsymbol{I_i}$ crossing a distance $\boldsymbol{L}$ within the medium of extinction-coefficient $\boldsymbol{\mu_e}$. According to the Beer-Lambert law [17], the intensity of transmitted light $\boldsymbol{I_t}$ can be expressed as:

$$\boldsymbol{I_t = I_i \cdot exp(-\mu_e \cdot L)} \qquad (15)$$

The extinction-coefficient defines how strongly the medium of a given droplet number density $\boldsymbol{N}$, absorbs and scatters the light crossing it at a given wavelength. The $\boldsymbol{\mu_e}$ can be expressed in terms of extinction cross-section $\boldsymbol{\sigma_e}$, and $\boldsymbol{N}$ as:

$$\boldsymbol{\mu_e = \sigma_e \cdot N} \qquad (16)$$

The cross-section $\boldsymbol{\sigma_e}$ gives the effective area of droplet/light interaction and is directly related to the droplets size and wavelength. The $\boldsymbol{\sigma_e}$ is equal to the sum of the scattering cross-section $\boldsymbol{\sigma_s}$ and the absorption cross-section $\boldsymbol{\sigma_a}$.
In the case of liquid droplets illuminated by a light source in the visible spectrum, the absorption effects are small or negligible unless they are doped with a fluorescence tracer at high concentration. The extinction effects are then mainly due to light scattering. On the contrary, scattering is negligible for droplet's probed with the high-intensity X-rays, where the incident wavelength in the range of a few nanometers. In this case, light absorption becomes the primary contributor to the extinction effects.

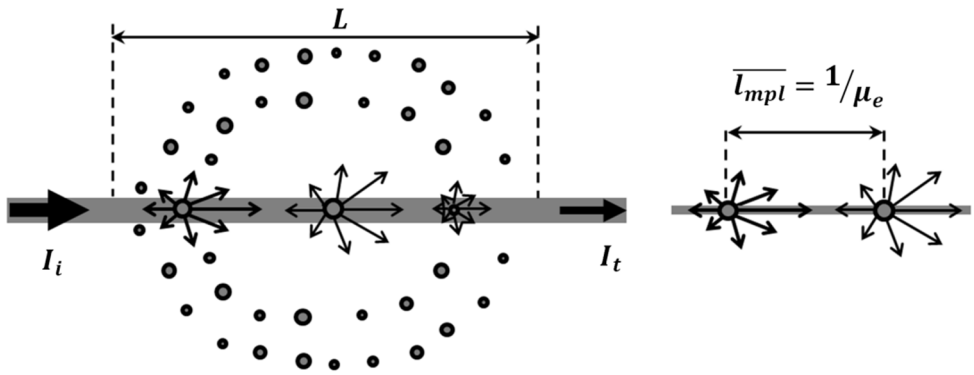

Fig. 13: Illustration of light extinction, and photon mean free path length.

When probing a system containing multiple droplets, the optical depth (OD) gives an approximation of the average number of scattering events occurring [16]. It is also referred in the literature as the optical thickness [81] or optical distance [82], and is expressed as:

$$\boldsymbol{OD = -ln\left(\frac{I_t}{I_i}\right)} \quad (17)$$

The photon mean path length, $\overline{\boldsymbol{l_{mpl}}}$ can be expressed as a function of $\boldsymbol{OD}$, such as:

$$\boldsymbol{OD = \frac{1}{\overline{l_{mpl}}} \cdot L} \quad (18)$$

The photon mean path length is the inverse of $\boldsymbol{\mu_e}$ and gives the average distance between two photons/droplet interactions. Therefore, from Eq. 18, it is seen that the OD is the ratio of the total distance $\boldsymbol{L}$ travelled by the light within the medium to the photon mean path length. Berrocal [17] and Linne [6] have reported that depending on the value of the OD and/or of the average scattering order, the scattering of light within a spray can be classified into three regimes: single scattering (OD ≤ 1), intermediate scattering (2 ≤ OD ≤ 9), and multiple scattering (OD ≥ 10) as illustrated in Fig. 14. Sprays within the single scattering regime are termed as *optically dilute* sprays, while the ones represented by intermediate and multiple scattering regime are termed as *optically dense* sprays. Most spray systems are *optically dense* for the optical diagnostics employed for their characterization. Therefore, the single scattering assumption does not hold true and impose challenges to optical diagnostics where effects such as laser extinction, signal attenuation, and multiple light scattering must be corrected for.

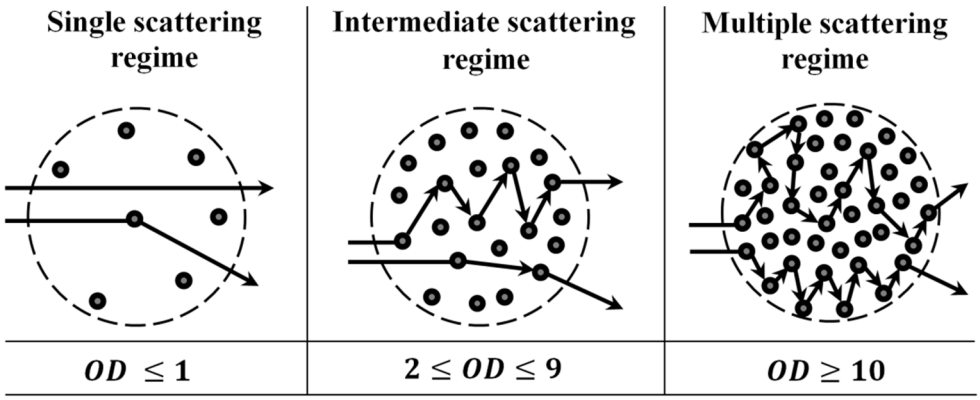

Fig. 14: Illustration of single and multiple scattering regimes estimated from the optical depth of the sample.

3.4 Multiple light scattering

Due to the detection of multiply scattered photons, effects such as the appearance of blur and the reduction of resolution occur on the recorded images. These effects start dictating when the OD of the probed medium becomes greater than 1. Jermy and coworkers [83, 84] reported a Monte-Carlo simulation to evaluate multiple light scattering on images of spray systems. Berrocal *et al.* [85] developed the Monte-Carlo simulation for the estimation of multiple scattering in poly-disperse and highly in-homogeneous media and compared the numerical results with experiments with hollow-cone sprays. It was found that even for sprays considered optically dilute, 76% of the detected photons were multiply scattered. Similar works were further extended for the estimation of singly and multiply scattered photons in turbid media for both forward scattering and side-scattering detection arrangement [86, 87]. From these studies, three possible reasons for detection of multiple light scattering were highlighted:

- The average deviation of the trajectory of the detected photons per scatter.
- OD of the medium.
- Detector geometry and detection acceptance angle.

Figure 15(a) shows an illustration of photons trajectories crossing a scattering medium. Here, in the forward scattering (also known as transmission) detection geometry, photons can be collected as the *Ballistic photons*, *singly scattered photons,* and *multiply scattered photons*. The *Ballistic photons* cross the medium without interacting with droplet and reach the imaging lens without deflected.

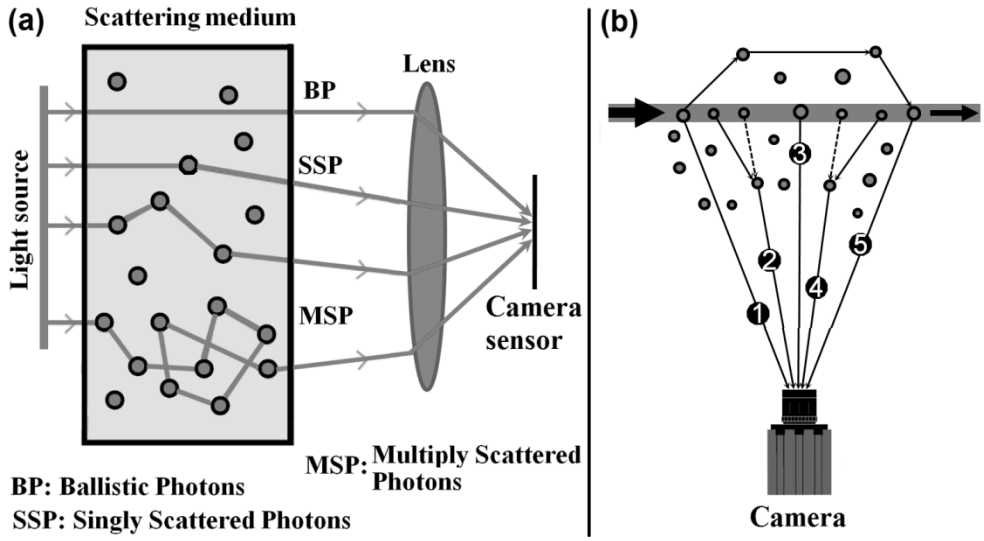

Fig. 15: (a) Illustration of possible detection of singly and multiply scattered photons emerging from a scattering medium for the forward scattering detection configuration. (b) Possible detection of singly and multiply scattered photons emerging from a scattering medium for the side-scattering detection.

The singly scattered photons cross the medium after interacting with droplet only once. The remaining trajectories represent the *multiply scattered photons* which deviate strongly from their initial incident path. In case of the laser sheet imaging corresponding to side-scattering detection, the photon trajectory is shown in Fig. 15(b). Here, different possible photon trajectories for both *singly scattered* and *multiply scattered photons* are shown:

- **Singly scattered photons:** Trajectories **1** and **3** are recorded on the camera after only one light-droplet interaction and thus, preserve information such as sample structures. In this case, a reliable characterization of the probed sample is possible.

- **Multiply scattered photons:** Trajectories **2**, **4,** and **5** are recorded on the camera after interaction of droplet multiple times and thus lose the useful information required for accurate droplet characterization. These three trajectories can be described as follows:

- Trajectory **2** starts as *singly scattered* from the laser sheet, however, on its way to the camera it interacts with another droplet and is slightly deflected from its original path and consequently, the angle of detection to the camera also

changes for it. As a result, the photon following this trajectory is misinterpreted as if it has arrived from the dashed position.

- Trajectory **4** starts as *singly scattered* from the laser sheet, and it would have gone out of the camera detection angle. However, due to interaction with another droplet on its way, its previous trajectory changes and it is interpreted by the detector to have coming from the dashed line.

- Trajectory **5** starts as *multiply scattered* photons from the laser sheet, and this photon induces scattering on another droplet. The subsequent photon path is interpreted as originating from the correct position. Thus, the light intensity reaching the camera sensor is the contribution of intensity both from multiply and singly scattered photon. Nevertheless, this is a most unlikely scenario.

In some situations, when a fluorescing dye is mixed with the liquid, light is not only scattered by the droplets but also fluoresce. Figure 16 illustrates several possibilities as follows:

- The incident light beam can emerge out of the medium as single Mie scattering① and a multiple Mie scattering② signals.

- The incident light can generate LIF in the dye doped droplet and the detected photons can generate primary LIF emission③. This primary LIF emission can then be multiply scattered④.

- The incident wavelength can induce secondary fluorescence in the droplet resulting in secondary LIF emission⑤. This secondary emission can then be multiply scattered⑥. Note that the secondary fluorescence occurs only if the absorption and emission bands of dye overlap. The secondary emission increases with an increase in dye concentration, and increase in path length of light crossing the medium.

- Generation of secondary LIF emission from primary LIF being multiply scattered⑦, secondary LIF emission from multiple Mie scattering⑧.

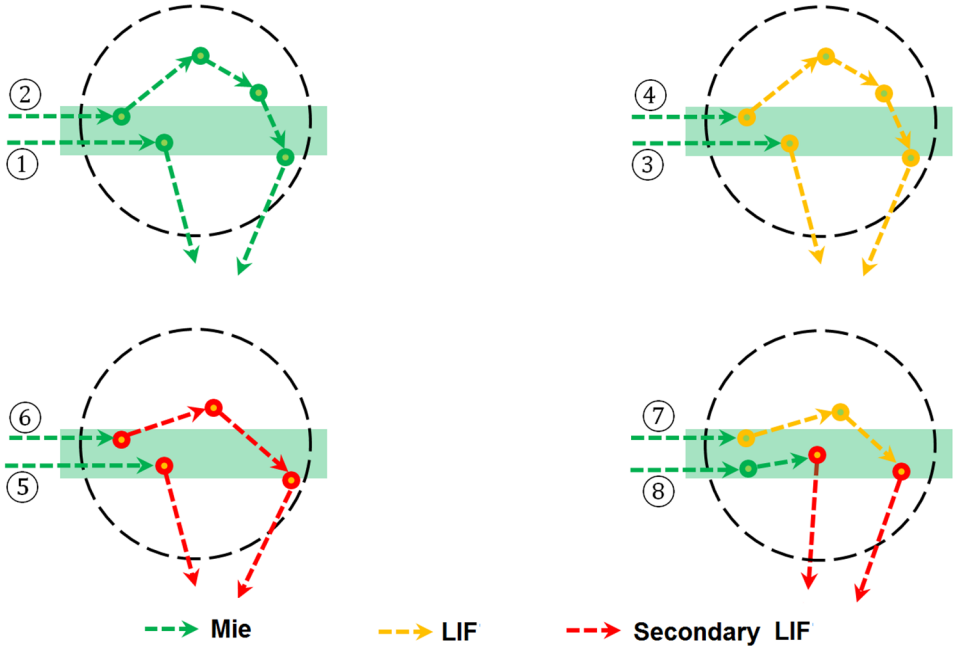

① Single Mie scattering

② Multiple Mie scattering

③ Single primary LIF emission

④ Primary LIF being multiply scattered

⑤ Single secondary LIF emission

⑥ Secondary LIF being multiply scattered

⑦ Secondary emission from primary LIF being scattered

⑧ Secondary LIF emission from multiple Mie scattering

Fig. 16: Several possibilities of photons emerging as singly and multiply scattered from a fluorescing and scattering medium.

4. Planar laser imaging techniques based on intensity ratio

This chapter introduces the laser sheet imaging techniques for spray characterization. Intensity ratio techniques based on planar laser imaging such as LIF/Mie ratio droplet sizing and two-color LIF ratio thermometry are reviewed.

4.1 Planar laser imaging in sprays

Planar laser imaging is a 2D optical sectioning imaging technique [88, 89]. As shown in Fig. 17, the laser beam is converted to a laser sheet and the common approach involves using a beam expander followed by a cylindrical lens to focus the beam along one direction of the projected axis. The 2D images are acquired by a camera fixed at 90 degrees when the spray droplets pass through the laser sheet.

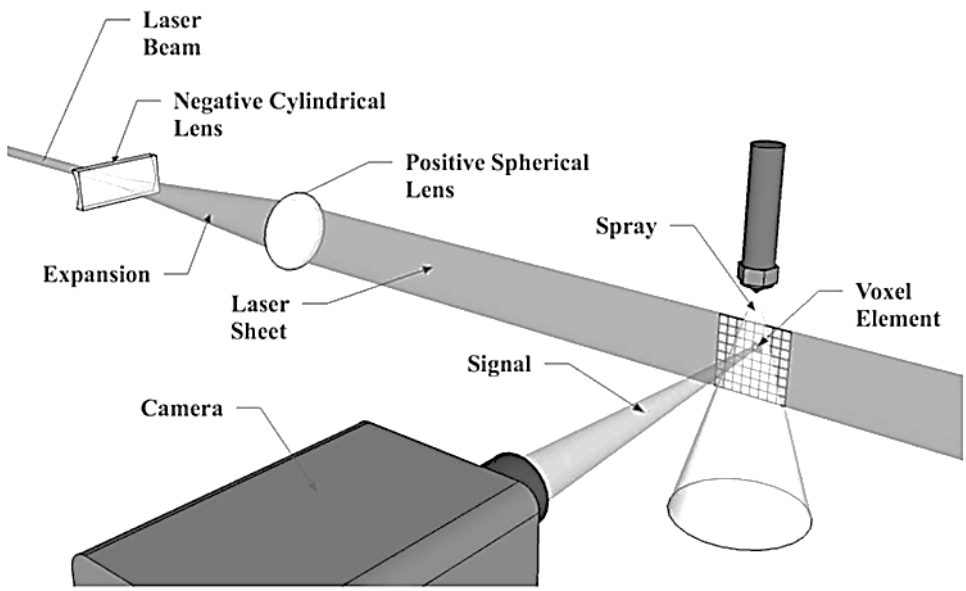

Fig. 17: Illustration of planar laser imaging in sprays. From reference [16].

The recorded images demonstrate the liquid distribution in form of the droplets in an instant in time. The sectioned region could be imaged preferably with both spatial and temporal resolution [5, 88, 89]. For example, many single-shot images can be collected to examine the transient development of a spray, or an ensemble average can be generated from multiple single-shot images to demonstrate the average spray distribution. However, the method often requires calibration in order to convert the qualitative measurements to absolute quantities of sprays, i.e. droplet size [23], spray temperature [54], *etc.* Thus, the precision and accuracy of the measured quantity also depend on the calibration procedure.

Over the past three decades, laser sheet imaging has been used for flow visualization and optical diagnostics in sprays (see table 1, chapter 1). One of the first investigations of a spray using laser sheet imaging was performed by Melton and Verdieck in 1985 [90]. This study was performed in an evaporating fuel hollow-cone spray, by means of Planar Laser Induced Exciplex Fluorescence to image the fuel distributed as a vapor phase and liquid phase within the spray. The planar analysis of diesel sprays in terms of Mie scattering was reported for the first time in 1989 by Cavaliere *et al.* [91].

Table 5. Laser sheet imaging based intensity ratio techniques for sprays

Spray quantities	Intensity ratio-based techniques
Droplet SMD	LIF/Mie intensity ratio [21-23], Raman/Mie intensity ratio [24], Polarization intensity ratio [92, 93], Exciplex-LIF/Mie intensity ratio [25]
Spray and droplet temperatures	Two-color LIF intensity ratio [26-28], Two-color LIP intensity ratio [29, 30], Exciplex LIF intensity ratio [31, 32]

Table 5 lists laser sheet imaging techniques based on intensity ratio for measuring spray quantities. Planar intensity ratio techniques such as LIF/Mie ratio [21, 22], Exciplex-LIF/Mie ratio [25], Polarization ratio [92, 93], and Raman/Mie ratio [24] have been demonstrated for droplet sizing in sprays. The LIF/Mie ratio is used to determine droplet SMD (D_{32}), where the LIF is assumed to be volumetric dependent to droplet diameter, while the Mie is considered surface area dependent to droplet diameter. Exciplex fluorescence has been exploited in Exciplex-LIF/Mie ratio to calculate droplet SMD in flash evaporating sprays. In the LIF/Mie ratio technique, doped fuel and the used fluorescence tracers should ideally have the same evaporation rate, to avoid or minimize enrichment and depletion of fluorescence tracers for evaporating sprays. One of the main challenges of

Exciplex-LIF/Mie ratio is the requirement of an oxygen-free surrounding environment.

To circumvent the use of fluorescent tracers, two alternative schemes have been reported; one based on the ratio of Raman scattering and Mie scattering giving droplet D_{32} [24]. The second method based on the ratio of the vertical and horizontal components of the scattered light intensity known as Polarization Ratio (PR) have been reported for measuring surface mean diameter (D_{21}) of the droplets [93]. The Raman/Mie ratio technique is a good alternative to the fluorescence-based method; however, its applicability is limited due to weak Raman signal leading to low SNR. In the case of PR, the method is limited by errors induced by the strong oscillations from the Mie scattered light intensity. Recently, a femtosecond PR approach was suggested to minimize these intensity oscillations [92]. The use of 220 femtosecond pulses reduces the standard deviation of these oscillations from 30% to 9%, improving the precision of PR for sizing droplets between 25 μm and 200 μm. Nevertheless, shorter light pulses are required for accurately sizing droplets smaller than 25 μm.

Another intensity ratio technique in combination with laser sheet imaging, known as two-color LIF thermometry has been demonstrated for temperature measurements in sprays [5]. In two-color LIF ratio thermometry, one or more dyes are judiciously selected. In two dye approach, one dye is usually temperature sensitive, and the other dye is insensitive. In the single dye approach, the doped dye acts as a temperature sensor and two spectral bands of the emitted LIF signal is used. The two-color ratio approach with a single dye is usually preferred as it eliminates issues related to changes in dye concentration, laser intensity fluctuations, light extinction, *etc.* [94]. Other intensity ratios based planar imaging for thermometry are phosphorescence emission ratio [29, 30] and exciplex two-color LIF ratio [32]. These two approaches are reviewed in detail in references [5, 95].

4.2 LIF/Mie ratio droplet sizing

The LIF/Mie ratio droplet sizing is an intensity ratio method, which is based on the calculation of the ratio of LIF/Mie optical signals measured simultaneously from the same probe location. The method assumes that the liquid LIF optical signal $\boldsymbol{S_{LIF}}$ from the dye-doped droplet is proportional to its volume $\boldsymbol{d^3}$ and the Mie optical signal $\boldsymbol{S_{Mie}}$ from the same droplet is proportional to its surface area $\boldsymbol{d^2}$. The resulting ratio $\boldsymbol{R_{LIF/Mie}}$ is then proportional to the Sauter mean diameter $\boldsymbol{SMD}$ of spherical droplets. SMD of a droplet is the diameter of the entire droplet in spray having the same ratio of volume to surface area.

Considering the LIF and Mie optical signals from the single spherical dye-doped droplet, for each pixel of a camera, the intensity ratio is given as:

$$\boldsymbol{R_{LIF/Mie} = \frac{S_{LIF}}{S_{Mie}} = \frac{K_{LIF} \cdot d^3}{K_{Mie} \cdot d^2} = K \cdot \frac{d^3}{d^2}} \quad (\mathbf{19})$$

Where, $\boldsymbol{K_{LIF}}$ and $\boldsymbol{K_{Mie}}$ are coefficients related to dye concentration, laser power, signal collection angle, detector response, and scattering efficienc, *etc.* Here $\boldsymbol{K}$ equals to the ratio, $\boldsymbol{K_{LIF}/K_{Mie}}$. For an ensemble number of droplets, the intensity ratio is defined as:

$$\boldsymbol{R_{LIF/Mie} = K \cdot \frac{\sum_{i=0}^{n} N_i \cdot d_i^3}{\sum_{i=0}^{n} N_i \cdot d_i^2}} \quad (\mathbf{20})$$

$$\boldsymbol{R_{LIF/Mie} = K \cdot SMD} \quad (\mathbf{21})$$

Where, $\boldsymbol{K}$ is the calibration curve, and it is usually deduced by using the calibration of LIF/Mie ratio with the absolute SMD measured by Phase Doppler Interferometry system [23] or calibrating the ratio by means of monodisperse droplets generated by a droplet generator [22]. The proportionality relation between the intensity-ratio with droplet SMD in Eq. 21 holds valid in following cases:

- Only if the probed droplets are spherical.
- Molecular absorption within the droplets is accounted for.
- The volumetric and square dependence of droplet diameter on the liquid LIF and Mie optical signals, respectively, must be respected.
- The dye concentration and laser power remain constant throughout the experiment.
- The liquid LIF optical signal is proportional to the laser power.
- The liquid LIF optical signal is not saturated during the experiments.
- The liquid LIF optical signal is not sensitive to the temperature change.
- The evaporation rate of the tracer and the doped liquid medium matches well.
- The multiple light scattering effects must be addressed.
- Any effects of morphology dependent resonance must be addressed.
- The Mie scattering signal oscillations are minimized.

The LIF/Mie ratio droplet sizing has been used in several sprays since it was reported by Yeh *et al.* [21] for the first time in 1993, for example in diesel fuel sprays in a rapid compression machine, in Delavan pressure swirl atomizers [22, 96], in dense cooling spray [97], in gasoline fuel injectors [98], and a fuel-injector suited for gun-type burner [23]. In all these investigations, different research group have reported it as Optical patternator [96], Planar Droplet Sizing (PDS) [97, 99] or Laser Sheet Drop-sizing (LSD) [22]. Here, it is referred as LIF/Mie ratio droplet sizing.

LIF and Mie signal dependence on droplet diameter

In the LIF/Mie ratio droplet sizing, droplet diameter, d^3 and d^2 dependency for respective LIF and Mie optical signals have been investigated over the years. Le Gal *et al.* [22] have found that the basic hypothesis is respected at low dye concentration 0.023 g/l for droplet diameter in the range of 50–180 μm produced in a mono-disperse stream using a droplet generator system. However, increasing dye concentration led to diameter exponent or index (*n*) variation between two to three and droplet lasing could change the exponent even higher than three. The tracer p-Terphenyl (PTP) was mixed with the mineral spirit in this study.

Domann *et al.* [80] have investigated the influences of scattering angles: 60°, 80°, 90°, and 120°, refractive index: water (1.333), and fuel (1.4), droplet sizes: 1-1000μm, and Rhodamine 6G dye of concentrations: 0.001-0.1 g/L. The monodisperse water droplet of size ranging from 170-270 μm were produced from a droplet generator for experimental validation. The LIF and Mie signals from the droplet were recorded with a photomultiplier tube. Considering only the influence of dye concentrations and droplet size range of water droplet at 90° detection, Mie signal shows a good agreement with d^2 relation. However, in case of LIF, at low dye concentration, the d^3 relation was respected, but it dropped down to exponent value of 2 with an eight times increase in dye concentration. One of the main reasons for the deviation was the extinction of light crossing the droplet diameter path between the 1st order refraction to 3rd order refraction (1st and 2nd internal reflections) for high dye concentration or large droplet diameters.

Another numerical study by Frackowiak *et al.* [100] have found a similar trend that for the low absorbing mixture d^3 is respected, while for highly absorbing mixtures d^2 relation is more fitting. In this study, the LIF tracer is 3-pentanone and is mixed in n-heptane. Figure 18 shows the evaluation of the diameter exponent of LIF against the imaginary part of the refractive index (n_i) for diameters ranging from 10-130 μm. It is seen that for a constant value of n_i of 10^{-3}, the diameter exponent for diameter range 10-70 μm is 2.4, while for larger diameter range 10-130 μm it is 2. Therefore, the reduction in exponent is much prominent for larger droplet size.

Charalampous *et al.* [77] have numerically investigated the d^3 and d^2 dependance as a function of collection angle 60°-120°, dye concentration, and real part of the refractive index. It was concluded that for LIF: d^3 is respected for the lowest dye concentration 0.001g/L, and real refractive index variation has a very little effect. For Mie scattering signal: d^2 depends strongly on the real refractive index, scattering angle, and dye concentration. The relation is best respected for lowest dye concentration, and scattering detection at 60° instead of 90°, for all the droplet refractive indices. At 60° detection angle, the Mie scattering fluctuations are minimized.

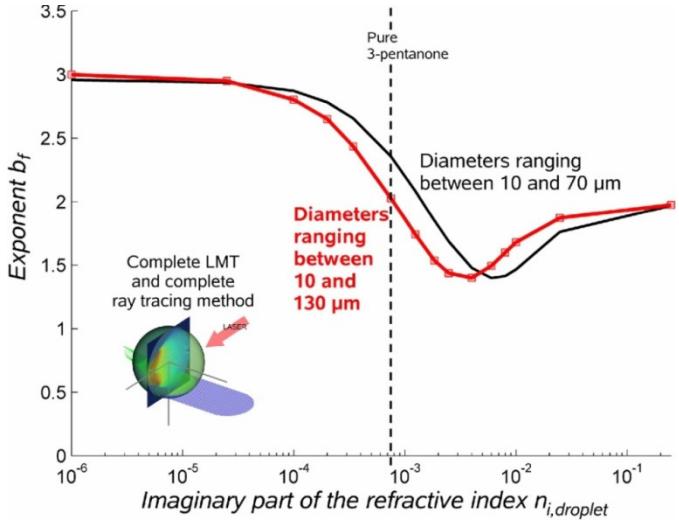

Fig. 18: Evolution of the diameter exponent of LIF against the imaginary part of the refractive index (n_i) for different diameter ranges. Plots are from reference [100].

Effects of tracer volatility in evaporating sprays

The LIF/Mie ratio gives a good estimate of absolute SMD values in non-evaporating sprays. In case of evaporating sprays, the tracer concentration varies locally and temporally and moreover, the fluorescence signal contribution from the gas phase cannot be neglected. The dependency of LIF signal on fuel temperature can also be an issue in evaporating sprays. Düwel *et al.* [73] have investigated the effects of tracer and fuel evaporation in LIF/Mie droplet sizing. Three LIF tracers: acetone, toluene, and coumarin 47 with different volatilities were investigated in ethanol as fuel. The summary of the investigation is as follows:

- **If the LIF tracer is more volatile than the fuel or if the tracer evaporates faster than the fuel.** For example, acetone (boiling point 56°C) starts evaporating faster than ethanol (boiling point 78°C), then the generated liquid LIF signal is lower due to low dye concentration. However, the Mie signal from the fuel remains unaffected. As a result, the overall LIF/Mie ratio reduces as the droplets evaporate and thus the calculated SMD value is lower than the actual SMD value.

- **If the LIF tracer is less volatile than the fuel**. For example, tracers, toluene and coumarin 47 have boiling points much higher than ethanol. The tracer concentration increases during evaporation (increasing the overall LIF signal), while the Mie signal from the fuel reduces. As a result, the LIF/Mie ratio is overestimated and the calculated SMD is larger than the actual SMD.

Erroneous SMD measurements can be made by LIF/Mie ratio approach due to enrichment or depletion of fluorescence tracers for evaporating conditions. Therefore, a careful choice of tracers with similar boiling points as the solvent or fuel is strongly recommended.

Effects of multiple light scattering

In most of the "conventional" LIF/Mie ratio measurements, the multiple scattering effects are not considered. However, in optically dense sprays, multiple light scattering effects cannot be ignored. If the multiple scattering $\boldsymbol{MS_{LIF}}$ effects are considered, then the intensity ratio, $\boldsymbol{R_{LIF/Mie}}$ in Eq. 21 becomes:

$$\boldsymbol{R_{LIF/Mie} = \frac{S_{LIF} + MS_{LIF}}{S_{Mie} + MS_{Mie}} \neq SMD} \qquad (22)$$

Where, $\boldsymbol{MS_{LIF}}$ and $\boldsymbol{MS_{Mie}}$ are the multiple light scattering contributions to the singly scattered LIF and Mie optical signals, respectively.

One of the first studies that reported on the effects of multiple scattering (MS) on LIF/Mie ratio was performed by Stepowski *et al.* [101]. They reported the effects of MS on LIF and Mie optical signals using Monte Carlo simulations. The MS from LIF is different to the MS from Mie, and this effect does not cancel out after the ratio as considered in most of the "conventional" LIF/Mie ratio works. The experimental demonstration of MS effects on LIF/Mie ratio has been reported in Berrocal *et al.* [42] by combining the sizing approach with SLIPI technique. It was found that the undesired MS intensity must be first suppressed on both the LIF and Mie signals for reliable mapping of the relative SMD. Another work from the same group by Kristensson *et al.* [48] have evaluated the effects of MS on fluorescence and Mie scattering media and supported the suppression of MS prior to SMD mapping. Subsequent work by the group on LIF/Mie ratio in combination with SLIPI has found that for SMD mapping in sprays, the MS effects must be suppressed. It was shown that the MS contribution impedes the quantitative SMD mapping that too in an optically dilute spray of OD = 1 [50]. The study is a part of this thesis work and reported in detail in chapter 5.2.

4.3 Two-color LIF ratio thermometry

Laser sheet-based two-color LIF thermometry is a very attractive technique for extracting a 2D map of temperature with high spatial and temporal resolution.

Using two-color LIF ratio method 2D images of temperatures in liquids, droplets and sprays have been reported in the past [5-13]. The method is divided into two sub-categories:

Two-dye approach

The initially reported work on LIF thermometry was performed by Coppeta *et al.* [26] and Sakakibara *et al.* [27], using two-dye approach. In both these studies, two fluorescent dyes were chosen because of their fluorescence emissions falling in different spectral bands. Ideally, the spectral separation should be perfect between the emissions bands selected for LIF thermometry, where no fraction of the fluorescence emission by one band $\boldsymbol{S_{LIF1}}$ is leaking into the second band $\boldsymbol{S_{LIF2}}$, and vice-versa. If this condition is respected, the intensity ratio, $\boldsymbol{R}$ of the detected fluorescence intensities as a function of droplet temperature $\boldsymbol{T}$ can be expressed as:

$$\boldsymbol{R(T) = \frac{S_{LIF1}}{S_{LIF2}} = \frac{K_{LIF1} \cdot C_1 \cdot I_{in} \cdot \varepsilon_1 \cdot \emptyset_1}{K_{LIF2} \cdot C_2 \cdot I_{in} \cdot \varepsilon_2 \cdot \emptyset_2} = K \cdot \frac{f(T)_1}{f(T)_2}} \qquad (23)$$

$$\boldsymbol{R(T) = K \cdot f(T)} \qquad (24)$$

for:

$$\boldsymbol{C_1 = C_2,} \qquad \boldsymbol{f(T)_1 = \varepsilon_1 \cdot \emptyset_1,} \qquad \boldsymbol{f(T)_2 = \varepsilon_2 \cdot \emptyset_2}$$

$\boldsymbol{C_1}$ and $\boldsymbol{C_2}$ **:** Concentrations of the two dyes.
$\boldsymbol{I_{in}}$ **:** Local incident laser intensity.
$\boldsymbol{\varepsilon}$ **:** Absorption coefficient of dye.
$\emptyset$ **:** Fluorescence quantum yield of dye.
$\boldsymbol{K}$ **:** Calibration constant related to experimental setup.
$\boldsymbol{f(T)}$**:** Overall temperature response function related to absorption coefficients and fluorescence quantum yields of two dyes.

For an accurate estimation of the liquid temperature with this approach, the following conditions must be considered:

- The used dyes should produce fluorescence emissions with one having temperature sensitive and other with almost negligible temperature sensitivity.
- The dye concentration ratio should be kept constant and uniform in the flow.
- The spectral interference due to the overlap between absorption and emission bands should be avoided to eliminate the re-absorption and re-emission of the fluorescence.
- The incident laser intensity fluctuations should be corrected.

The technique has been employed for LIF thermometry in liquid solutions stored in transparent test cells [26, 27], microchannel [102], and on droplets produced from droplet generators [103, 104]. In a recent study from Chaze *et al.* [104], the

approach is demonstrated using Fluorescein dye (FL) as temperature sensitive tracer, while Sulfo-Rhodamine 640 (SR640) as temperature insensitive tracer. In Fig. 19(a), the two detection bands selected from the LIF emissions of two dyes for the application of two-color LIF thermometry can be seen. The evolution of Fluorescence intensity ratio is plotted as a function of temperature in Fig. 19(b). The dyed solution consists of mixtures with concentrations $C_{SR640} = 0.7 \cdot 10^{-6}$ M and $C_{FL} = 2 \cdot 10^{-4}$ M.

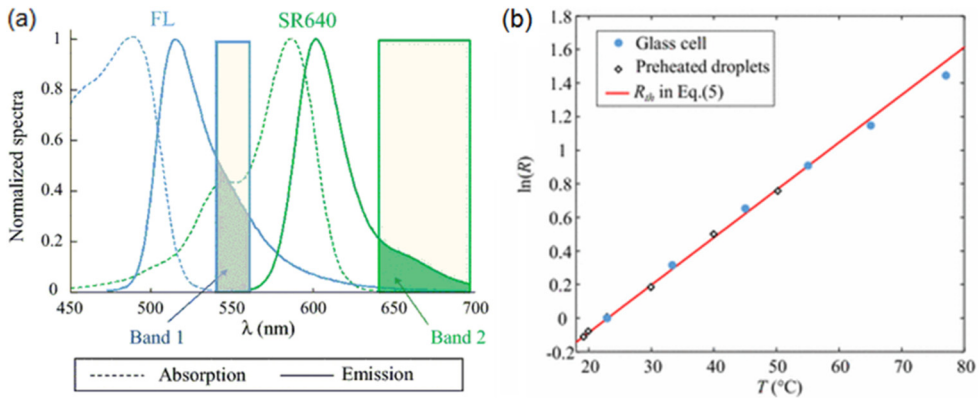

Fig. 19: (a) Two detection bands selected for the application of two-dyes approach using dyes FL/SR640. (b) Evolution of the fluorescence intensity ratio R as a function of the temperature at concentration $C_{FL} = 2 \cdot 10^{-4}$ M and of $C_{SR640} = 0.7 \cdot 10^{-6}$ M. Plots are from reference [104].

Single dye approach

The second approach, with single dye, is preferred over the first approach because it eliminates the issue of changes in dye concentration, laser intensity fluctuations, *etc.* [28]. In this, two spectral bands from a single temperature sensitive fluorescence emission are selected. One spectral band represents a temperature insensitive or relatively less sensitive band, while the selected second band is highly temperature sensitive or vice-versa. The intensity ratio of either of these two bands can be used as temperature sensor. Lemoine *et al.* pioneered this method for thermometry in droplets steam and sprays [28, 94, 105]. For example, Perrin *et al.* [106] have reported the approach using pyrromethene 597-C8 dye as temperature sensitive tracer, which is doped with different liquid fuels (ethanol, isohexane, n-heptane, n-decane, n-dodecane) and their mixtures for thermometry. The seeded liquid is excited with 532 nm pulsed illumination of a frequency-doubled Nd-YAG laser. Figure 20(a) shows the temperature sensitive broadband emission spectrum of pyrromethene 597-C8 dissolved into n-dodecane at temperatures ranging from 20°C to 99°C. Here, LIF1 (Band1) is in the range 540-560 nm, and the LIF2 (Band2) is ranging from 610 nm to 630 nm. The sensitivity

factor $\Delta\beta$ is plotted in Fig. 20(a). A marked distinction in temperature sensitivity can be observed in the green-yellow region and the orange-red region of the LIF emission spectrum. Figure 20(b) presents the calibration curves of two-color LIF ratio against temperature, obtained for different fuels including ethanol, isohexane, n-heptane, n-decane, and n-dodecane. It can be observed that the sensitivity to temperature of the fluorescence ratio is fuel solvent dependent even for the same group of chemical compounds such as alkanes. Temperature sensitivity is lower in n-heptane (about 0.7 %/°C at 25°C) and higher in ethanol (about 1 %/°C at 25°C). These differences can be interpreted as the intermolecular deactivations of the excited states mainly by collisional quenching. These temperature-dependent processes are by nature function of the quencher type and hence the liquid solvent containing the dye molecules.

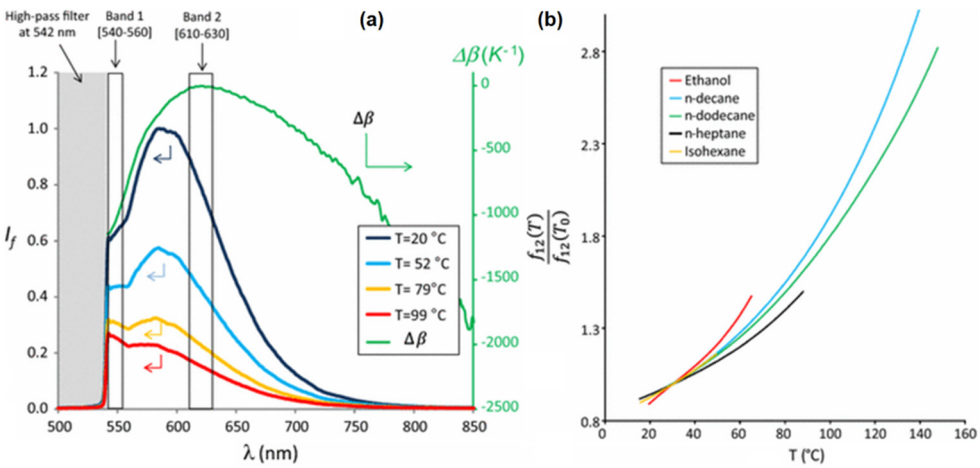

Fig. 20: (a) Emission spectra of pyrromethene 597-C8 recorded at different temperatures. In green, the temperature sensitivity ($\Delta\beta$) with λ_0 = 630 nm. (b) The evolution of LIF intensity ratio showing the effect of temperature on the signal ratio R_{12} (T_0 = 25 °C) for different fuels. Plots are from reference [106].

Effects of Morphology Dependent Resonances

According to Perrin *et al.* [106], the coupling of the fluorescence emission of the dye and morphology dependent resonances (MDR) also termed whispering gallery modes, could impose difficulties in LIF thermometry. As shown in Fig. 21(a), the basic interpretation of MDR's is that of rays that travel around the spherical particle return to their starting position in phase and after one or several turns around the drop. The ray of an MDR approaches the internal surface of the particle beyond the critical angle and so is almost totally reflected. Hence, the energy of an

MDR remains confined in the particle and high densities of energy can accumulate. The travel of such light rays is favored only for specific wavelengths, for a given droplet diameter and liquid refractive index. In fluorescent dyes, lasing can occur within the dye-doped microparticle with high amplification modes that coincide with an emission band of the dye as shown in Fig. 21(b). The emission spectra recorded here is for 100 μm size decane droplets seeded by pyrromethene 597-C8 at different concentrations from 10^{-7}mol/L to $5{\cdot}10^{-5}$ mol/L. Each spectrum is LIF signal contribution of thousands of droplets. A peak due to lasing inside the droplets is clearly visible near 620 nm at the highest concentrations of fluorescent dye. To suppress the MDR effects, it is suggested to use a non-fluorescent dye, the Oil Blue N, in the liquid fuel, which covers the spectral absorption region of pyrromethene 597-C8 dye to stop the light amplification. A concentration of as low as 10^{-6} mol/L of Oil Blue N has found to be sufficient to suppress the MDR effects.

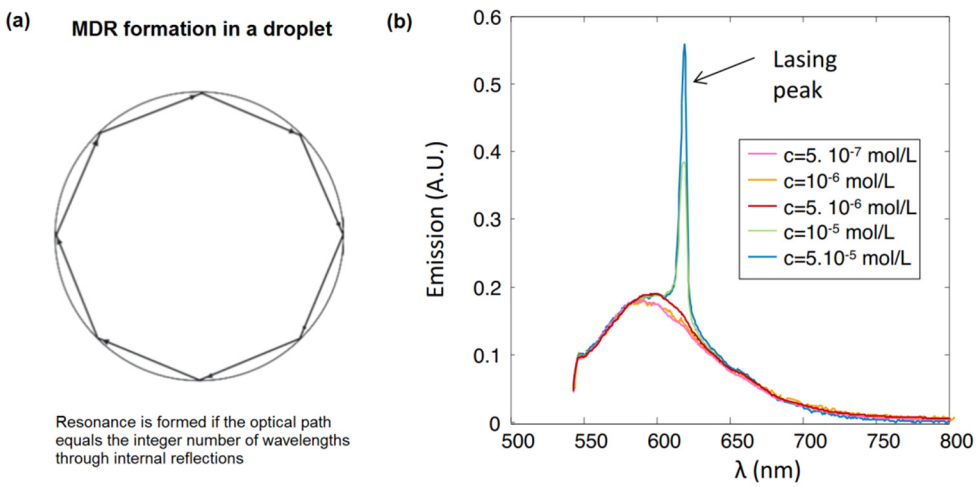

Fig. 21: (a) Illustration of MDR formation in a droplet. (b) The emission of a lasing peak inside the droplet at 620 nm wavelength. Plots are from reference [106].

Effects of Self-absorption

The self-absorption effects occur due to the overlap of absorption and fluorescence emission as shown in Fig. 22. When the laser light passes through the fluorescing medium, the part of the emitted signal is re-absorbed, and lead to the generation of re-emission of secondary fluorescence at longer wavelengths. This re-absorption and re-emission process depends on the quantum efficiency of the dye and is collectively called self-absorption process. In LIF thermometry, the self-absorption has a strong effect on the determination of temperature. The self-

absorption is significant if the path length of the light crossing the medium is larger or the tracer concentration increases. To minimize the effects of self-absorption it is advised to use low dye concentration, however, that comes at the cost of reduction of signal intensity. Another possibility is to minimize the path length for the light crossing the fluorescing medium. Lavieille *et al.* [28] have evaluated the self-absorption effect and corrected the influence of optical path by introducing a third spectral band.

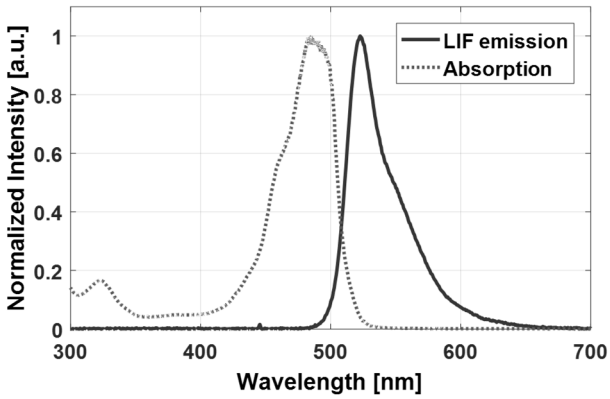

Fig. 22: Generation of self-absorption effect due to partial overlapping between the absorption and LIF emission spectra of fluorescein as a temperature sensitive tracer.

5. Temporally averaged SLIPI-based characterization in steady sprays

In this chapter SLIPI-based intensity ratio techniques for droplet sizing, droplet concentration, and spray thermometry are described. These temporally averaged SLIPI-based techniques are demonstrated for the characterization of steady sprays. Results from papers I, II and VI are summarized here.

5.1 Temporally averaged SLIPI

The concept of SLIPI technique [45, 46] has stemmed from structured illumination microscopy [107]. In SLIPI, the illuminating light sheet is modulated in space, either with a sinusoidal- or square intensity pattern, rather than a homogeneous illumination. The purpose of this "line-pattern" is to experimentally differentiate between light that has been directly- and multiply scattered and to computationally remove the latter. This is achieved by shifting the "line-pattern" one-third of the spatial period and record a set of three modulated images (sub-images). From this data set, a final demodulated SLIPI image (see Fig. 25) can be extracted, wherein the contribution from the multiply scattered light has been reduced [45]. However, due to the need for recording three sub-images, SLIPI has been mostly used for temporally averaged measurements in sprays. Note that SLIPI has also been demonstrated for 'instantaneous' imaging of rapidly occurring events [49]. In this case, the three sub-images were recorded with an optical arrangement consisting of three Nd:YAG lasers in combination with a multi-frame ICCD camera. With this setup, the three sub-images could be acquired within a sub-microsecond time scale, short enough to temporally freeze the flow and thereby avoid droplets displacements occurring in the time interval between the data acquisitions. Although, despite the ability to obtain 'instantaneous' images in the near-field spray region with no image blur, the hardware cost and complexity of such SLIPI setup clearly limit its applicability in practice. As an alternative to instantaneous 3p-SLIPI technique, recently 2p-SLIPI and one-phase 1p-SLIPI techniques are developed. Their optical setup, image post-processing, and application for instantaneous evaluation of transient sprays are given in chapter 6.

Spatial modulation of light intensity

The essence of the SLIPI technique relies on the spatial modulation of light intensity for generation of the structured light sheet, and one of most used scheme to achieve this in this thesis work is exploiting the interference of diffraction orders projected from the Ronchi grating. This scheme was employed in Papers I-III and VI. This approach is based on illuminating a square grating, consisting of rulings which provided alternating opaque and transmission stripes. In this method, the opaque stripes reflect the incident light, thereby increasing the laser damage threshold, unlike the image generation of sinus pattern (see papers IV, V, VII), which absorbs the light. One of the advantages of this scheme is that the modulation depth of the projected pattern remains nearly constant with distance. In addition, the imaged field will mostly contain a single spatial frequency, which reduces the risk for eventual residuals as artifacts in the final SLIPI image. When the square wave pattern of Ronchi grating is illuminated with the incident light source, it is dispersed and split into several orders of diffraction. Each diffraction order has a certain magnitude and direction which, depends on the mask. The dispersion angle $\boldsymbol{\theta_n}$ of each diffraction order $\boldsymbol{n}$ depends on the spatial frequency $\boldsymbol{\nu}$ of the Ronchi grating and the wavelength $\boldsymbol{\lambda}$ according to:

$$\boldsymbol{\theta_n = sin^{-1}(n \cdot \nu \cdot \lambda)} \qquad (25)$$

From several of these diffraction orders as shown in Fig. 23, only two diffraction orders ±1, are selected, while blocking the order 0, to let only allowed orders interfere further. In this case, it is accomplished by focusing the transmitted light onto a frequency cutter device positioned at the Fourier plane. The device consisted of two blades, and a thin thread in-between the two, which block higher orders of diffraction. The two blades block the diffraction orders above ±1, while the thin thread blocks the order 0. With distance, the allowed orders overlap and interfere, thus creating the desired sinusoidal intensity pattern. One of the drawbacks of the fringe projection approach is the substantial loss of incident laser energy (in some cases up to 90%) due to the required rejection of the 0th and higher spatial frequency orders.

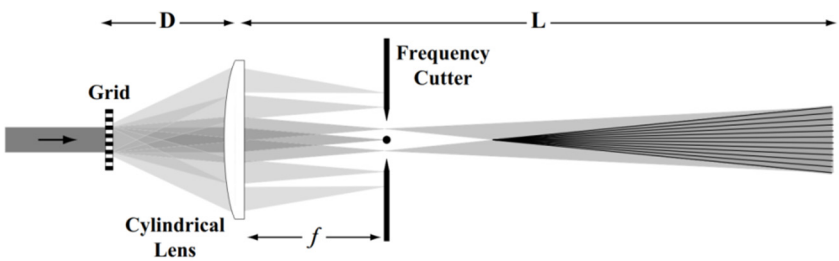

Fig. 23: Generation of the structured beam in fringe projection approach by letting the 1st order diffraction interference. Image from reference[16].

5.2 SLIPI-LIF/Mie ratio droplet sizing

In this section, LIF/Mie ratio is applied in combination with SLIPI for 2D mapping of droplet SMD in a steady state (continuously running) hollow-cone water spray. The LIF/Mie ratio is calibrated with the SMD data measured with a PDA system.

Description of the experimental setup

The SLIPI-LIF/Mie experimental setup is given in Fig. 24. A pressure swirl nozzle of 1 mm orifice diameter (Lechler, ordering no. 216.324) is used to create the spray of 60° spray angle. It is investigated at room temperature and atmospheric pressure conditions. The injection pressure is fixed at 20 bar producing a liquid flow rate

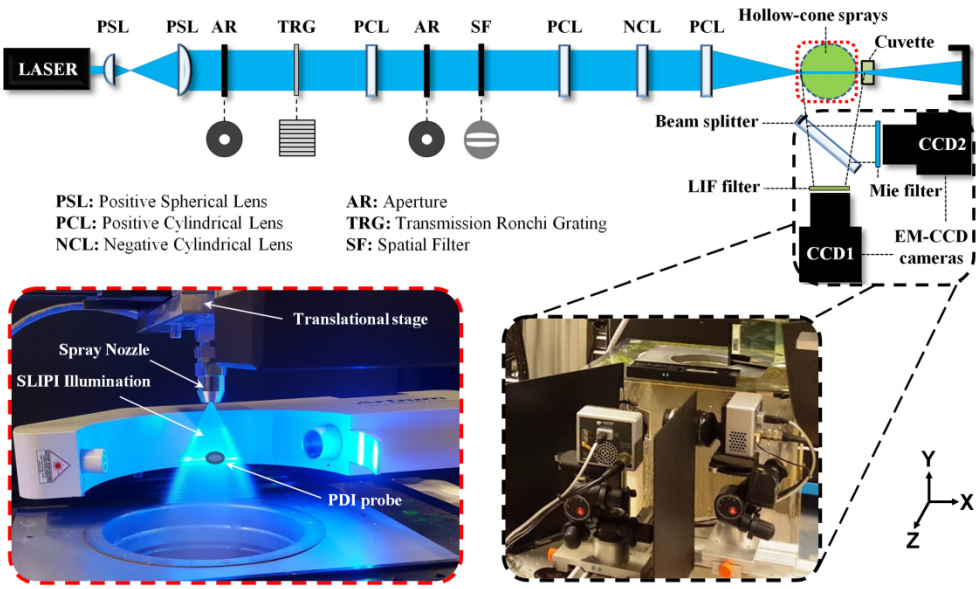

Fig. 24: Experimental setup for SLIPI-LIF/Mie planar droplet sizing and SLIPI-scan extinction coefficient mapping. A hollow-cone water spray is illuminated with the SLIPI-modulated light sheet. Two identical EM-CCD cameras are used to simultaneously record the spectrally separated LIF and Mie optical signals. A PDA system is used to calibrate the LIF/Mie ratio with the absolute SMD of droplet measured by it.

of 1.26 liter/min. The injected water is doped with a translucent fluorescing dye (Pyranine: Solvent green 7) from yellow highlighter's ink. The main reasons for choosing the yellow highlighter's ink as tracers are the non-toxicity and the high quantum efficiency of the dye when excited at $\lambda = 448$ nm. The center of the spray

is illuminated (using a collimated CW diode laser) with a vertically modulated laser sheet. The broad-band LIF signal, which is peaking at 517 nm, and the 448 nm narrow-band Mie signal are spectrally separated using a long pass filter (GG495 Yellow Schott Optical Filters) together with two high-performance optical filters (95% in transmission and optical density > 6 in blocking). The long-pass filter is characterized by a cut-on wavelength at 495 nm and reflects most of the 448 nm incident light. The band-pass filter used for the detection of the fluorescence signal is centered at 510 nm with 94 nm FWHM (full width at half maximum). For the Mie signal, a narrow-band filter centered at 448 nm with 20 nm FWHM is used. The LIF and Mie signals are simultaneously recorded using two identical cameras positioned orthogonal to each other and at 90 from the illuminated plane. These cameras are 14-bit electron multiplying CCD cameras (Luca R from Andor), providing images of 1004×1002 pixels. A pixel-to-pixel overlapping of the images is important before processing the intensity ratio. To achieve this, the positioning and the focusing of the cameras must be carefully adjusted and the recorded images must be warped to reach a nearly equal field of view. Here, the two separated optical signals are recorded with an exposure time of 0.88 seconds and 75 images are accumulated. The laser power of the modulated light sheet is reduced down to 5% of the 900 mW initial output power mostly due to light losses induced by the transmission Ronchi grating and the spatial filter. To calibrate the SLIPI-LIF/Mie ratio, a PDA system (PDI-200 MD) from Artium Technologies is used. The detailed description of the PDA optical setup is given in reference [50]. The PDA probe volume is overlapping with the modulated laser sheet in order to calibrate the LIF/Mie images. The spray is moved along the direction of the laser sheet (from the edge of the spray towards its center) to acquire distribution histograms of the droplet size for every millimeter. For each collection point, 50000 validated size measurements are recorded and the corresponding absolute SMD is calculated. It is observed in all measurements that the diameter validation percentage was above 96%, demonstrating good sphericity of the droplets at distance 3.5 cm below the nozzle tip.

LIF and Mie images

Three modulated sub-images of the LIF and the Mie signals are shown in Fig. 25(a). The modulated light sheet is entering the spray from the left and traverses it along its central axis. A spatial phase difference of 120° between the set of two successive images are achieved by physically shifting the grating along the vertical direction. This is operated by means of a high-precision piezo actuator from Physik Instrumente. Based on these three modulated sub-images, the final "conventional" and SLIPI images, shown in Fig. 25(b), are extracted using Eq. 3 and Eq. 2, respectively. The image differences between the two detection schemes can be seen. In comparison to the "conventional" image, the SLIPI image is

"cleaned up" from undesired effects such as blurring and detection of light intensities from non-illuminated areas.

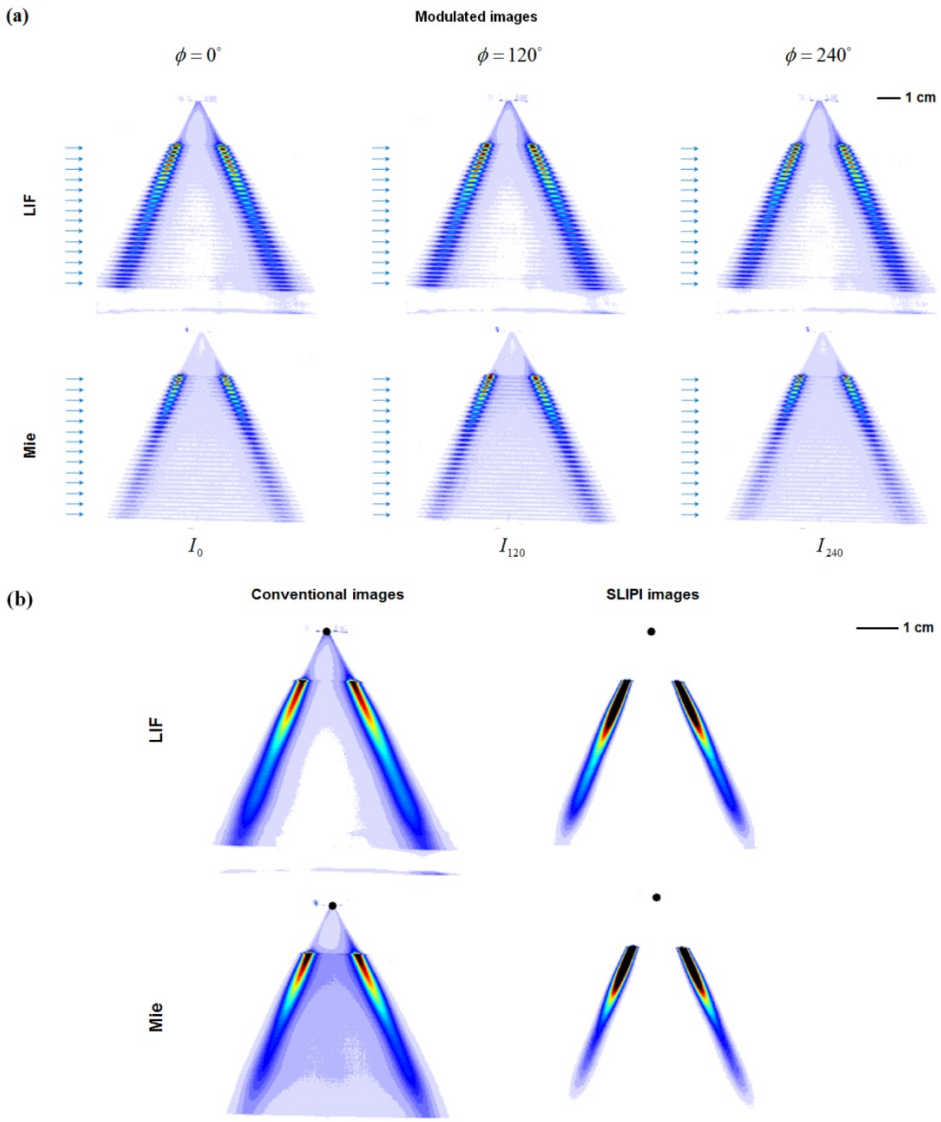

Fig. 25: The "conventional" and SLIPI, LIF and Mie averaged images of the hollow-cone spray are generated by recording three modulated sub-images of both signals as shown in (a). These modulated images are recorded with a phase difference of 120°. The "conventional" images, created by averaging the three modulated sub-images, and the SLIPI images, generated by taking the root-mean-square of the same images, are shown in (b).

Non-calibrated LIF/Mie ratio images

The images of non-calibrated LIF/Mie ratio or relative SMD of droplets is shown in Fig. 26. These images are extracted from the intensity ratio of the LIF and Mie images given in Fig. 25(b). For a fair comparison between the "conventional" and the SLIPI results, the image post-processed routine is kept the same:

- The image background is first calculated from the average of 100 pixels located at the top left corner of each image.
- After background subtraction, a threshold value equal to 0.001% of the maximum peak intensity of the image is calculated.
- Any pixel value below this threshold is disregarded to avoid numerical errors while ratio in the data.

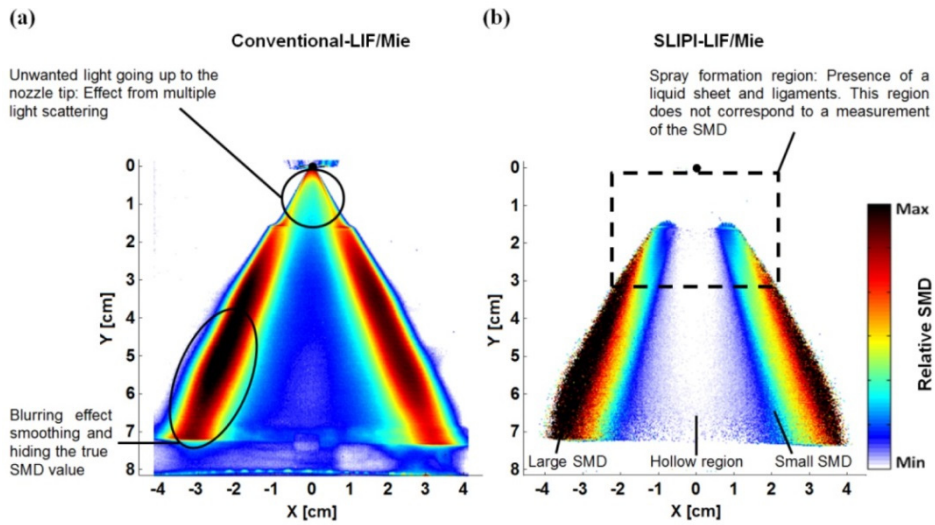

Fig. 26: Averaged images of the "conventional" LIF/Mie and SLIPI LIF/Mie, in (a) and (b) respectively, representing the relative SMD of droplets distribution. Effects from the multiple light scattering can be seen on the "conventional" SMD image.

It is worth mentioning here that a nearly identical SLIPI SMD image can be obtained without background subtraction. Several noticeable differences between the LIF/Mie ratios of "conventional" in Fig. 26(a) and SLIPI in Fig. 26(b) can be pointed out as:

- First, a SMD value is seen up to the nozzle tip on the conventional LIF/Mie image while this is not observable for the SLIPI case. As this part of the spray is not illuminated by the laser sheet, the corresponding SMD is extracted from multiply scattered photons only and has, consequently, no real meaning.

- Second, according to the SLIPI results large droplets are located on the edge of the spray while small droplets are measured at this same location with "conventional" planar imaging.
- Finally, due to blurring effect, the spray cone does not appear as hollow for the "conventional" as it does clearly for the SLIPI image.

This observation needs now to be proven by the means of an additional technique where the absolute SMD can be measured. To achieve this, a PDA setup from Artium Technologies has been used. It should also be noted from Fig. 26(b) that the SMD data cannot be considered near the nozzle exit (indicated on the SLIPI LIF/Mie image by the dashed rectangular area) due the presence of non-spherical droplets and ligaments.

PDA measurements

The absolute SMD of droplet measured by using PDA system is shown in Fig. 27(a). This is performed at a given vertical position (y = 3.5 cm) from the nozzle center (up to x = 0.5 cm). Large droplets, SMD ~ 27 µm, are detected on the spray edge, while small droplets, SMD ~ 5 µm, are in the spray center. This support the trend observed in the previous section for the non-calibrated SLIPI LIF/Mie

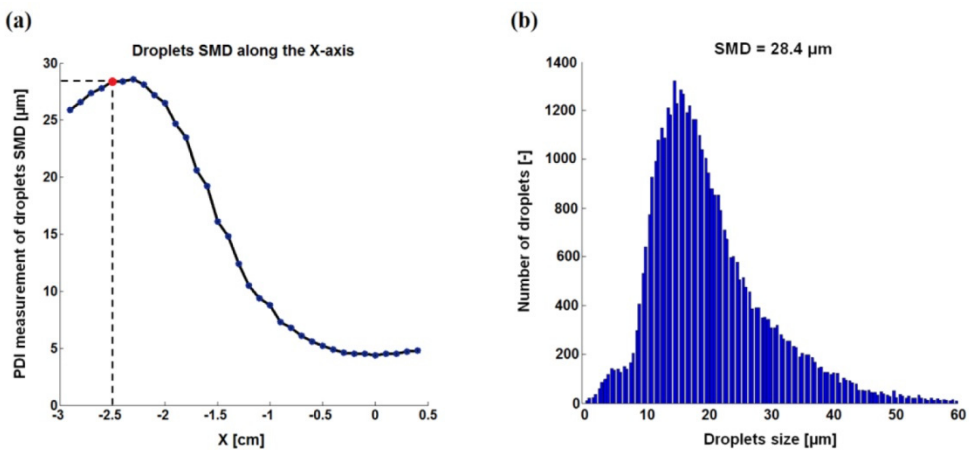

Fig. 27: (a) Droplets SMD along the x-axis from one edge of the spray (set as −3 cm) towards its center (0 cm). An example of such distribution at position x = 2.5 cm in the Fig. 27(a)) is given in (b) where the resulting SMD = 28.4 µm.

results. In addition, it shows that the central part of the spray is not fully hollow and those small droplets are transported in this region due to vortical air flows. The spacing between each PDA data point is kept 1 mm. For each of the point, a

droplet size distribution corresponding to 50000 droplets validated by the PDA system is considered. One example of distribution is given in Fig. 27(b) corresponding to the position x = −2.5 cm (red dot from Fig. 27(a)). In this example, a bimodal distribution can be observed where the resulting SMD equals 28.4 µm.

Calibration of LIF/Mie ratio

The SMD data from PDA measurements in Fig. 27(a) is now used for the calibration of the LIF/Mie intensity ratios. For each PDA measurement point, a value of the LIF/Mie ratio is assigned as shown in Fig. 28. In "conventional" detection, corresponding to Fig. 28(a), it is observed that for the same LIF/Mie ratio, two different SMD values are measured with PDA. For example, 10 µm and 28 µm droplets SMD are found for an identical LIF/Mie ratio equal to ~ 1 at different locations in the spray. This reveals that the LIF/Mie ratio cannot, in this case, be calibrated. It is, however, important to note that the intensity contribution from multiply scattered light is very difficult to predict and the observed trend may change with the collection angle, optical turbidity, droplets size, ditribution of the

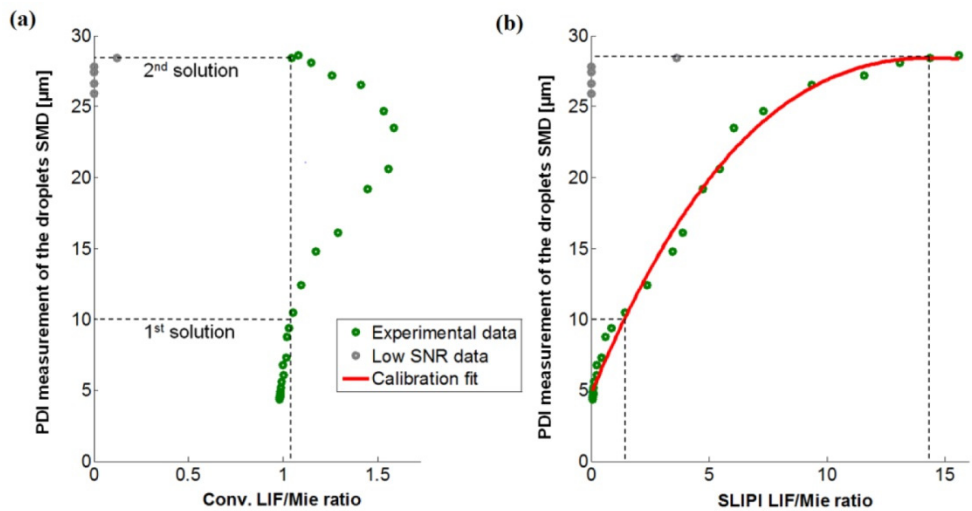

Fig. 28: Plots of the SMD values measured with PDA against the corresponding LIF/Mie ratio. In (a) the "conventional" case shows two SMD solutions for a single LIF/Mie ratio. In this case, the measurement cannot be calibrated. In (b) the SLIPI case shows a unique solution for each LIF/Mie ratio. This confirms the possibility of extracting a reliable calibration curve that can be used to deduce the absolute droplets SMD from Fig. 26(b).

droplets in the spray, *etc.* As the spray investigated here is optically dilute (of OD = 1 in reference [50]), this observation leads to the examining of the accuracy of any SMD measurement when using "conventional" LIF/Mie in sprays. Opposite to

the “conventional” approach, in SLIPI detection corresponding to Fig. 28(b), a single solution of SMD is found for any LIF/Mie ratio. A calibration curve can be deduced allowing the relative SMD data shown in Fig. 26(b) to now be calibrated.

Absolute SMD mapping in 2D

A two-dimensional map of the absolute SMD of the droplets is shown in Fig. 29, after calibration of the SLIPI LIF/Mie results using the red curve from Fig. 28(b). The indicated box corresponds to the spray formation region where non-spherical droplets and ligaments are present. Similarly to the results found with PDA, the presented image shows the presence of 5 µm droplets in the central region of the spray. However, the injected water disintegrates into large droplets of ~ 29 µm along the spray edges which is also in accordance with the PDA measurements.

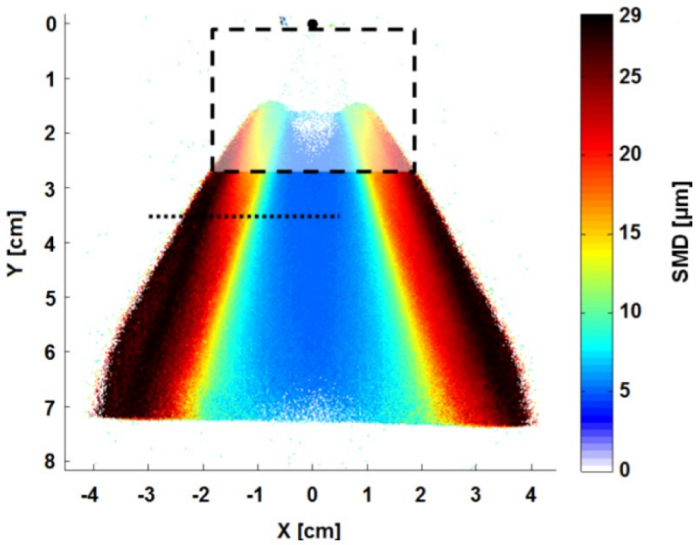

Fig. 29: Two-dimensional map of the absolute droplets SMD for a hollow-cone water spray running at 20 bar injection pressure. The result is obtained from SLIPI LIF/Mie after calibration with PDA data. The PDA measurements were performed at 3.5 cm below the nozzle tip, along with the black dot line the image.

5.3 Combined SLIPI-LIF/Mie and SLIPI-scan

In this section, SLIPI-LIF/Mie ratio approach is applied in combination with a light transmission imaging technique known as the SLIPI-scan for simultaneous mapping of droplet SMD, droplet concentration (N), and Liquid Volume Fraction (LVF). To perform this combined approach, the spray is probed by the structured light sheet in a "bread-slicing" manner. A flow chart showing all extracted spray quantities is shown in Figure 31. A general description of the process is as follows: The calibrated SLIPI-LIF/Mie measurements provide the droplet SMD for each spray layers. Based on this measurement and by taking advantage of the droplet size distribution provided by the PDA measurement, the averaged extinction cross-section σ_e (in mm^2) for each droplet SMD is deduced from the Lorenz-Mie theory. Those calculations were performed using a Mie calculator developed by the authors based on the algorithm proposed by Bohren and Huffman [108]. The local μ_e maps are obtained from SLIPI-scan [41]. By now calculating the ratio μ_e/σ_e the N value (#/mm^3) is deduced. Finally, the LVF can be extracted from the product between the droplet number density values and the droplet volume which is approximated from the droplet SMD. Note that those calculations are made on each pixel of the spray images allowing to map the spray in 3D.

Description of the experimental setup

The experimental setup of combined SLIPI-LIF/Mie and SLIPI-scan technique is shown in Fig. 24. Some of the additional components and modifications for this setup is as follows:

- The spray is injected at 50 bar liquid injection pressure at room temperature and atmospheric pressure conditions.
- The spray nozzle is now staged on a programmable translational stage for moving along the Z-direction.
- Fluorescein dye is used as a LIF tracer.
- A transparent cuvette with dyed liquid is used for light transmission measurements.
- A turn-key PDA (Artrium PDI-TK2 system) is used for calibrating the SLIPI-LIF/Mie ratio with the absolute SMD measured from it.

The simultaneous LIF and Mie sub-images are recorded with an exposure time of 0.08 seconds and 20 accumulations. To perform the SLIPI-scan, the spray is moved along the Z-direction with a step difference of 500 μm.

LIF, Mie and their intensity ratio images

Figure 32 shows SLIPI-LIF images of the spray and transmitted light through the cuvette in (a), Mie images of spray in (b) and the intensity ratio, SLIPI-LIF/Mie of

spray in (c). Out of 31 slices of images recorded with the combined SLIPI approach, only the image at Z = 15 mm is shown here. A detaimed procedure to obtain those spray quantities using the combined SLIPI technique is demonstrated in paper VI.

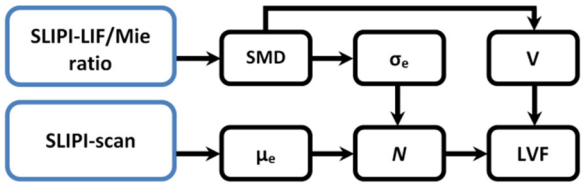

Fig. 31: Simplified flow chart of the image post-processing for extracting the droplet SMD, the droplet number density (N), and the liquid volume fraction (LVF). The process is operated via a scanning approach where the SLIPI-LIF signal, the SLIPI-Mie signal and the light intensity transmitted through the spray are simultaneously recorded.

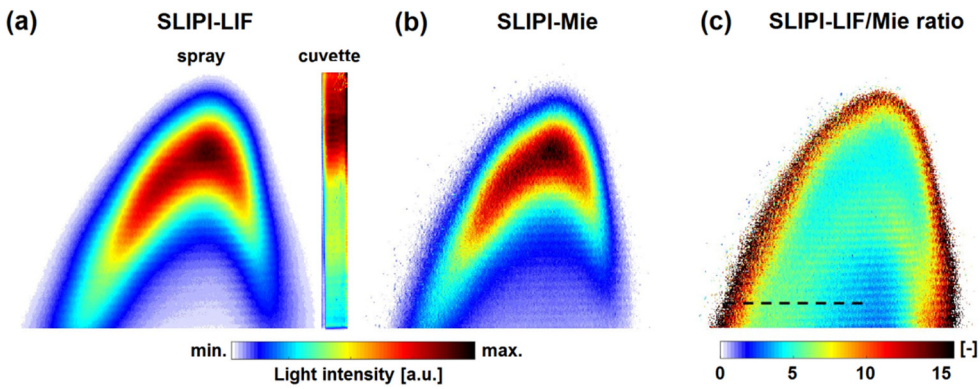

Fig. 32: SLIPI-LIF images of spray and the dye cuvette are given in (a). SLIPI-Mie image of spray in (b). SLIPI-LIF/Mie intensity ratio of spray image is shown in (c).

Droplet SMD, droplet concentration, and LVF

Figure 33 shows the 2D images of spray quantities: droplet SMD, N values, and LVF at positions Z = 4 mm to Z = 15 mm along Z-direction. The 2D results for different spray layers are as follows:

- At Z = 4 mm: droplet SMD ranges between 50 µm to 60 µm, N value ranges from 5 droplets per mm^3 to 20 droplets per mm^3, LVF ranges between 0.35×10^{-3} to 1×10^{-3}.
- At Z = 8 mm: droplet SMD ranges from a minimum value of 35 µm to a maximum value of 60 µm, N value ranges from 5 droplets per mm^3 to 35 droplets per mm^3, LVF ranges between 0.25×10^{-3} to 1×10^{-3}.

- At Z = 15 mm: droplet SMD ranges between 20 µm to 60 µm, *N* value ranges from 5 droplets per mm^3 to 70 droplets per mm^3, LVF ranges between 0.1×10^{-3} to 1×10^{-3}.

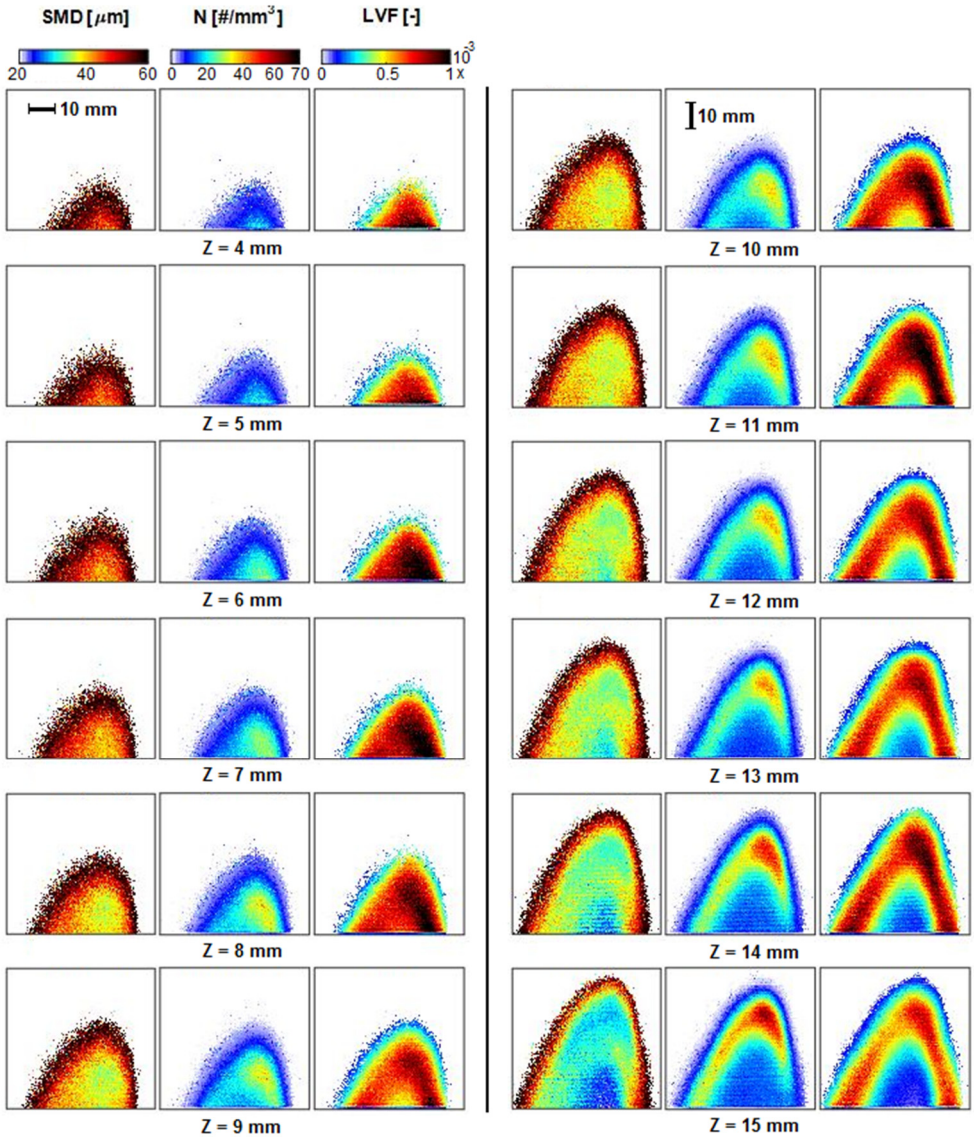

Fig. 33: 2D maps of droplet SMD, N, and LVF at Z = 4 mm to Z = 15 mm along Z-direction. Droplet SMD ranges between 20-60 µm, N varies between 5-70 droplets per mm^3, and LVF vary from a minimum of 0.1×10^{-3} to a maximum value of 1×10^{-3}.

5.4 SLIPI-two color LIF thermometry

In this section, two-color LIF (single dye) approach is introduced in combination with SLIPI for 2D mapping of temperature in aqueous solutions and in hollow-cone water sprays.

Description of the experimental setup

A schematic setup of the combined SLIPI two-color LIF ratio technique is shown in Fig. 34. A spatially modulated laser light sheet (52 mm height,~ 0.5 mm thickness) is created from the SLIPI setup using a 447 nm continuous wave diode laser. This illumination scheme excites the dye solution either stored in a cuvette or droplet in a hollow-cone water spray. The emitted fluorescing signal is detected by two electron multiplying CCD cameras of the same characteristics. Each of these 14-bit cameras (Andor, Luca R) records an image of 1004 × 1002 pixels. To record the two LIF signals simultaneously, a beam splitter (40/60%: transmission/reflection) is used in-between the cameras together with two high-performance bandpass filters, F1 and F2 fixed in front of each objective.

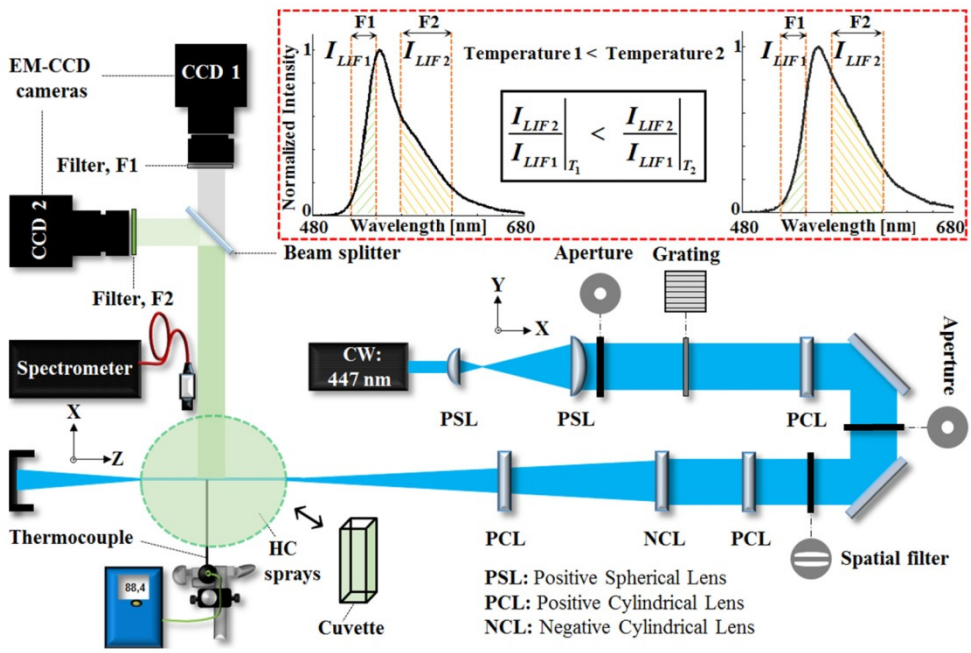

Fig. 34: Experimental setup of SLIPI two-color LIF ratio thermometry including all optical components. The dashed box (red) on the top right is an illustration of two-color LIF ratio thermometry principle.

The overlap of the cameras field-of-view is accurately adjusted by imaging a test target and by using a warping scheme to ensure a perfect pixel to pixel overlapping. For correlating the two-color LIF ratio with liquid temperature, a calibration work is performed by measuring temperature within a defined region on the recorded image. The reference temperature is measured using a thermocouple of 1 mm tip diameter (K type, Pentronic AB). In the cuvette measurements, the thermocouple is fixed and inserted within ~2 mm behind the laser sheet. In the spray case, the thermocouple is inserted into the light sheet directly and for each measured temperature (droplet temperature in this case) the LIF images are recorded after rapid removal of the thermocouple. As the studied spray is steady (continuously running for a given temperature of the injected water), the assumption that the temperature remains constant between the thermocouple measurements and the images recordings is considered as valid.

5.4.1 Measurements in cuvette

For the cuvette measurements, the Fluorescein dye solution is mixed with water and heated up to 90°C. The two-color LIF images are then recorded from 85°C down to 25°C at every five degrees temperature change. The exposure time of the cameras is set to 12 milliseconds for each sub-image so that the final SLIPI image is recorded in a sufficiently short time where the temperature decreases less than 0.1°C for each measurement point. This is required under higher temperature conditions where the water is rapidly cooled. Moreover, in order to have an optimized signal-to-noise ratio (SNR), the smallest f-number of the objectives is chosen, corresponding here to $f_{\#} = 2.8$.

Temperature dependent LIF spectrum

The temperature-dependent LIF spectrum of the solution (dye/water) is investigated at an excitation wavelength of λ = 447 nm and at temperatures ranging from 21°C to 90°C. The spectra are recorded using a spectrometer AvaSpec-USB2 while the temperature is monitored using a K-type thermocouple. The non-normalized spectra, shown in Fig. 35(a), indicate that the maximum fluorescence intensity reached 21°C decreases by 27.3% at 90°C. When normalizing the spectra, Fig. 35(b), a red-shift of the intensity maximum from 523 nm to 530 nm is clearly observed. From the spectral shift in the LIF emission intensity as a function of temperature, two suitable spectral bands are selected. Figure 35(b) shows the spectral range of two selected optical filters (F1, F2), used for two-color LIF ratio. A detailed description regarding the selection of two spectral bands is given in paper II and in reference [109].

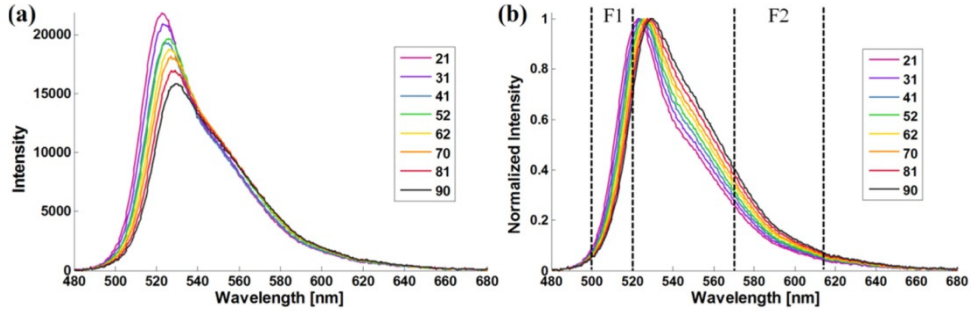

Fig. 35: Non-normalized in (a) and normalized in (b) LIF emission spectra of the Fluorescein dye at 447 nm excitation and for a temperature ranging from 21-90°C: A change in LIF emission intensity and spectral shift are apparent [109]. The spectral range of two selected optical filters (F1, F2), used for the LIF ratio can be seen in (b).

Two-color LIF ratio sensitivity to liquid temperature

The temperature sensitivity between CONV ("conventional") and SLIPI detection, the two-color LIF ratio and its sensitivity are plotted as a function of temperature in Figs. 36(a) and 36(b), respectively. In Fig. 36(a), the plotted curves are obtained by correlating the reference temperature with the averaged two-color LIF ratio over the thermocouple measurement region corresponding to a 100 × 100 pixels area. It is seen that the LIF ratio increases from 1.8 to 8.9 with SLIPI while it only increases from 1.4 to 3 with CONV when the temperature rises from 25°C to 85°C. Therefore, the LIF ratio dynamic range improves by a factor of three with the SLIPI technique in comparison with the "conventional" planar imaging approach. Note that the solid lines are third-order polynomial fittings of the

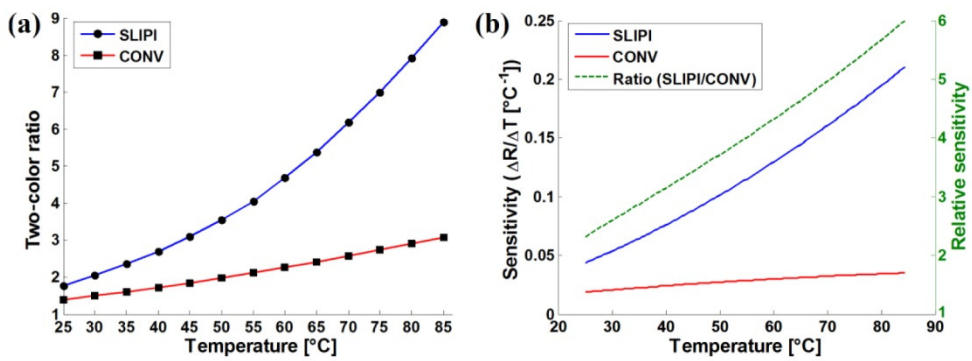

Fig. 36: (a) the two-color LIF ratio (both from CONV and SLIPI) are plotted as a function of liquid temperature. It is found that the SLIPI-LIF ratio improves the dynamics by a factor of three compared to that of CONV-LIF ratio. (b) The sensitivity per degrees (left Y-axis) both for the SLIPI and CONV is shown together with the sensitivity ratio SLIPI/CONV (right Y-axis, in green).

respective markers. In Fig. 36(b), the sensitivity per degree is deduced by taking the derivative of the two-color LIF ratio R with respect to the temperature T. It is seen that SLIPI offers a much higher sensitivity than CONV. From, the relative sensitivity curve, represented by the green dashed line, it is apparent that at 25°C the measurement sensitivity is more than twice as high with SLIPI than with CONV and it increases up to 4 and 6 times higher at 55°C and 85°C, respectively. Those improvements in sensitivity are mostly due to suppression of unwanted background fluorescence with SLIPI.

Absolute temperature of liquid in the cuvette

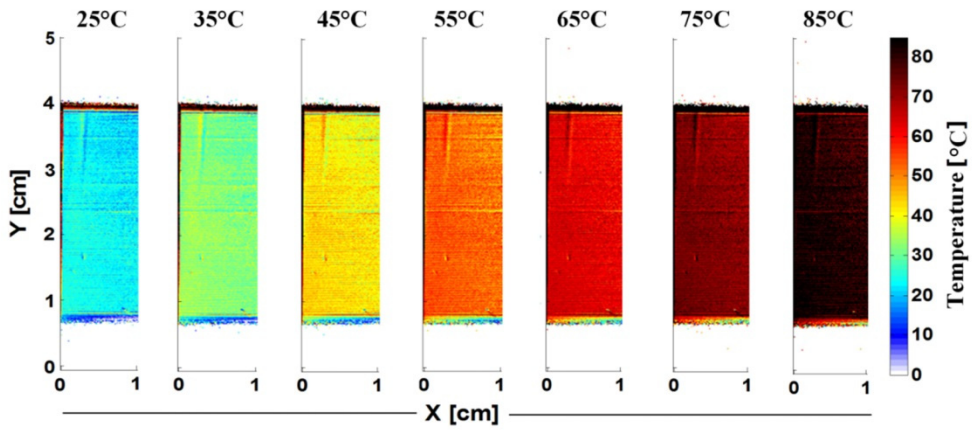

Fig. 37: Calibrated SLIPI-LIF ratio depicting the absolute temperature of the liquid in the cuvette. Results have been deduced using the SLIPI calibration curve given in Fig. 36(a). It is seen that the water temperature is nearly homogenous throughout the cuvette for each reference temperature case ranging between 25°C to 85°C.

The calibrated SLIPI-LIF ratio is shown in Fig. 37. Those images are obtained by using the SLIPI curve from Fig. 36(a) as a calibration curve and generating an image of the absolute temperature of the water in the cuvette. It is apparent from those images that the water temperature is homogeneous throughout the light sheet, for each reference temperature.

5.4.2 Measurements in sprays

For the spray measurements, the laser sheet shown in Fig. 34 is located at 1.5 cm below the nozzle tip. The dyed water is heated in a 50 liters tank before being sprayed by a pressure swirl nozzle (Lechler, no. 216.324) of 1 mm orifice diameter. A steady condition is set at 20 bar injection pressure corresponding to a

liquid flow rate of 1.26 liters/min. The liquid is discharged at room temperature and atmospheric pressure conditions. The two-color LIF images are recorded for droplet temperatures ranging between 25°C to 55°C with a step difference of 5°C.

Absolute temperature of liquid in sprays

The two-dimensional absolute temperature mapping of the spray droplets are given in Figs. 38(a), 38(b), 38(c) and 38(d), respectively recorded at reference temperatures 25°C, 35°C, 45°C and 55°C. In (a) the droplet temperature is overall homogeneous throughout the spray and equals 25°C as expected as the injected water was at room temperature. When the injected liquid is heated-up, gradients of temperature are becoming apparent over the spray, with a cooler region in the spray center. For instance, for the case of the image (d) this gradient ranges from 25°C in the hollow region of the spray to 55°C near the nozzle orifice.

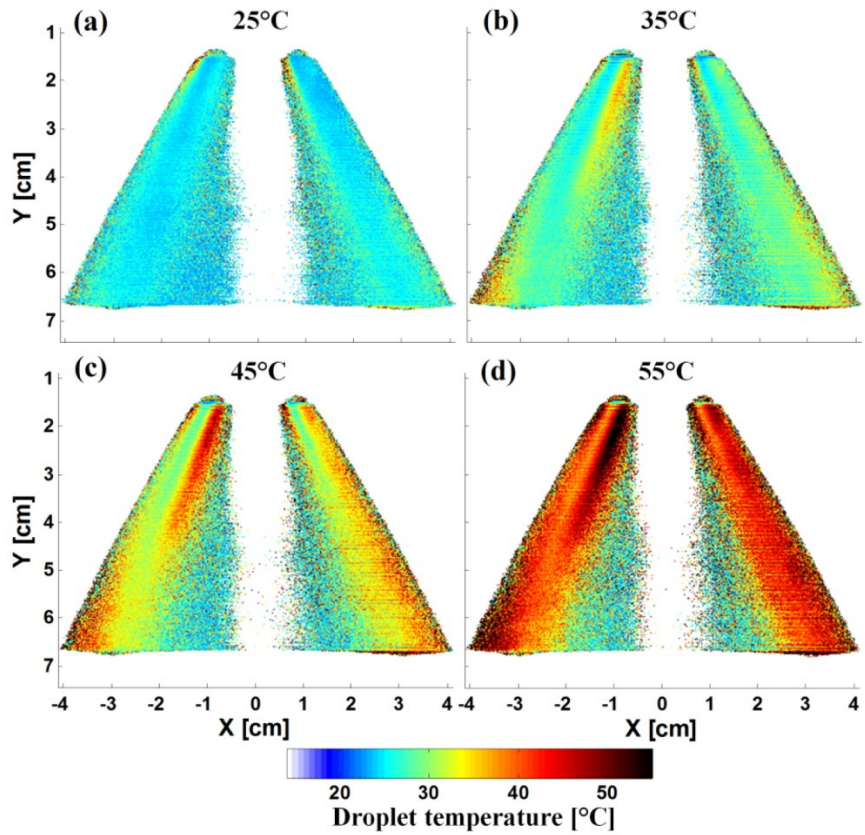

Fig. 38: Two-dimensional map of droplet temperature in a hollow-cone water spray at reference temperature varying between 25°C to 55°C. The spray cools down in its hollow region while the liquid located nearer to the nozzle orifice is hotter.

6. Instantaneous SLIPI based characterization in transient sprays

This chapter provides a brief introduction to 2p-SLIPI and 1p-SLIPI techniques and their applications for the characterization of transient sprays. Results from papers IV, V and VII are summarised here.

6.1 Two-phase SLIPI (2p-SLIPI)

General description

In 2p-SLIPI, the spray is illuminated with two modulated light sheets of the same spatial frequency, but of opposite spatial phases. Thus, a final SLIPI image is constructed from a set of two sub-images, denoted $\boldsymbol{I_0}$ and $\boldsymbol{I_{180}}$, having a phase difference of 180°. An intermediate image is extracted from the absolute value of the intensity difference of the two sub-images, $|\boldsymbol{I_0 - I_{180}}|$. However, this subtraction produces *residuals,* stretching throughout the intermediate image within the regions where the sub-images have equal light intensities. To deduce a residual-free final 2p-SLIPI, an additional Fourier-filtering is required:

$$\boldsymbol{I_{2p-SLIPI} = F_{2v}\left(\sqrt{(I_0 - I_{180})^2}/2\right)} \qquad (\mathbf{26})$$

where $\boldsymbol{F_{2v}}$ denotes the applied Fourier-filtering while $\boldsymbol{I_{2p-SLIPI}}$ is the light intensity corresponding to the resulting SLIPI image. Note that the "gap" of information manifested as residuals is the main reason why 3p-SLIPI is preferred and 2p-SLIPI has been avoided in the past. These residuals appear at a spatial frequency twice that of the incident modulation, and, therefore, can be made indistinguishable by strategically "placing" them at spatial frequencies beyond the resolving capability of the imaging system, as illustrated by [110].

2p-SLIPI optical setup

A schematic of the 2p-SLIPI optical arrangement is shown in Fig. 39, where two 532 nm pulsed Nd:YAG lasers are used. In this case, the time duration of each pulse is approximately 6 nanoseconds and the lasers have a repetition rate of 10 Hz. The fluence of the pulses from each laser is adjusted to be as equal as possible. The time delay in between the two laser pulses is set to ~150 nanoseconds, which corresponds to the shortest time for an sCMOS camera to record two successive frames. To accurately adjust the orientation of the linear polarization a half-wave plate is used at the output of each laser system and the beams are spatially combined using a polarization beam splitter. The two overlapping beams are then expanded using the combination of a negative and a positive spherical lens. An aperture is used to select the central part of the expanded beams in order to homogenize their intensity profiles. The pattern created by the Ronchi grating is imaged along the vertical direction using a first cylindrical lens. A second cylindrical lens is then used to focus the beam into a light sheet that coincides with the location of the image of the grating. One important requirement for 2p-SLIPI is to have a phase difference of the two spatially modulated pulses corresponding to half a period (i.e. 180 degrees phase shift). As mechanical devices are not fast enough to produce such a phase shift within ~150 ns, this has been done in the past by means of two Ronchi gratings positioned in two optical channels [110]. However, recently an alternative method to produce the required phase shift through optical means only was demonstrated, and this study is part of this thesis work in Paper IV. The solution exploits the birefringence properties of calcite crystals as shown in the zoomed area of Fig. 39. The basic principle is that the horizontally and vertically polarized pulses are subjected to ordinary and extraordinary refraction through the crystal, respectively. In the case of an incidence angle of 0° on the crystal, it results in no directional change for the vertically polarized beam while the horizontally polarized beam refracts with an

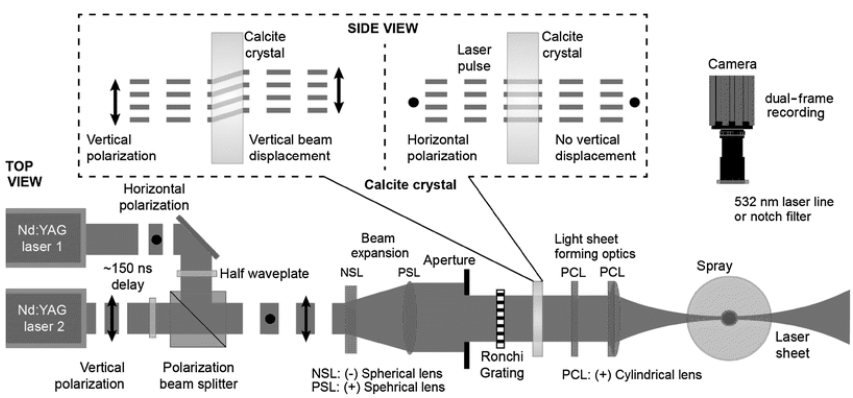

Fig. 39: The schematic of the 2p-SLIPI experimental setup for imaging transient sprays.

angle of 6.3°. By adjusting the frequency of the Ronchi grating together with the thickness of the crystal, a perfect shift in spatial phase between the two beams can be obtained. The camera should be able to record the two frames at a time delay as short as possible to freeze the spray motion. This can be achieved using dual-frame sCMOS or interline transfer CCD cameras. Depending on the signal that needs to be recorded, a laser line filter (for Mie scattering only), a notch filter (for LIF only) or a bandpass fluorescence filter (for part of the fluorescence) is used in front of the camera. Note that two cameras can be used when two signals need to be recorded simultaneously. More details of the experimental setup can be found in Paper V. The successive steps of the post-processing for the extraction of a final SLIPI image as follows:

Corrections for variations in light intensity

Prior to subtracting the two sub-images, it is important to correct for intensity fluctuations between them to ensure that the modulated component of the two sub-images alternate around a common intensity (background) *offset*. This procedure is especially important for measurements using two different lasers sources. Here, the post-processing scheme for intensity corrections is applied according to reference [16, 111]. The steps to follow are:

Step 1: First, the background *offset* of the sub-images are evaluated by calculating the mean intensity in a region where the signal is known to be zero (indicated by a blue dashed box in Fig. 40(a)). An offset-corrected image is obtained by subtracting the mean of the background *offset* in the original image.
Step 2: The average values of the offset-corrected image, A_{off}, are calculated and the mean value of these, M_R is deduced. Both offset-corrected sub-images in step 1 are then multiplied by M_R and divided by its corresponding A_{off}.
Step 3: The Fourier transform of both sub-images (from step 2) is calculated and multiplied by a low pass filter to filter out the modulation. The inverse Fourier transform of this filtered data is then calculated, referred to as I_{LPF}.
Step 4: The average value of the two I_{LPF} is then calculated, M_{LPF}, and the factor M_{LPF}/I_{LPF} is used as normalization map for the two sub-images.

Figures 40(a, b) show a pair of sub-images recorded with the 2p-SLIPI setup (LIF signal). Figures 40(c) and 40(d) show plots of the mean intensity of the two images, calculated over the region indicated by the white dashed boxes in Figs 40(a, b). Figure 40(c) displays the data before applying any intensity fluctuation corrections, where it can be observed that the detected intensities for the two sub-images are significantly different. Figure 40(d) shows the outcome of applying steps 1-4, illustrating that such differences can be compensated for

computationally. These graphs demonstrate the importance of addressing the issue with intensity variations/fluctuations between the recorded sub-images.

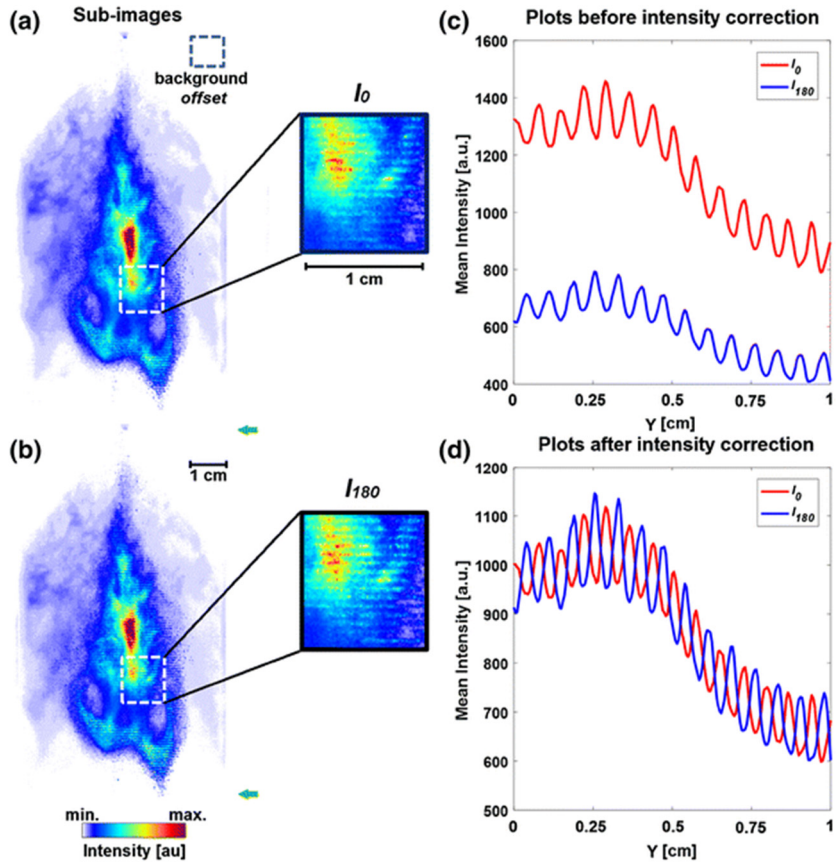

Fig. 40: Two modulated LIF sub-images of complementary phase are shown in (a) and (b). The plots of the mean intensity of I_0 and I_{180} from the indicated region (white-dashed box) are given in (c) without any intensity correction. The same plots are shown in (d) after the correction procedure for the variations in light intensity.

Post-processing: 2p-SLIPI

The two sub-images corrected from intensity variations (as shown in Fig. 40(b)) are subtracted and the absolute value of their subtraction $|\boldsymbol{I_0 - I_{180}}|$ is deduced. Figure 41(a) shows one of the modulated sub-images, $\boldsymbol{I_0}$, along with its Fourier transform. Figure 41(b) shows $|\boldsymbol{I_0 - I_{180}}|$ without applying the intensity correction procedure (see Fig. 40). The image shows an apparent residual line structure, having a spatial frequency corresponding to that of the incident modulation ν as shown by the Fourier transform. Figure 41(c) is obtained from the

absolute value of the subtraction between the two sub-images after applying the intensity correction. Although less apparent, this image also contains a residual line structure stretching across the entire image. This is also observed in the corresponding Fourier transform, which shows a clear modulation at a spatial frequency twice that of the incident modulation. To obtain a residual-free 'final' 2p-SLIPI image, a Gaussian low pass filter $F_{2\upsilon}$ is locally applied at the location of the residual frequencies, as shown in Fig. 41(d). It should be noted that any structural information appearing periodically at 2ν, i.e. residing within the indicated filter range (see Fig. 41(d)), is also removed in the final step of the procedure.

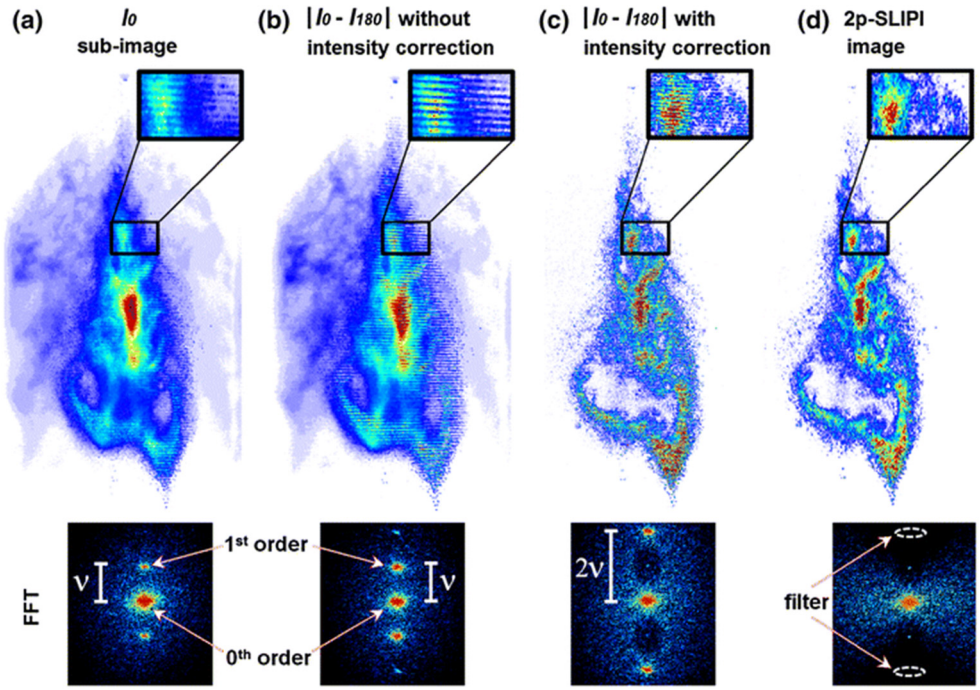

Fig. 41: Illustration of 2p-SLIPI extracted from post-processing of two sub-images. One of the modulated sub-images in (a) and subtracted images (without the intensity correction) in (b) along with their Fourier transforms, respectively. (c) Subtracted image produces an intermediate processed image and its Fourier transform with residuals appearing at 2ν instead of at ν as in (b). (d) 'Final' 2p-SLIPI image along with its Fourier transform, where the residuals in (c) have been suppressed. A band-rejection filter is locally applied in the region indicated in (d) to remove the residuals.

6.2 One-phase SLIPI (1p-SLIPI)

The reconstruction of SLIPI from just one sub-image, referred to as one-phase SLIPI (1p-SLIPI), has been demonstrated in turbid media by for the first time by Berrocal *et al.* [112] and more recently also for combustion studies based on Rayleigh thermometry by Kristensson *et al.* [57]. Recently, the approach is demonstrated in transient sprays, which is reported here as part of this thesis work.

1p-SLIPI optical setup

The description of a standard 1p-SLIPI optical setup is given in Fig. 42. This optical arrangement is simplified in comparison with the 2p-SLIPI setup presented in the previous sub-section 6.1. The polarizing beam splitter, the half-wave plates, and the calcite crystal are, here, no longer needed and the setup is based on the use of only one 532-nm-pulsed Nd:YAG laser. For 1p-SLIPI, either a square or a sinusoidal pattern can be employed to induce the desired spatial modulation on the incident light sheet. However, the use of Ronchi gratings is usually preferred to sinusoidal gratings as they are characterized by a higher laser damage threshold and they are cost-effective. Note that a 3p-SLIPI setup for temporally averaged imaging is obtained from the 1p-SLIPI setup by simply including a device that adequately shifts the spatial phase of the modulation. This is usually done by means of a motorized actuator, which displaces the grating along the direction of the modulated pattern. However, in the case of 3p-SLIPI, a sinusoidal pattern is preferred to reduce as much as possible the appearance of residual line on the final reconstructed SLIPI images.

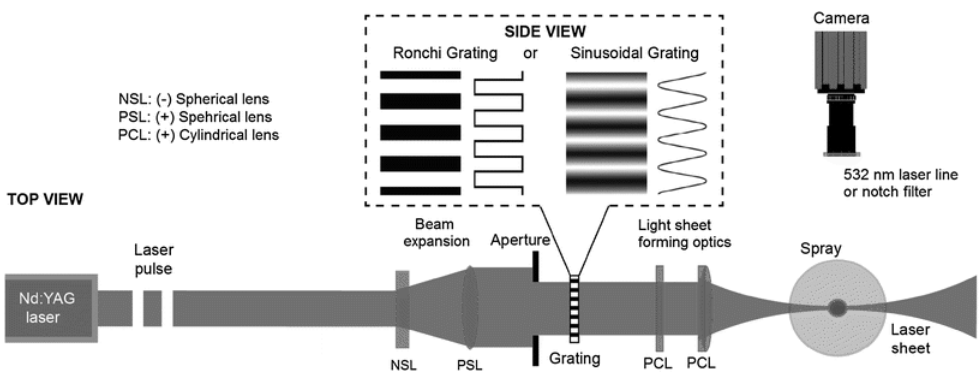

Fig. 42: Schematic of the 1p-SLIPI experimental setup: the setup consists of an Nd: YAG-pulsed laser source, some beam expansion optics, a transmission Ronchi or sinusoidal grating, and the sheet forming optics. Contrary to the 2p-SLIPI setup, the camera used here does not need a double-frame recording capability.

Finally, while 1p-SLIPI has the advantage of not being limited by dual-frame recordings, the technique has the disadvantage of being more demanding on using a high-frequency modulation to preserve a good image spatial resolution. Thus, the use of a lens objective which resolves the line structure equally well over the full image array (e.g., telecentric lenses), as well as the use of cameras having a large number of pixels, are recommended for 1p-SLIPI.

Post-processing: 1p-SLIPI

The lock-in detection algorithm of 1p-SLIPI is illustrated in Fig. 43. The sub-image and its Fourier transform are shown in (a, b), respectively.

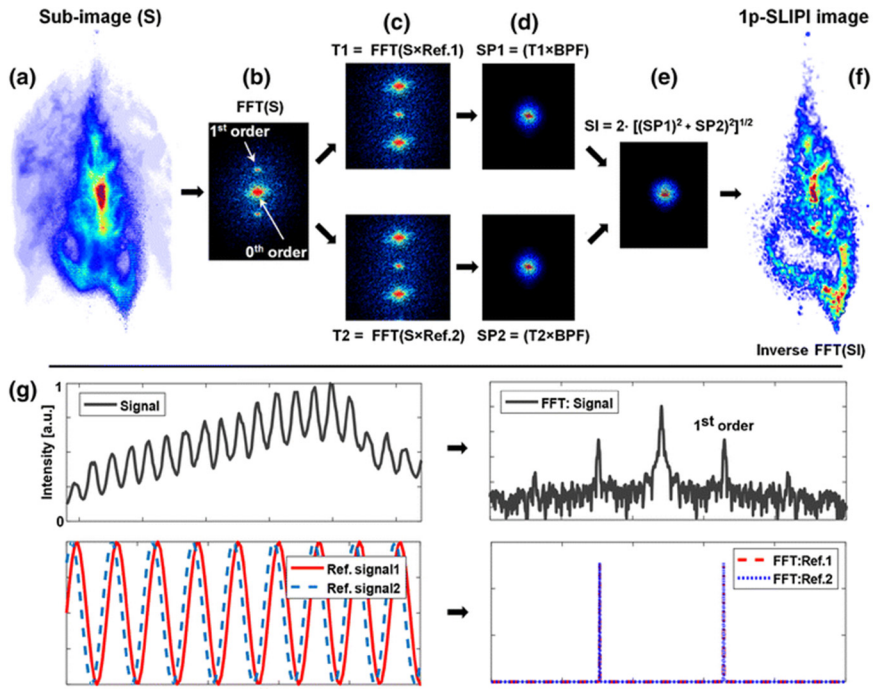

Fig. 43: Illustration of the lock-in detection algorithm of 1p-SLIPI. In (a) and (b): The modulated sub-image and its FFT, respectively. (a) The resulting signals T1 and T2 from the multiplication of the sub-image signal and the generated reference signals are shown. The reference signals are generated using the modulated signal frequency ("first order" in FFT), as shown in (g). When multiplied by the reference signal, the modulated intensity components of the sub-image in (a) are demodulated, while the non-modulated components are modulated. (d) Resulting SP1 and SP2 from the multiplication between the FFT images in (c) and BPF, respectively. (e) FFT of the SI signal is calculated. To extract this, first, the inverse FFT of both SP1 and SP2 is deduced, and then, the square root of the sum of $(SP1)^2$ and $(SP2)^2$ is obtained. (f) 'Final' 1p-SLIPI image of the spray, which is calculated from the inverse FFT of SI signal.

The first-order peak indicated in (b) corresponds to the modulation frequency of the incident illumination. Using this frequency, two sinusoidal reference signals with a phase-difference of 90° is generated as shown in (g) along with their FFT plots. The multiplication between the generated reference signals and the recorded sub-image matrix yields to T1 and T2 as shown in (c). This multiplication allows the "first order" peak and "zeroth order" peak to switch places. Thus, a modulated signal becomes demodulated. The signals of interest, SP1 and SP2 shown in (d), are obtained after the multiplication of T1 and T2 with a desired band-pass filter BPF; which is a rotationally symmetric two-dimensional Gaussian low-pass filter. The image (e) is deduced from the square root of the sum of the SP signals in square. Finally, the 1p-SLIPI image shown in (f) is finally deduced from the inverse Fourier transform of the SI signal.

6.3 2p-SLIPI droplet sizing

This section reports the investigation of spray formation and droplet sizing of ethanol and butanol fuels using 2p-SLIPI in combination with LIF/Mie ratio approach for droplet sizing. The atomization and evaporation behavior of multi-jet DISI-sprays are investigated in an injection chamber. The influence of the biofuels ethanol and butanol and fuel temperature on the spray structure and cyclic spray variation is analyzed. Results from paper VII are summarized here.

Description of the experiment

The 2p-SLIPI droplet sizing optical setup is similar to the setup given in Fig. 39. Four sub-images are simultaneously recorded on dual-frame mode with two scientific CMOS cameras (Imager sCMOS, LaVision GmbH), out of which a pair of two sub-images are for SLIPI-LIF image reconstruction and another pair for SLIPI-Mie image reconstruction. Each acquired sub-image is represented by 2560 × 2160 pixels. For simultaneous recording and for obtaining the same image field-of-view on both cameras, an in-house camera stage with the single objective is constructed. On the back of the objective, a cube beam splitter (70% reflection, 30% transmission) is fixed which distributes the incoming signals onto the two cameras. For the illumination of the spray two pulsed 532 nm Nd:YAG lasers (laser 1, Quanta Ray; and laser 2, Quantel Brilliant) with matched laser fluence and top hat beam profile are used. The pulse duration is in the order of 6 ns, while the pulse repetition rate is 10 Hz. The lines pattern on the light sheets is superimposed through a transmission Ronchi grating with four line-pairs/mm spatial frequency. The two overlapping incident laser sheets have a height of 90 mm and a thickness of approximately 500 μm. The time delay between the two

laser pulses is set to 750 ns. The short time difference allows the recording of the pair of modulated sub-images, required to generate the 2p-SLIPI image, while temporally freezing the spray in motion.The different polarization of the beams does not introduce uncertainties to the LIF and Mie-scattering signal (for the investigated spray, the droplet size distribution range is 5-20 µm and the Mie scattering simulations show the same light intensity both for p and s polarization in that diameter range). As the fluorescent tracer, an organic luminescence dye, Eosin-Y (Kingscote Chemicals, USA), is added at 0.5 vol.-% of the liquid fuel. The LIF emission is detected by using a 532 nm (17 nm FWHM) notch filter just in front of the sCMOS chip in order to exclude the excitation light. The Mie scattering signal is detected by using a 532 nm (1 nm FWHM) laser line filter. The spray chamber is operated with dry air at 0.2 Mpa (2 bar) and 293 K (20°C) which represents an early injection (during the suction stroke) at a high load engine operating point. The chamber design enables a variable fuel temperature. The injector is heated by a fluid-based heating circulator. The temperature of the nozzle tip is measured with a highly sensitive micro sheathed thermocouple (0.25 mm diameter, type K). It is assumed that the fuel adopts the injector temperature due to the long residence time of the fuel in the injector (the injection duration is relatively short - it is kept constant at 1800 µs- for an injection repetition rate of 1 Hz. For the shown experiments, the fuel temperatures are adjusted to 293 K (20°C) and 343 K (70°C). This fuel temperature variation should lead to small changes in the spray shape as well as droplet size distributions and with this study, the sensitivity of the SLIPI-technique is tested to resolve these variations. This temperature range is also relevant for cold and warm start conditions of the IC engine. The injection pressure is set to 8 Mpa (80 bar). A 5-hole DISI-injector (BOSCH) is utilized, where one jet is centrally separated from the others allowing unrestricted optical access. In this study, ethanol and butanol are investigated.

Figures 45 and 46 show the three instantaneous images of the LIF and Mie-scattering signals and their corresponding LIF/Mie ratio both for the ethanol and butanol sprays, respectively. The turbulent spray structure can be visualized only with instantaneous images while fluctuations in the spray shape and the vortex structures are not visible in the mean images. A good indication of cyclic variation is provided by the coefficient of variance in right columns. The acquisition time is 2552 µs aESOI. At the presented point in time, the nozzle has been closed. The modulated light sheets enter the spray from the left side and illuminate the central jet of the multi-jet spray. When comparing the LIF and the Mie images obtained using SLIPI it is noticed that a strong signal occurs at the spray front in both cases in Figs. 45 and 46. The signal of the LIF/Mie ratio also shows the largest intensities at the spray front and on the radial edges of the spray. The drag forces at the spray front support collision of the fuel droplets accompanied with droplet

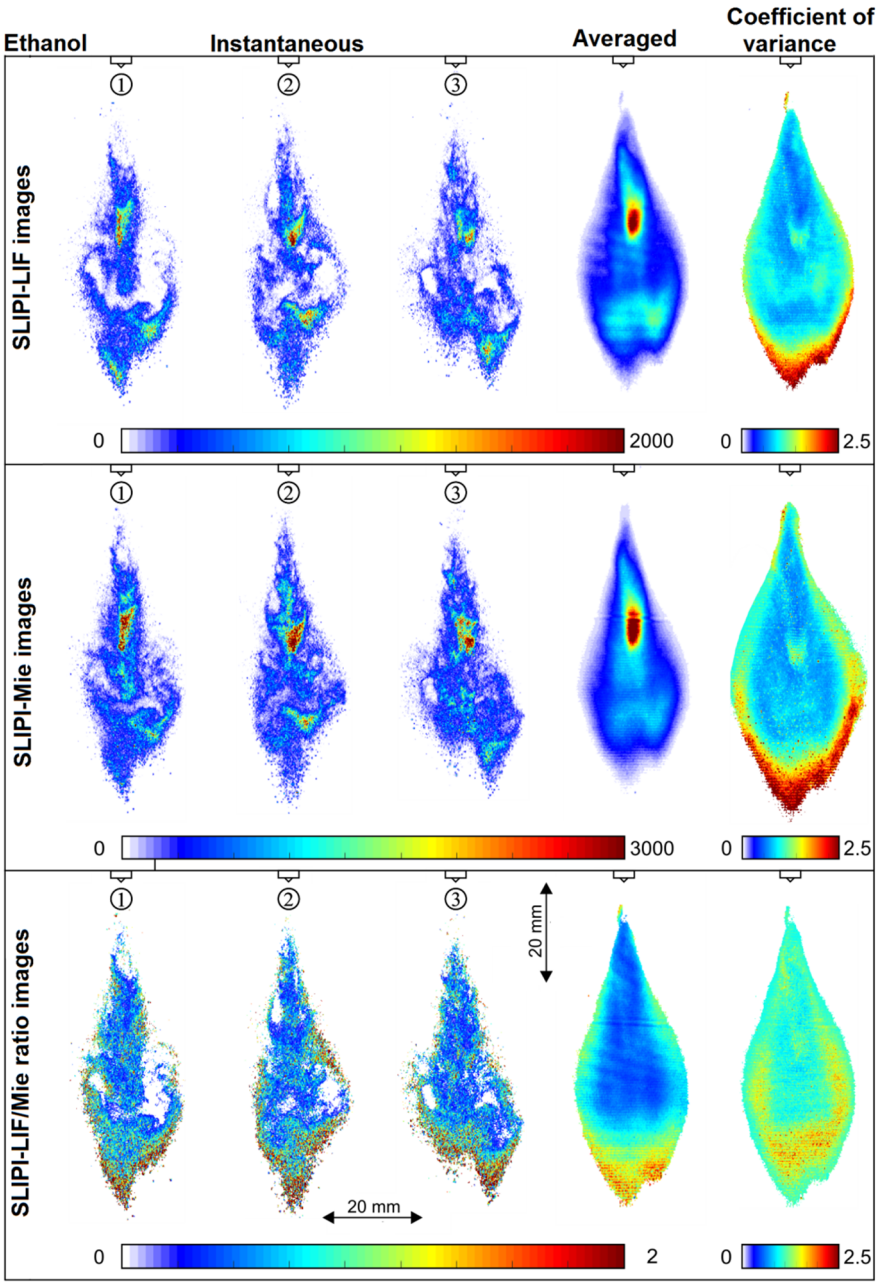

Fig. 45: Instantaneous and averaged images of ethanol as the coefficient of variance, 2552µs aESOI, 343 K(70°C) fuel temperature. (Images from paper VII).

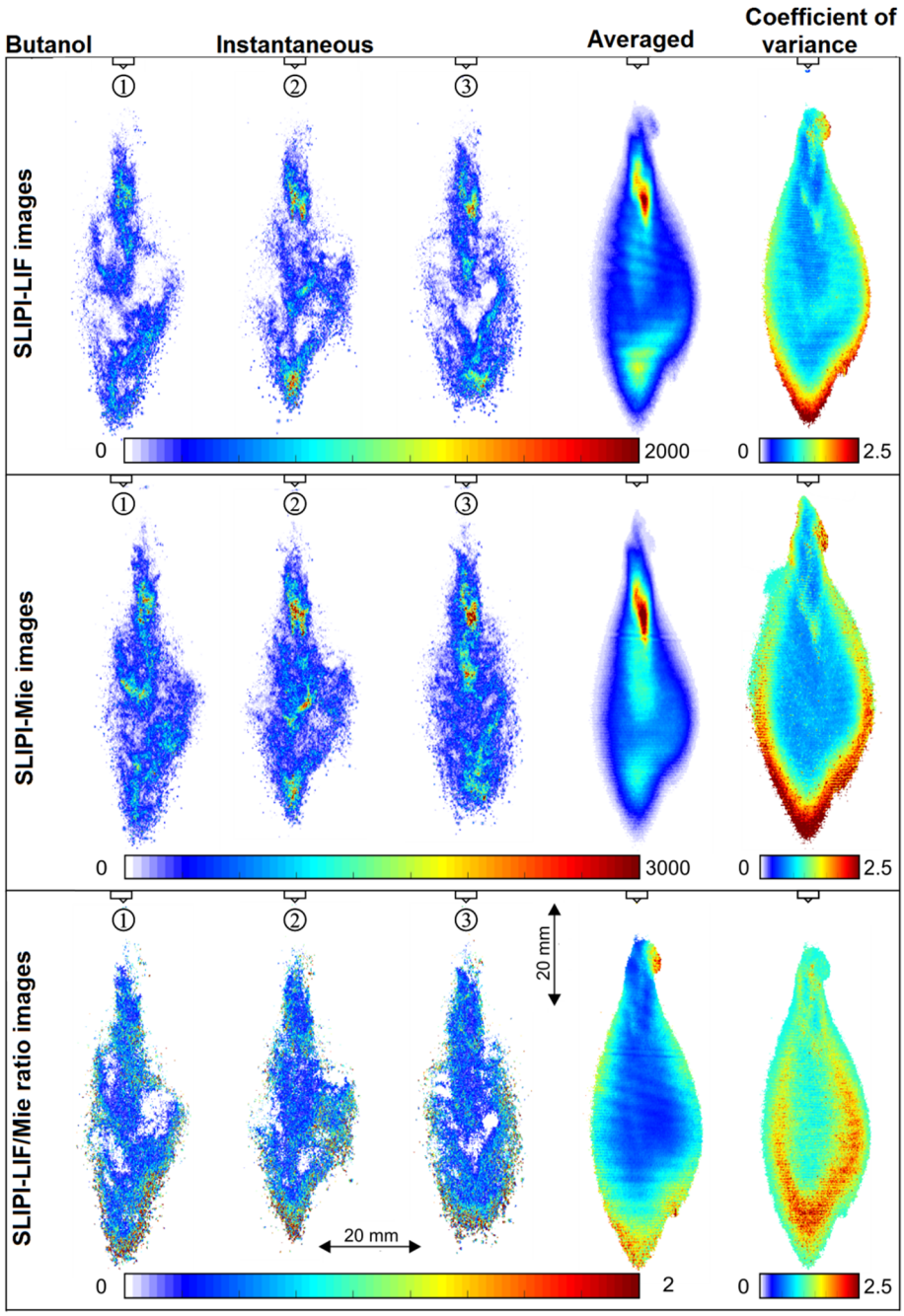

Fig. 46: Instantaneous and averaged images of butanol as the coefficient of variance, 2552µs aESOI, 343 K (70°C) fuel temperature. (Images from paper VII).

coalescence. This leads to larger droplets at the spray front, which is typical for DISI-sprays [68]. The instantaneous SLIPI-LIF/Mie ratio shows the same structure. Large cavities (produced by large turbulent eddies) are visible behind the spray front. The large cavities are characterized by a low LIF/Mie ratio in their center corresponding to small droplets. The evaporation of fuel may also lead to low LIF/Mie signals of the droplets in these spray regions. When comparing ethanol and butanol sprays it can be seen that the butanol sprays have larger penetration depth and a smaller spray angle. This is caused by the formation of larger droplets mainly due to the higher viscosity and surface tension of butanol. This leads to higher droplet momentum and reduced droplet deformation and breakup, thus lower surface specific drag forces.

7. Conclusions

In this thesis, a variety of SLIPI-based techniques were reported for droplet size, droplet concentration, and liquid temperature measurements in spray systems. The temporally averaged 3p-SLIPI-based measurements were applied on steady hollow-cone water sprays generated from pressure swirl atomizers. In addition, two novel approaches, 2p-SLIPI and 1p-SLIPI, were developed for the investigation of transient biofuel DISI sprays. The main results and highlights of the applied optical methods can be summarized as follows:

SLIPI-LIF/Mie planar droplet sizing technique

- This scheme was used for extracting a 2D map of the droplets SMD in steady hollow-cone water sprays.
- Even for the case of a fairly dilute spray with an OD of 1, where single scattering events were the majority, the "conventional" LIF/Mie technique still remains largely affected by errors introduced by multiple light scattering.
- The SLIPI-LIF/Mie results were calibrated and compared with measurement data from PDA.
- An appropriate calibration process was not possible when using the "conventional" approach, as two SMD values were assigned for a single LIF/Mie ratio value. On the contrary, for the SLIPI-LIF/Mie, a calibration curve was possible to obtain.
- The SLIPI-LIF/Mie results were in good agreement with the data from the PDA measurements.

SLIPI-LIF/Mie ratio droplet sizing and light transmission imaging

- This scheme was first used for extracting 3D map of the droplets SMD and 2D map of optical depth in hollow-cone water sprays.
- The 3D maps helped depicting a global distribution of droplet SMD and showed an asymmetry in droplet size from the probed spray.
- In another investigation, the scheme was applied for the simultaneous imaging of the LIF/Mie ratio and light transmission images for an optically dilute spray with an OD of approximately 1. The droplet SMD and extinction-coefficient were first extracted using this approach. These two spray quantities were

further used to deduce 2D maps of the droplet SMD, droplet number density, and LVF. Finally, using all the 2D layers, a 3D map of LVF is reconstructed.

- The SMD measurements were verified with PDA measurement data. The droplet number density and liquid volume fraction measurements, however, require further verification with complementary experimental data.

SLIPI-two color LIF ratio thermometry

- This scheme was used for measuring water temperature in both a cuvette and a steady hollow-cone water spray.
- Fluorescein dye was used a temperature-sensitive tracer.
- By removing the unwanted background interferences using SLIPI, there was a significant improvement in terms of temperature sensitivity with more pronounced temperature gradients within the spray.
- The two-color LIF ratio was independent of laser power at a constant dye concentration, while it was significantly dependent on the dye concentration at a constant laser power. This observation is related to self-absorption effects due to the partial overlapping of the absorption and emission spectra of fluorescein.

Two-phase SLIPI technique

- A novel optical setup was developed for instantaneous SLIPI imaging in optically dense transient ethanol DISI sprays.
- The setup was developed by utilizing the birefringence property of a calcite crystal.
- The fast formation of polydispersed droplets and the appearance of voids after fuel injection were investigated by the simultaneous detection of Mie scattering and LIF signals, allowing a significantly improved visualization of the spray pattern.
- In a second investigation, 2p-SLIPI-LIF/Mie ratio was applied for comparing ethanol and butanol DISI sprays in terms of spray patterns and droplet SMD.
- In equivalent conditions, butanol consistently showed larger spray penetration than ethanol. This behavior was due to the higher surface tension and viscosity of butanol, resulting in the formation of larger droplets and larger SMDs in the whole spray region. The butanol injection also showed larger cyclic variations in the spray shape from injection to injection, which is also explained by the larger fuel viscosity.

One-phase SLIPI technique

- A novel image post-processing routine was reported for the generation of a SLIPI image reconstructed from a single modulated sub-image where it was demonstrated for single-shot imaging on a transient DISI spray.

- The approach was compared with 2p-SLIPI detection, where 1p-SLIPI is limited to the analysis of global features due to loss of image spatial resolution.

Future considerations

- The precision and accuracy of a droplet sizing scheme in steady sprays need to be thoroughly investigated. These measurements in combination with PDA data are possible for the case of steady sprays. However, in the case of rapid changes in the droplet size in transient sprays, PDA data might not be adequate to calibrate instantaneous images. The SLIPI-LIF/Mie instantaneous images require a calibration procedure where droplets of known and controlled size are generated from a monodisperse droplet generator.
- 2p-SLIPI and 1p-SLIPI schemes can be employed for measurements in transient sprays under varying conditions, such as different injectors, different fuels, and different chamber conditions.
- 2p-SLIPI and 1p-SLIPI methods can be used for particle tracking velocimetry measurements in transient sprays to investigate spray dynamics in detail.
- Exciplex-LIF in combination with SLIPI can be investigated for droplet sizing under highly evaporating conditions.
- The use of telecentric camera objectives should be explored for maintaining constant modulation depth of structured lines pattern throughout the viewable area.
- Finally, a large dataset of different spray quantities measured with SLIPI-based methods for different spray conditions can be generated preferably in collaboration with spray modelers to use the results for validation purposes.

References

1. Park, S.H., H.J. Kim, and C.S. Lee, *Effect of Multiple Injection Strategies on Combustion and Emission Characteristics in a Diesel Engine.* Energy & Fuels, 2016. **30**(2): p. 810-818.
2. Zhao, F., M.C. Lai, and D.L. Harrington, *Automotive spark-ignited direct-injection gasoline engines.* Progress in Energy and Combustion Science, 1999. **25**(5): p. 437-562.
3. Han, Z., et al., *Mechanism of Soot and NOx Emission Reduction Using Multiple-injection in a Diesel Engine*. 1996, SAE International.
4. Todd, D.F. and E.P. Scott, *Spray measurement technology: a review.* Measurement Science and Technology, 2015. **26**(1): p. 012002.
5. Lemoine, F. and G. Castanet, *Temperature and chemical composition of droplets by optical measurement techniques: a state-of-the-art review.* Experiments in Fluids, 2013. **54**(7): p. 1572.
6. Linne, M., *Imaging in the optically dense regions of a spray: A review of developing techniques.* Progress in Energy and Combustion Science, 2013. **39**(5): p. 403-440.
7. Tropea, C., *Optical Particle Characterization in Flows.* Annual Review of Fluid Mechanics, 2011. **43**(1): p. 399-426.
8. Lee, K. and J. Abraham, *Spray Applications in Internal Combustion Engines*, in *Handbook of Atomization and Sprays: Theory and Applications*, N. Ashgriz, Editor. 2011, Springer US: Boston, MA. p. 777-810.
9. Kristensson, E., et al., *Structured illumination for 3-D Mie imaging and 2-D attenuation measurements in optically dense sprays.* Proceedings of the Combustion Institute, 2011. **33**(1): p. 855-861.
10. Hanson, R.K., *Combustion diagnostics: Planar imaging techniques.* Symposium (International) on Combustion, 1988. **21**(1): p. 1677-1691.
11. Ueda, T., et al., *Measurement of three-dimensional flame structure by combined laser diagnostics.* Journal of Mechanical Science and Technology, 2009. **23**(7): p. 1813-1820.
12. Masri, A.R., *Turbulent Combustion of Sprays: From Dilute to Dense.* Combustion Science and Technology, 2016. **188**(10): p. 1619-1639.
13. Sick, V. and B. Stojkovic, *Attenuation effects on imaging diagnostics of hollow-cone sprays.* Applied Optics, 2001. **40**(15): p. 2435-2442.
14. Talley, D., et al., *Accounting for laser sheet extinction in applying PLLIF to sprays*, in *34th Aerospace Sciences Meeting and Exhibit*. 1996, American Institute of Aeronautics and Astronautics.

15. Hyeonseok, K., et al., *Analysis of signal attenuation for quantification of a planar imaging technique.* Measurement Science and Technology, 2003. **14**(10): p. 1829.
16. Kristensson, E., *Structured Laser Illumination Planar Imaging SLIPI Applications for Spray Diagnostics, PhD Thesis, Lund University, Lund.* 2012.
17. Berrocal, E., *Multiple Scattering of Light in Optical Diagnostics of Dense Sprays and Other Complex Turbid Media, Ph.D. thesis, Cranfield University, Cranfield.* 2006.
18. Adrian, R.J. and J. Westerweel, *Particle Image Velocimetry*. 2011, Cambridge; New York: Cambridge University Press.
19. Westerweel, J., G.E. Elsinga, and R.J. Adrian, *Particle Image Velocimetry for Complex and Turbulent Flows.* Annual Review of Fluid Mechanics, 2013. **45**(1): p. 409-436.
20. Li, T., K. Nishida, and H. Hiroyasu, *Droplet size distribution and evaporation characteristics of fuel spray by a swirl type atomizer.* Fuel, 2011. **90**(7): p. 2367-2376.
21. Yeh, C.-N., H. Kosaka, and T. Kamimoto, *Fluorescence/Scattering Image Technique for Particle Sizing in Unsteady Diesel Spray.* Transactions of the Japan Society of Mechanical Engineers Series B, 1993. **59**(568): p. 4008-4013.
22. Le Gal, P., N. Farrugia, and D.A. Greenhalgh, *Laser Sheet Dropsizing of dense sprays.* Optics & Laser Technology, 1999. **31**(1): p. 75-83.
23. Domann, R. and Y. Hardalupas, *Quantitative Measurement of Planar Droplet Sauter Mean Diameter in Sprays using Planar Droplet Sizing.* Particle & Particle Systems Characterization, 2003. **20**(3): p. 209-218.
24. Malarski, A., et al., *Laser sheet dropsizing based on two-dimensional Raman and Mie scattering.* Applied Optics, 2009. **48**(10): p. 1853-1860.
25. Zeng, W., et al., *Laser sheet dropsizing of evaporating sprays using simultaneous LIEF/MIE techniques.* Proceedings of the Combustion Institute, 2013. **34**(1): p. 1677-1685.
26. Coppeta, J. and C. Rogers, *Dual emission laser induced fluorescence for direct planar scalar behavior measurements.* Experiments in Fluids, 1998. **25**(1): p. 1-15.
27. Sakakibara, J. and R.J. Adrian, *Whole field measurement of temperature in water using two-color laser induced fluorescence.* Experiments in Fluids, 1999. **26**(1): p. 7-15.
28. Lavieille, P., et al., *Evaporating and combusting droplet temperature measurements using two-color laser-induced fluorescence.* Experiments in Fluids, 2001. **31**(1): p. 45-55.
29. Brübach, J., A. Patt, and A. Dreizler, *Spray thermometry using thermographic phosphors.* Applied Physics B, 2006. **83**(4): p. 499.
30. Omrane, A., G. Särner, and M. Aldén, *2D-temperature imaging of single droplets and sprays using thermographic phosphors.* Applied Physics B, 2004. **79**(4): p. 431-434.
31. Su, W., et al., *Quantitative Study of Concentration and Temperature of a Diesel Spray by Using Planar Laser Induced Exciplex Fluorescence Technique.* SAE Int. J. Engines, 2010. **3**(1): p. 717-732.

32. Zhang, Y., et al., *Droplet temperature measurement based on 2-color laser-induced exciplex fluorescence.* Experiments in Fluids, 2013. **54**(8): p. 1583.
33. Melton, L.A., *Spectrally separated fluorescence emissions for diesel fuel droplets and vapor.* Applied Optics, 1983. **22**(14): p. 2224-2226.
34. Todd, D.F., et al., *Quantitative liquid and vapor distribution measurements in evaporating fuel sprays using laser-induced exciplex fluorescence.* Measurement Science and Technology, 2009. **20**(12): p. 125401.
35. Hajime, F., et al., *Two-dimensional imaging of fuel-vapour concentration by use of LIEF technique during mixture formation process in a DI diesel engine.* Measurement Science and Technology, 2002. **13**(3): p. 391.
36. Pastor, J.V., et al., *Planar Laser-Induced Fluorescence fuel concentration measurements in isothermal Diesel sprays.* Optics Express, 2002. **10**(7): p. 309-323.
37. Payri, R., et al., *Fuel concentration in isothermal Diesel sprays through structured planar laser imaging measurements.* International Journal of Heat and Fluid Flow, 2012. **34**: p. 98-106.
38. van Cruyningen, I., A. Lozano, and R.K. Hanson, *Quantitative imaging of concentration by planar laser-induced fluorescence.* Experiments in Fluids, 1990. **10**(1): p. 41-49.
39. *Development of quantitative measurement of fuel mass distribution using planar imaging technique.* Journal of Visualization, 2006. **9**(2): p. 161.
40. Kristensson, E., E. Berrocal, and M. Aldén, *Quantitative 3D imaging of scattering media using structured illumination and computed tomography.* Optics Express, 2012. **20**(13): p. 14437-14450.
41. Wellander, R., et al., *Three-dimensional measurement of the local extinction coefficient in a dense spray.* Measurement Science and Technology, 2011. **22**(12): p. 125303.
42. Berrocal, E., et al., *Quantitative imaging of a non-combusting diesel spray using structured laser illumination planar imaging.* Applied Physics B, 2012. **109**(4): p. 683-694.
43. Labs, J. and T. Parker, *Two-dimensional droplet size and volume fraction distributions from the near-injector region of high-pressure diesel sprays.* Atomization and Sprays, 2006. **16**(7): p. 843-855.
44. Deshmukh, D. and R.V. Ravikrishna, *A method for measurement of planar liquid volume fraction in dense sprays.* Experimental Thermal and Fluid Science, 2013. **46**: p. 254-258.
45. Berrocal, E., et al., *Application of structured illumination for multiple scattering suppression in planar laser imaging of dense sprays.* Optics Express, 2008. **16**(22): p. 17870-17881.
46. Kristensson, E., et al., *High-speed structured planar laser illumination for contrast improvement of two-phase flow images.* Optics Letters, 2008. **33**(23): p. 2752-2754.
47. Mishra, Y.N., et al., *Comparison between two-phase and one-phase SLIPI for instantaneous imaging of transient sprays.* Experiments in Fluids, 2017. **58**(9): p. 110.

48. Kristensson, E., et al., *Analysis of multiple scattering suppression using structured laser illumination planar imaging in scattering and fluorescing media.* Optics Express, 2011. **19**(14): p. 13647-13663.
49. Kristensson, E., et al., *Nanosecond structured laser illumination planar imaging for single-shot imaging of dense sprays.* 2010. **20**(4): p. 337-343.
50. Mishra, Y.N., E. Kristensson, and E. Berrocal, *Reliable LIF/Mie droplet sizing in sprays using structured laser illumination planar imaging.* Optics Express, 2014. **22**(4): p. 4480-4492.
51. Mishra, Y.N., Kristensson, E., Berrocal, E. *3D droplet sizing and 2D optical depth measurements in sprays using SLIPI based techniques*. in *LISBON Symposium*. 2016. Lisbon.
52. Storch, M., et al., *Two-phase SLIPI for instantaneous LIF and Mie imaging of transient fuel sprays.* Optics Letters, 2016. **41**(23): p. 5422-5425.
53. Kapusta, Ł.J. and A. Teodorczyk, *Laser diagnostics for urea-water solution spray characterization.* MATEC Web Conf., 2017. **118**: p. 00029.
54. Mishra, Y.N., et al., *Thermometry in aqueous solutions and sprays using two-color LIF and structured illumination.* Optics Express, 2016. **24**(5): p. 4949-4963.
55. Zentgraf, F., et al., *Application of structured illumination to gas phase thermometry using thermographic phosphor particles: a study for averaged imaging.* Experiments in Fluids, 2017. **58**(7): p. 82.
56. Grosshans, H., et al., *Prediction and Measurement of the local extinction coefficient in sprays for 3D simulation/experiment data comparison.* International Journal of Multiphase Flow, 2015. **72**: p. 218-232.
57. Kristensson, E., et al., *Advancements in Rayleigh scattering thermometry by means of structured illumination.* Proceedings of the Combustion Institute, 2015. **35**(3): p. 3689-3696.
58. Kempema, N.J. and M.B. Long, *Quantitative Rayleigh thermometry for high background scattering applications with structured laser illumination planar imaging.* Applied Optics, 2014. **53**(29): p. 6688-6697.
59. Larsson, K., et al., *Single-shot photofragment imaging by structured illumination.* Optics Letters, 2015. **40**(21): p. 5019-5022.
60. Kristensson, E., et al., *Instantaneous 3D imaging of flame species using coded laser illumination.* Proceedings of the Combustion Institute, 2017. **36**(3): p. 4585-4591.
61. *Basic Processes in Atomization*, in *Atomization and Sprays*. 2017, CRC Press. p. 17-54.
62. Chigier, N., *An assessment of spray technology - Editorial.* Atomization and Sprays, 1993. **3**(4): p. 365-371.
63. Rayleigh, L., *On The Instability Of Jets.* Proceedings of the London Mathematical Society, 1878. **s1-10**(1): p. 4-13.
64. *Regimes of Jet Breakup and Breakup Mechanisms (Physical Aspects)*, in *Recent Advances in Spray Combustion: Spray Atomization and Drop Burning Phenomena*. 1996, American Institute of Aeronautics and Astronautics. p. 109-135.

65. Bonhoeffer, B., A. Kwade, and M. Juhnke, *Impact of Formulation Properties and Process Parameters on the Dispensing and Depositioning of Drug Nanosuspensions Using Micro-Valve Technology.* Journal of Pharmaceutical Sciences. **106**(4): p. 1102-1110.
66. Dumouchel, C., *On the experimental investigation on primary atomization of liquid streams.* Experiments in Fluids, 2008. **45**(3): p. 371-422.
67. Tropea, C., *Techniques of Atomization - Overview* 2015: Darmstadt.
68. *Fundamentals of Mixture Formation in Engines*, in *Mixture Formation in Internal Combustion Engine*. 2006, Springer Berlin Heidelberg: Berlin, Heidelberg. p. 5-46.
69. Mugele, R.A. and H.D. Evans, *Droplet Size Distribution in Sprays.* Industrial & Engineering Chemistry, 1951. **43**(6): p. 1317-1324.
70. Vesilind, P.A., *The Rosin-Rammler particle size distribution.* Resource Recovery and Conservation, 1980. **5**(3): p. 275-277.
71. Tanner, F.X., *Evaporating Sprays*, in *Handbook of Atomization and Sprays: Theory and Applications*, N. Ashgriz, Editor. 2011, Springer US: Boston, MA. p. 263-278.
72. Landry, E.S., et al., *Droplet evaporation: A molecular dynamics investigation.* Journal of Applied Physics, 2007. **102**(12): p. 124301.
73. Düwel I. , K.T., Schorr J. , Schulz C. , Wolfrum J. . *Application of fuel tracers with different volatilities for planar LIF/Mie drop sizing in evaporating systems*. in *9th International Conference on Liquid Atomization and Spray Systems* 2003.
74. *Fuel injection*: http://wikicars.org/en/Fuel_injection.
75. *Light scattering by small particles. By H. C. van de Hulst. New York (John Wiley and Sons), London (Chapman and Hall), 1957. Pp. xiii, 470; 103 Figs.; 46 Tables. 96s.* Quarterly Journal of the Royal Meteorological Society, 1958. **84**(360): p. 198-199.
76. Walter Schäfer, T.C., Wolfgang Elsäber. *Determination of Size and Refractive Index of a Single Water Droplet by Using a Light Source with Short Coherence Length (LED)*. in *15th Int Symp on Applications of Laser Techniques to Fluid Mechanics*. 2010. Lisbon, Portugal.
77. Charalampous, G. and Y. Hardalupas, *Numerical evaluation of droplet sizing based on the ratio of fluorescent and scattered light intensities (LIF/Mie technique).* Applied Optics, 2011. **50**(9): p. 1197-1209.
78. Tu, C., et al., *A Review of Experimental Techniques for Measuring Micro- to Nano-Particle-Laden Gas Flows.* Applied Sciences, 2017. **7**(2): p. 120.
79. *Practical Course Biophysics: Absorption and Fluorescence Spectroscopy*: www.dkfz.de/Macromol/teaching/files/fluorescence_practical.pdf.
80. Domann, R. and Y. Hardalupas, *A Study of Parameters that Influence the Accuracy of the Planar Droplet Sizing (PDS) Technique.* Particle & Particle Systems Characterization, 2001. **18**(1): p. 3-11.
81. Prahl, S.A., M.J.C. van Gemert, and A.J. Welch, *Determining the optical properties of turbid media by using the adding–doubling method.* Applied Optics, 1993. **32**(4): p. 559-568.

82. Kuga, Y. and A. Ishimaru, *Modulation transfer function of layered inhomogeneous random media using the small-angle approximation.* Applied Optics, 1986. **25**(23): p. 4382-4385.
83. Jermy, M.C. and A. Allen, *Simulating the effects of multiple scattering on images of dense sprays and particle fields.* Applied Optics, 2002. **41**(20): p. 4188-4196.
84. Berrocal, E., et al., *Crossed source–detector geometry for a novel spray diagnostic: Monte Carlo simulation and analytical results.* Applied Optics, 2005. **44**(13): p. 2519-2529.
85. Berrocal, E., I. Meglinski, and M. Jermy, *New model for light propagation in highly inhomogeneous polydisperse turbid media with applications in spray diagnostics.* Optics Express, 2005. **13**(23): p. 9181-9195.
86. Berrocal, E., et al., *Laser light scattering in turbid media Part I: Experimental and simulated results for the spatial intensity distribution.* Optics Express, 2007. **15**(17): p. 10649-10665.
87. Berrocal, E., et al., *Laser light scattering in turbid media Part II: Spatial and temporal analysis of individual scattering orders via Monte Carlo simulation.* Optics Express, 2009. **17**(16): p. 13792-13809.
88. Fansler, T. and S. Parrish, *Spray measurement technology: a review.* Measurement Science and Technology, 2015. **26**(1): p. 012002.
89. Coghe, A. and G.E. Cossali, *Quantitative optical techniques for dense sprays investigation: A survey.* Optics and Lasers in Engineering, 2012. **50**(1): p. 46-56.
90. Melton, L.A. and J.F. Verdieck, *Vapor/Liquid Visualization for Fuel Sprays.* Combustion Science and Technology, 1985. **42**(3-4): p. 217-222.
91. Cavaliere, A., et al., *Analysis of diesel sprays through two-dimensional laser light scattering.* Symposium (International) on Combustion, 1989. **22**(1): p. 1973-1981.
92. Stefan, B., et al., *Application of femtosecond lasers to the polarization ratio technique for droplet sizing.* Measurement Science and Technology, 2013. **24**(2): p. 025203.
93. Hofeldt, D.L., *Full-field measurements of particle size distributions. II: experimental comparison of the polarization ratio and scattered intensity methods.* Applied Optics, 1993. **32**(36): p. 7559-7567.
94. Bruchhausen, M., F. Guillard, and F. Lemoine, *Instantaneous measurement of two-dimensional temperature distributions by means of two-color planar laser induced fluorescence (PLIF).* Experiments in Fluids, 2005. **38**(1): p. 123-131.
95. Aldén, M., et al., *Thermographic phosphors for thermometry: A survey of combustion applications.* Progress in Energy and Combustion Science, 2011. **37**(4): p. 422-461.
96. Sankar, S.V., et al., *Rapid Characterization of Fuel Atomizers Using an Optical Patternator.* Journal of Engineering for Gas Turbines and Power, 1999. **121**(3): p. 409-414.
97. Jermy, M.C. and D.A. Greenhalgh, *Planar dropsizing by elastic and fluorescence scattering in sprays too dense for phase Doppler measurement.* Applied Physics B, 2000. **71**(5): p. 703-710.

98. Sangon, P., et al., *Measurement of droplet size distribution of gasoline direct injection spray by droplet generator and planar image technique.* Measurement Science and Technology, 2002. **13**(6): p. 859.
99. Kannaiyan, K., M.V.K. Banda, and A. Vaidyanathan, *Planar Sauter Mean Diameter measurements in liquid centered swirl coaxial injector using Laser Induced Fluorescence, Mie scattering and laser diffraction techniques.* Acta Astronautica, 2016. **123**: p. 257-270.
100. Frackowiak, B. and C. Tropea, *Numerical analysis of diameter influence on droplet fluorescence.* Applied Optics, 2010. **49**(12): p. 2363-2370.
101. D. Stepowski, O.W., C. Roze, and T. Girasole. *Account for extinction and multiple scattering in planar droplet sizing of dense sprays*. in *13th International Symposium of Laser Techniques to Fluids Mechanics*. 2006. LISBON.
102. Kim, M. and M. Yoda, *Dual-tracer fluorescence thermometry measurements in a heated channel.* Experiments in Fluids, 2010. **49**(1): p. 257-266.
103. Fenner, A. and P. Stephan, *Two dye combinations suitable for two-color/two-dye laser-induced fluorescence thermography for ethanol.* Experiments in Fluids, 2017. **58**(6): p. 65.
104. Chaze, W., et al., *Spatially and temporally resolved measurements of the temperature inside droplets impinging on a hot solid surface.* Experiments in Fluids, 2017. **58**(8): p. 96.
105. Castanet, G., et al., *Measurement of the temperature distribution within monodisperse combusting droplets in linear streams using two-color laser-induced fluorescence.* Experiments in Fluids, 2003. **35**(6): p. 563-571.
106. Perrin, L., G. Castanet, and F. Lemoine, *Characterization of the evaporation of interacting droplets using combined optical techniques.* Experiments in Fluids, 2015. **56**(2): p. 29.
107. Neil, M.A.A., R. Juškaitis, and T. Wilson, *Method of obtaining optical sectioning by using structured light in a conventional microscope.* Optics Letters, 1997. **22**(24): p. 1905-1907.
108. Bohren, C.F. and D.R. Huffman, *Appendixes: Computer Programs*, in *Absorption and Scattering of Light by Small Particles*. 2007, Wiley-VCH Verlag GmbH. p. 475-476.
109. Polster, S., *Temperature mapping of liquids using two-colour LIF ratio and SLIPI: Application for spray thermometry*. 2014, University of Erlangen-Nuremberg.
110. Kristensson, E., E. Berrocal, and M. Aldén, *Two-pulse structured illumination imaging.* Optics Letters, 2014. **39**(9): p. 2584-2587.
111. Cole, M.J., et al., *Time-domain whole-field fluorescence lifetime imaging with optical sectioning.* Journal of Microscopy, 2001. **203**(3): p. 246-257.
112. Berrocal, E., Johnsson, J., Kristensson, E., Alden, M., *Single scattering detection in turbid media using single-phase structured illumination filtering.* Journal of the European Optical Society - Rapid publications; Vol 7 (2012), 2012.

Summary of articles

Paper I: Three-phase SLIPI (3p-SLIPI) was applied in combination with LIF/Mie droplet sizing in a steady hollow-cone water spray for 2D mapping of the droplet SMD. First, the conventional LIF/Mie ratio and SLIPI-LIF/Mie ratio were compared for an optically dilute spray. When calibrating the ratio of two detection schemes with SMD measured by a phase Doppler anemometry system, it was only successful with the SLIPI-LIF/Mie ratio. It was concluded that multiple light scattering effects impede the conventional ratio that too for an optical depth = 1.

I performed the measurements together with Edouard. I did the majority of the data post-processing. Elias helped me with the calibration procedure. I produced all the illustrations and was responsible for the preparation of the manuscript together with Edouard.

Paper II: Temporally averaged 3p-SLIPI was employed in combination with two-color LIF thermometry for 2D mapping of temperature in aqueous solutions stored in a transparent glass cuvette, and on a steady hollow-cone water spray. Two-color LIF ratio from conventional and SLIPI detection are compared. By suppressing the unwanted background interferences using SLIPI, we observe both significant improvements in terms of temperature sensitivity as well as more pronounced temperature gradients within the spray.

Stefanie Polster and Edouard Berrocal initiated the two-color LIF thermometry project. Stefanie Polster investigated the temperature-sensitive properties of the dye tracer. She worked on the selection of adequate optical filters for the thermometry measurements. I performed the cuvette measurements, while the spray measurements were conducted together with Fahed Abou Nada. I performed the data post-processing, produced most of the illustrations, and was responsible for the preparation of the manuscript.

Paper III: SLIPI-LIF/Mie ratio droplet sizing is applied in combination with the SLIPI-scan approach for 3D mapping of the droplet SMD and 2D mapping of the droplet OD in a steady asymmetric hollow-cone water spray. To reconstruct a 3D map, the spray is probed with an SLIPI laser sheet in a bread-slicing manner to generate several 2D slices of the LIF/Mie ratio. These 2D slices are used together

to form a 3D map. Light transmission on a dyed cuvette for each layer of probed spray is used to calculate the corresponding OD values.

I constructed the experimental setup and conducted all the measurements. I was responsible for the image post-processing and the preparation of the manuscript.

Paper IV: A novel two-phase SLIPI (2p-SLIPI) optical setup exploiting the birefringence of calcite crystal is reported for instantaneous SLIPI. The simultaneous detection of LIF and Mie imaging along with their intensity ratio was demonstrated on transient ethanol DISI sprays.

Michael Storch and Edouard Berrocal initiated the project. I and Matthias Koegl did the measurements. I post-processed the data together with Elias Kristensson. I produced all the illustrations and was responsible for the preparation of the manuscript.

Paper V: A comparison between 2p-SLIPI and single-phase SLIPI (1p-SLIPI) detection approaches and their application in instantaneous LIF and Mie imaging is demonstrated on ethanol DISI sprays.

I and Matthias Koegl did the experiments. Elias Kristensson guided me in the lock-in detection approach for 1p-SLIPI. I was responsible for the generation of SLIPI images, while Joakim Jönsson generated images with Monte-Carlo simulation. I prepared illustrations and wrote the manuscript together with Edouard Berrocal.

Paper VI: SLIPI-LIF/Mie ratio droplet sizing is applied in combination with SLIPI-scan approach for layerwise 2D mapping of the droplet SMD, droplet number density, and liquid volume fraction (LVF), in an steady asymmetric hollow-cone water spray. Using several 2D layers, a 3D reconstruction of LVF is presented.

I conducted the experiments. Timo Tscharntke was responsible for the SLIPI-scan data post-processing for the extinction-coefficient calculations. I produced all the images and plots and wrote the manuscript.

Paper VII: Using 2p-SLIPI, ethanol and butanol DISI sprays are investigated in terms of droplet size.

I and Matthias Koegl did the SLIPI measurements. Chris and Michael did the PDA measurements. I helped Matthias with the 2p-SLIPI post-processing. Matthias generated all the images and wrote the manuscript together with Lars.

Media-Tryck, Lund 2018 NORDIC SWAN ECOLABEL 3041 0903

Lund University
Faculty of Engineering
Department of Physics
Division of Combustion Physics
ISBN 978-91-7753-467-9 (print)
ISBN 978-91-7753-468-6 (pdf)
ISSN 1102-8718
ISRN: LUTFD2/TFCP-207-SE